ELECTRIC FIELD EFFECTS ON DENSIFICATION OF TiB_2 AND $BaTiO_3$: A TIME-RESOLVED IN-SITU ENERGY DISPERSIVE X-RAY DIFFRACTION STUDY

By

TEVFIK ERTUGRUL OZDEMIR

A dissertation submitted to the

Graduate School-New Brunswick

Rutgers, The State University of New Jersey

In partial fulfillment of the requirements

For the degree of

Doctor of Philosophy

Graduate Program in Materials Science and Engineering

Written under the direction of

Thomas Tsakalakos

And approved by

_____

_____

_____

_____

New Brunswick, New Jersey

January, 2016

ABSTRACT OF THE DISSERTATION

Electric Field Effects on Densification of TiB_2 and $BaTiO_3$: A Time-Resolved in-situ Energy Dispersive X-Ray Diffraction Study

by TEVFIK ERTUGRUL OZDEMIR

Dissertation Director:

Thomas Tsakalakos

Flash sintering is a unique consolidation method of applying an electric field directly on a specimen while heating it. This method results in outstanding densification results at temperature values typically 30-70% less than the conventional sintering temperature and at ultra-short time scales such as 1-2 orders of magnitude smaller than conventional sintering times. This technique has been used on many oxide and non-oxide ceramics and yielded high densification results.

This thesis seeks to establish an improved understanding on mass flux phenomena at unit cell scale under an applied dc electric field utilizing energy dispersive x-ray diffraction (EDXRD). Titanium diboride (TiB_2) and barium titanate ($BaTiO_3$) were chosen as the materials of interest to investigate the electric field induced densification and phase transformation. Uniaxially cold pressed TiB_2 and $BaTiO_3$ particulate matters of $\leq$ 128 nm and $\leq$ 100 nm median particle size, respectively, were used. A custom made experimental setup was utilized for in-situ flash sintering experiments. An electric field of chosen

amplitude, depending on the electrical properties of the material on which each experiment was carried out, was directly applied on the bulk sample while it was being subjected to thermal field. TiB_2 samples showed no densification but oxidation and a phase transformation between already existing oxides in the raw commercial powder even in an inert atmosphere due to its high tendency to oxidation and poor sinterability. All new oxide peaks occurred upon current leakage were found to be of titanium borate ($TiBO_3$). $BaTiO_3$ was found to be more prone to densification compared to TiB_2. 92% - 94% ρ_{th} was obtained in $BaTiO_3$ pellets based on two different commercial powders as the temperature and sintering time ranging from ~400 °C to ~950 °C and from 24 seconds to ~1.5 minutes, respectively. This material, in addition to consolidation, showed a phase transformation from cubic to tetragonal structure under electric fields smaller than its coercive field.

Ultra-high energy polychromatic radiation with photons of as much energy as 200 keV was employed as energy dispersive x-ray diffraction method (EDXRD) to collect data from the body center of each sample with a time interval as short as maximum 4 seconds while the sample was being subjected to thermal and electric fields. Changes in crystal parameters, and hence unit cell volume, were continuously tracked. Therefore, all mass transport phenomena was monitored and recorded with an error of ≤4 seconds. Phase transformations occurred under applied fields were determined by examining EDXRD data. Scanning electron microscope (SEM) and powder x-ray diffraction were also utilized for the characterization of $BaTiO_3$ for continuity and completeness of the analysis on its consolidation.

Acknowledgements

I would like to first thank my advisor Prof. Thomas Tsakalakos and Dr. Enver K. Akdogan. This dissertation study would not have been possible without their keen insight, guidance, and feedbacks. I have greatly benefitted from their knowledge and experience. I would also like to extend my thanks to my dissertation committee: Prof. Lisa Klein, Prof. Bernard Kear, and Dr. Zhong Zhong. Their suggestions, support, and friendly approach is greatly acknowledged.

I give thanks to past and current Nanomaterials Laboratory (NML) group members Ilyas, Hulya, and William for their all support and input. I also thank Berra, Muharrem, Ibrahim, Damien, Fatih, Metin, Azmi, Zeynep, Sukanya, Ahmed, Elaheh, and everyone else in Rutgers MSE whom I have not mentioned in name.

I would like to acknowledge the Turkish Ministry of Education for the financial support they provided me with. Also, I wish to express my thanks for the funding provided by the Office of Naval Research (ONR) under contract no. N00014-10-1-042 and N000141512492. Significant contributions were made by Dr. A. Makinen and Dr. L. Kabacoff of the ONR and Dr. J. Okasinski of ANL with respect to valuable technical feedbacks.

Most of all, I am forever indebted to my family for their unending love and support which sustained me during the difficult times. Their moral support has always made me carry on.

Table of Contents

List of Tables

List of Figures

1. Introduction

Sintering, as a manufacturing process, refers to an increase in the density of a material up to a value close to its theoretical density. Different methods have been used for different materials to date. Some of the major parameters which influence the sintering process, and hence the density of the material of interest, have been listed as temperature, pressure, electric field, time, particle size, and particle-particle contact in open literature. In conventional sintering methods, temperature value to acquire enough density in a material is 2/3 of its melting temperature. This temperature decreases under the influence of some other external forces such as pressure and electric field. A recent method called flash sintering (FS), a.k.a. burst mode densification (BMD), yields outstanding results that BMD temperature and time is 30-70% and 1-2 orders of magnitude less than regular sintering conditions, respectively.

Titanium diboride (TiB_2) is a promising material for many applications in military and technological realms because it exhibits good mechanical and thermal properties. Furthermore, TiB_2 is being used extensively as an electrode material in electrolytic processing of aluminum because of its chemical inertness against aluminum.[15] This material is also used as an additive to obtain fine grain size aluminum castings because of its surface thermodynamic compatibility with aluminum, i.e. wettability and low solubility in molten aluminum.[16] Besides, It is a good metallic and thermal conductor.[17] However, this material in question has a low self-diffusion coefficient that sintering this material to high densities is difficult. Therefore, temperature should be increased up to 2000 °C to obtain enough densification, but exaggerated grain growth is observed at this level of

temperature values. Another disadvantage of this material is its high tendency to oxidation, especially at high temperatures. Therefore, TiB_2 powders contain more oxygen compared to other commercial powders. Given this fact, sintering additives are mostly used to sinter this material to high densities ($\geq$95% ρ_{th}) and to prevent it from oxidation.

Barium titanate ($BaTiO_3$) is a dielectric in cubic structure and a ferroelectric in tetragonal structure. Its tetragonal structure exhibits excellent piezoelectric and thermoelectric properties.[18] It has been one of the major materials in electronics industry, especially in the manufacturing of capacitors, ever since it was discovered due to its high dielectric properties. $BaTiO_3$ is usually kept at $\geq$1300 °C for 2 h to obtain high densification $\geq$95% ρ_{th}.[19] Sintering this material at 950 °C for 20 h using conventional method only results in 80% density.[20] Researches on grain growth of $BaTiO_3$ as well as the size effect on its structure have been of interest. Suppressing the grain growth which event mostly occurs during sintering is also of importance.

This thesis seeks to investigate the implementation of flash sintering method on TiB_2 and $BaTiO_3$. Results of in-situ experiments carried out to examine the effects of thermal and dc electric fields simultaneously imposed on these materials at unit cell scale using energy dispersive x-ray diffraction (EDXRD) with a kinetic of as frequent as maximum 4 seconds will be discussed. Analysis on the crystal parameters, and hence unit cell volume, calculated using traditional methods will be presented. Quantitative phase analysis done, using integrated area under the strongest peak of each phase on EDXRD spectra, to determine the phase composition present in TiB_2 will be evaluated. Adiabatic

calculations on power vs time graphs obtained during the burst event of both materials to find out the required temperature values to acquire the same magnitude of work in the absence of electric field will be exhibited. Results of more non-destructive characterization, such as Archimedes density, microstructural observation, and powder x-ray diffraction, performed on dense $BaTiO_3$ samples will be shown. Because of the resolution issues with EDXRD as a result of $BaTiO_3$ having a high atomic number, powder x-ray diffraction analysis will be of significance in structural phase transformation of this material upon an electric field. Also, the result and challenges encountered during piezoelectric coefficient measurements will be highlighted.

2. Background

This section presents a brief scientific background on TiB_2, $BaTiO_3$, and flash sintering (FS) leading to present dissertation. Previous works on BMD as well as sintering behaviors and physical and chemical properties of the materials in question are examined here to form the core of this study.

2.1. Flash Sintering Method

Flash sintering method, a.k.a. burst mode densification, has recently been employed by many researchers to study densification of different materials under the application of an electric field on the material of interest.[7–20] In this method, an electric field is directly imposed on the specimen as it is being heated. The material which is being worked on becomes conductive at a certain temperature depending on its electrical and thermal properties, and current starts flowing though the specimen. Burst of charges, a.k.a. burst event, occurs after a while the current flow is first observed. Burst event can simply be defined as a sudden rise in the current flow from as low as 0.1 A to the set current cut-off. Power absorbed by the specimen is coupled with consolidation of the material, i.e. the more power the sample absorbs the more density it exhibits. Enormous increase in the density of the sample subjected to an electric field in a very short time span was attributed to local Joule heating at grain boundaries at first.[2] However, it was later proposed that applied electric field activates additional mechanisms, such as surface oxide removal, electromigration, and electroplasticity, accompanying ultra-fast mass flux in the material.[12, 33] The biggest advantage of this method, in addition to 30-70% lower sintering temperatures, is humongous decrease in sintering time down to ≤30 seconds. Figure 2.1

depicts a representative plot of the efficiency of flash sintering method.[2] These results are of flash sintered yttria-stabilized zirconia (3YSZ).[2] As seen in the figure, application of higher field results in lower sintering temperature till which no significant shrinkage is observed in the material. Required sintering temperature is higher, as expected, in the absence of electric field compared to those under the influence of a given electric field. In a nutshell, this material was sintered in few seconds using flash sintering method although conventional sintering method requires hours to sinter it.

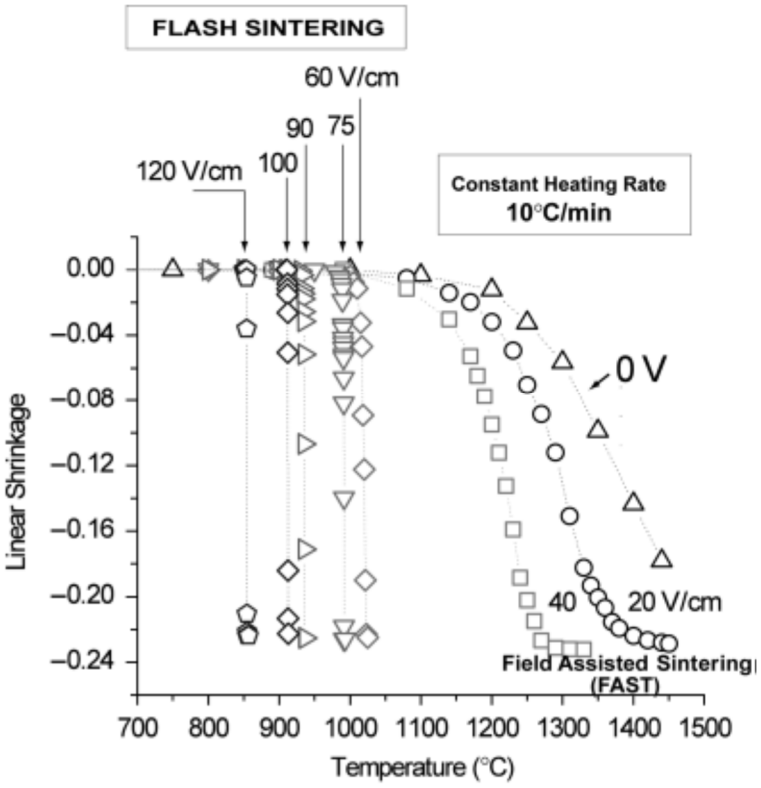

Figure 2.1. Shrinkage in yttria-stabilized zirconia (3YSZ) under the application of different magnitude of dc electric fields[2]

2.2. Titanium Diboride (TiB_2)

Titanium diboride is a transition metal synthesized by using several methods such as metal-thermal reduction,[34] direct reaction of Ti and B,[35] arc-plasma method,[36, 37] and gas-phase combustion (a.k.a. flame) method.[38] TiB_2 is an attractive material for use in military applications since it has prominent mechanical and physical properties such as an elastic modulus of E=565 GPa at 298 K, a temperature coefficient (dE/dt) of -0.032 GPa/K, and an ultrahigh Vicker's hardness of 25-34 GPa at 298 K.[39, 40] It is also considered as a promising interconnection material for integrated circuits.[41] Additionally, its high melting temperature ($T_m \geq 3000$ °C[42]) makes it a material of interest for high temperature applications.[43–46] It also has a good corrosion and wear resistance.[4, 5, 44, 47, 48] This ceramic is also used as an electrode in the electrolysis process of aluminum due to its chemical inertness against aluminum.[15] Furthermore, TiB_2 is being used as an additive to obtain fine grain size aluminum casting because of its surface thermodynamic compatibility with aluminum, i.e. wettability and low solubility in molten aluminum.[16] Besides, it is a good thermal conductor (96 W/m·K at 298 K).[17] The resistivity of TiB_2 decreases with increasing thickness, so a thin film boride shows much higher resistivity compared to a bulk specimen.[49] Also, grain boundaries, defects, and trapped impurities are blamed for the increase in the resistivity of a material. While the resistivity of this material is ~15 x 10^{-6} Ωcm at 298 K for a polycrystalline bulk specimen[50], it is ~6.5 x 10^{-6} Ωcm for a single crystal sample as being independent of the orientation of the crystal[49]. Furthermore, because it has a low electrical resistivity, it can be machined using electrical discharge machining (EDM).[51] Despite the outstanding properties and high potential of TiB_2, it is difficult to sinter this material to high densities due to its low self-diffusion coefficient as

a result of covalent bonds. It is also very prone to oxidation that the presence of an oxygen rich layer on its surface inhibits densification. Moreover, it has a poor flexural strength and fracture toughness.[52] Although it has a great potential to be used in many applications such as cutting tools, wear-resistant bodies, armor materials, and so on, it is commercially limited due to these disadvantages.

2.2.1. Phase Diagram and Crystal Parameters

TiB_2 is a stable intermetallic phase as seen in the phase diagram in Figure 2.2.[3] It is a stable material which has high melting temperature (>3000 °C) and narrow homogeneity, whereas orthorhombic TiB and Ti3B4 exhibit less melting temperature.[3] TiB and Ti3B4 decompose peritectically at ~2200 °C as seen in the figure. The stoichiometry of B ranges from 28.5 wt% to 30 wt% in the formation of TiB_2.[3, 5]

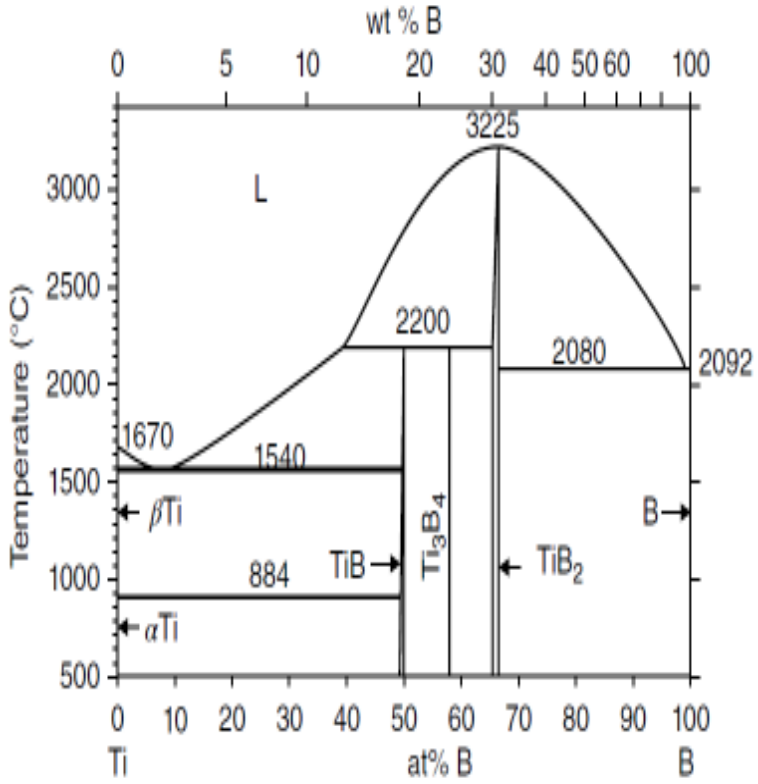

Figure 2. 2. Equilibrium phase diagram of binary Ti-B system[3] showing three possible Ti-B intermetallic composition, TiB, Ti_3B_4, and TiB_2

Single crystal TiB_2 has a hexagonal structure with a space group of P6/mmm. Its crystal parameters typically are a=3.03034 and c=3.22953, and hence c/a=1.066 ± 0.001 at 298 K.[53, 54] (000) is occupied by titanium and (1/3, 2/3, 1/2) and (2/3, 1/3, 1/2) by boron (Fig.2.3a).[4, 5] B atoms are interstitially located between Ti atoms of hexagonal layers, thereby forming strong covalent bonds to which the high mechanical properties of TiB_2 are attributed (Figure 2.3b).[6]

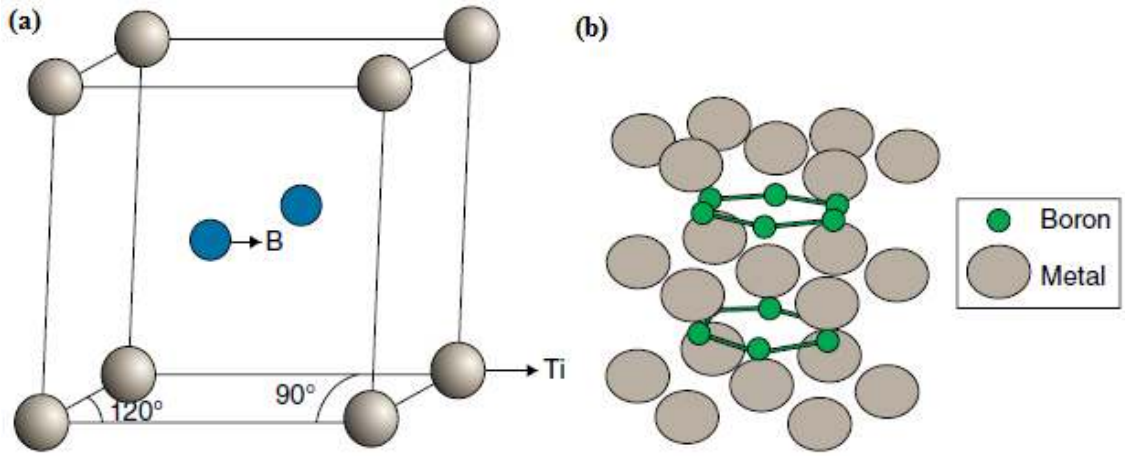

Figure 2. 3. a) Schematic illustration of AlB2 type hexagonal unitcell structure of a single crystal TiB_2, space group P6/mmm, a=b=3.03034 Å, c=3.22953 Å, α=β=90°, and γ=120°,[4, 5] **b)** representation of B atoms interstitially located between metal layers

Temperature dependence of the lattice parameters of TiB_2 is exhibited in Figure 2.4 that the ratio, c/a, increases, from 1.066 ± 0.001 to 1.070 ± 0.001, with an increase in the temperature, from 25 °C to 1500 °C.[4] Each lattice parameter, a and c, of hexagonal TiB_2 can quantitatively be defined as follows;[4]

$$a = 3.0236 + 1.73 * 10^{-5} * (T) + 3.76 * 10^{-9} * T^2 \quad (2.1)$$

$$c = 3.2204 + 2.73 * 10^{-5} * (T) + 3.95 * 10^{-9} * T^2 \quad (2.2)$$

where a and c are crystal parameters in Angstrom (Å), and temperature is 293 K ≤ T ≤ 2000 K.

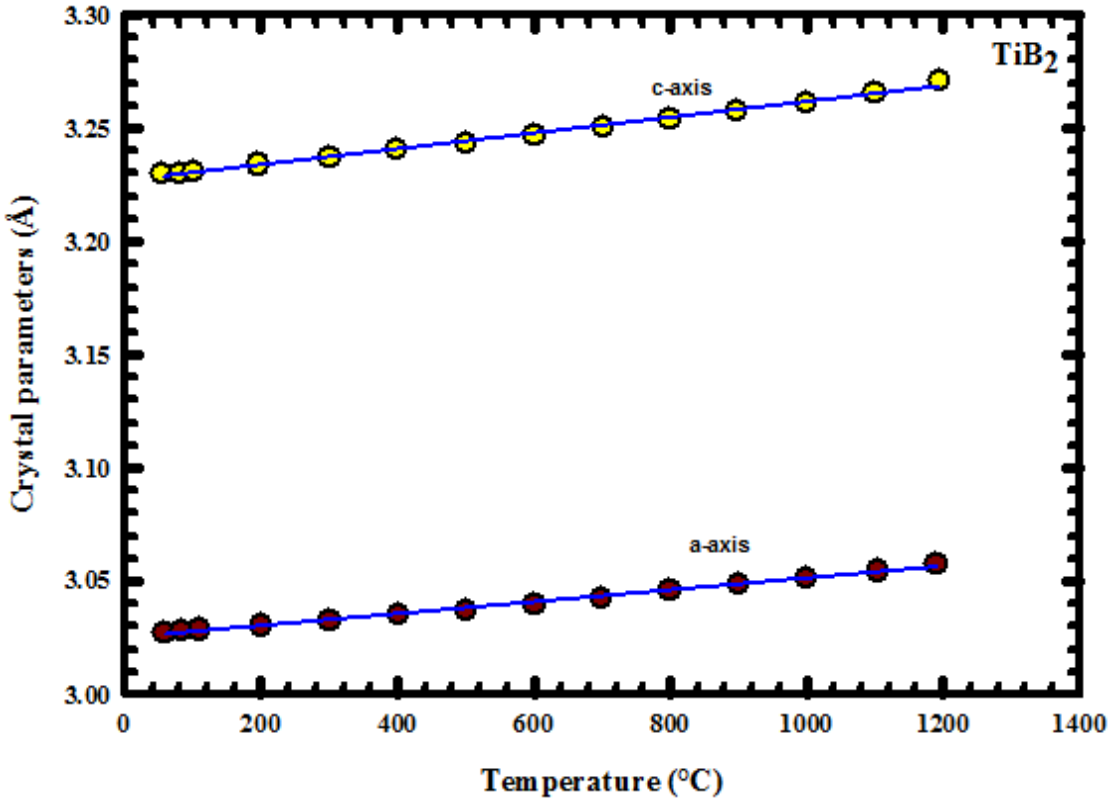

Figure 2. 4. Variation of lattice parameters, a and c, of a single crystal TiB_2 as a function of temperature[4]

The anisotropy due to its hexagonal crystal structure is a disadvantage of this material that it might instigate a thermal stress during cooling which might in turn yield to spontaneous microcracking in the system if the grain size distribution reaches the critical value (≥15 μm).[55]

2.2.2. Mechanical Properties

TiB_2 is one of the hardest ceramic materials. Its high mechanical properties are attributed to the strong covalent bonds between Ti and B atoms. Mechanical properties of TiB_2 vary depending on the synthesizing and processing methods. Grain size, porosity, and

hence the density of the sample have a clear effect on its mechanical properties. Temperature is also another external force affects the properties of this material. Almost all diborides, such as HfB_2 and ZrB_2, present a decreasing elastic modulus with an increase in temperature, especially over 900 °C. TiB_2 exhibits higher modulus of elasticity compared to other diborides at any temperature value. Reported elastic modulus of a dense TiB_2 sample is E=565 GPa at 298 K.[39, 40, 56]

TiB_2 is among the hardest ceramic materials with a Vickers hardness value ranging from 25 GPa to 34 GPa. Since temperature increase softens a material, and deformation left on the material increases after indentation at elevated temperatures, hardness value of that material, unlike elastic modulus, decreases with increasing temperature. Because TiB_2 is a promising refractory material for high temperature applications, hardness values obtained at service temperatures are of significance. Density of a material is another influential factor at play that the denser the material, the harder it is. Figure 2.5 depicts the changes in the hardness value of TiB_2 upon heating.[4, 7–9] Figure 2.5a additionally shows how porosity is effective on the hardness of TiB_2 that a sample of 20% porosity is softer than that of 6% porosity.[7] The difference between the hardness values of these two samples of different densities decreases from ~100 Kg/mm^2 to ~20 Kg/mm^2 as the temperature increases from ~1000 °C to ~1400 °C. The values read on the plot might be lower than the actual hardness value of TiB_2 (Fig. 2.5a). This is so mostly due to the used indentation technique by A. G. Atkins and D. Tabor given the difficulty of the measurements at those temperature values in 1960s. However, this study still gives an idea about the effects of temperature and porosity on the hardness of a material.[7] The values shown on Figure 2.5b

were collected from recent studies that they more or less match with the common hardness value of TiB_2 found in the open literature.[1, 4, 8, 9] This plot also reveals that the hardness of monolithic TiB_2, as well as of its any composite such as TiB_2-$TiSi_2$ and TiB_2-$MoSi_2$, decreases with increasing temperature as expected.

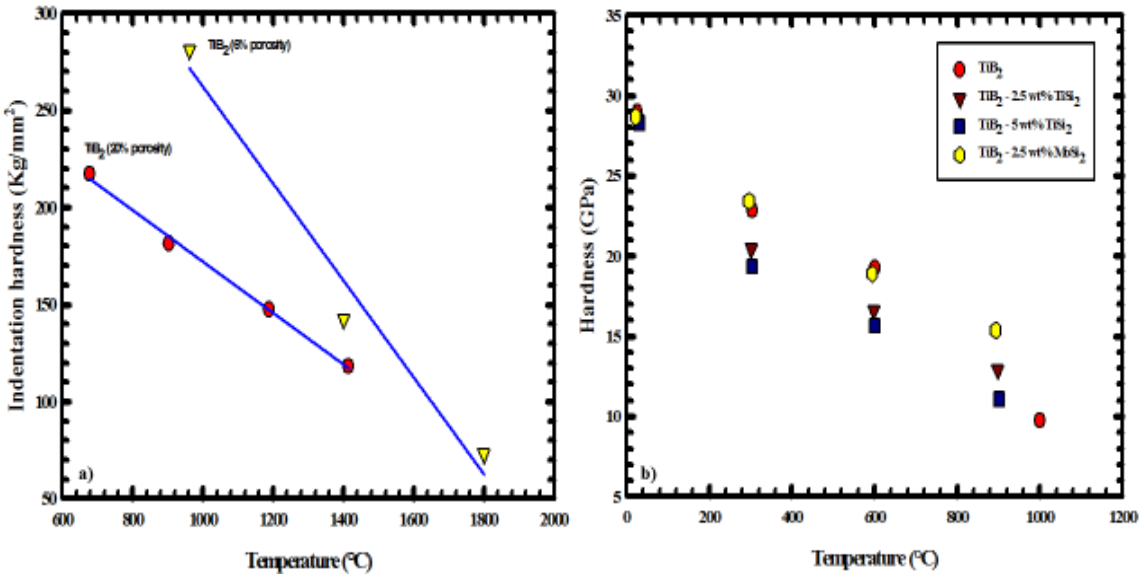

Figure 2. 5. Hardness values of **a)** TiB_2 of different porosity and **b)** TiB_2 and TiB_2-$TiSi_2$ and TiB_2-$MoSi_2$ of different compositions[1, 4, 8, 9] as a function of temperature

A detailed evaluation of temperature dependence of the hardness of TiB_2 is presented in Table 2.1. Addition of 5 wt% $TiSi_2$ decreases the sintering temperature from 1800 °C to 1650 °C while increasing the hardness of TiB_2 by 5.92% at RT.[1] Hardness of monolithic TiB_2 hot pressed at 1800 °C for 1 h is 25.3 ± 1.8, 13.9 ± 1.4, 10.8 ± 0.7, 8.2 ± 0.7 at RT, 300 °C, 600 °C, and 900 °C, respectively.[1] Addition of 2.5 wt% $TiSi_2$ increases the hardness of monolithic TiB_2 from 7.2 to 8.9 GPa as a result of the enhancement in densification.[1]

Table 2. 1. Relative density, average grain size, and Vickers hardness values of TiB_2-$TiSi_2$ composites hot pressed at 1650 °C for 1 h and monolithic TiB_2 ([a] and [b] hot pressed at 1800 °C and 1650 °C for 1 h, respectively) at different temperatures[1]

Composition (wt%)	**Relative Density (% ρ_{th})**	**Average Grain Size (μm)**	**Vickers Hardness (GPa)**			
			RT	300 °C	600 °C	900 °C
Monolithic TiB_2[a]	97.8	1.5 ± 0.2	25.3 ± 1.8	13.9 ± 1.4	10.8 ± 0.7	8.2 ± 0.7
Monolithic TiB_2[b]	94.4	3.6 ± 0.7	21.2 ± 1.1	13.8 ± 0.4	9.8 ± 0.5	7.2 ± 0.5
TiB_2-2.5% $TiSi_2$	98.8	2.3 ± 0.3	27.0 ± 1.7	15.1 ± 0.3	11.5 ± 0.6	8.9 ± 0.3
TiB_2-5.0% $TiSi_2$	99.6	3.0 ± 0.6	26.8 ± 1.0	14.1 ± 0.8	10.6 ± 0.6	7.8 ± 0.5
TiB_2-10% $TiSi_2$	99.6	3.5 ± 0.5	23.7 ± 2.7	13.1 ± 0.9	9.8 ± 0.6	8.0 ± 0.4

Another important mechanical property is fracture strength, a.k.a. flexural strength which is measured using 3 point or 4 point bending test. It is sensitive to average grain size, density, secondary phase(s) at grain boundaries, additive content if any used.[1, 5, 6, 57] Small amount (1-2 wt%) of metallic additives, such as Fe, Ni, and Cr, result in high density (≥ 99%), high hardness value (23-31 GPa), moderate fracture toughness (~4-5 MPa . $m^{1/2}$), and fracture strength (≥500 GPa) in TiB_2; however, these properties cannot be retained at elevated temperatures. Table 2.2 shows the flexural strength of TiB_2 at different

temperature values.[4, 9, 37] As seen in the table that hot pressing process (HP) results in an appreciable increase in the fracture strength of TiB_2 at elevated temperatures (1000 °C) compared to pressureless sintering (PS) though the density obtained at 2100 °C using pressureless sintering is higher than that at 1800 °C under pressure.

Table 2. 2. Flexural strength and density of TiB_2 sintered using different methods

Material	**Processing (Method, °C, min, MPa)**				**Density (% ρ_{th})**	**Bending**	**Flexural Strength (MPa)**		
							RT	1000 °C	1200 °C
TiB_2	PS	1900	60	-	>95	3P, Argon, 3.8 x 6.9 x 38 mm^3	310	370	405
TiB_2	PS	2100	60	-	99	-	290	390	400
TiB_2	-				99.5	-	400	459	471
TiB_2	HP	1800	60	30	98	4P, Air, 3 x 4 x 40 mm^3	387	546	-

2.2.3. Thermal and Electrical Properties

Thermal expansion coefficient, a.k.a. coefficient of thermal expansion (CTE, α in symbol), is one of the most significant thermal properties of a material that change in the length of a material (Δl) is proportional to temperature difference (ΔT) and its initial length (l_0). Hence, CTE is a concise expression of full extent of the ultimate dilation of a material under applied heat. Expansion of TiB_2 is anisotropic due to its hexagonal unitcell structure,

thereby having a thermal expansion coefficient of α_c= 9.2 x 10^{-6} K^{-1} in the direction of c-axis and that of α_a= 6.4 x 10^{-6} K^{-1} at right angles to the c-axis, the basal planes, so that the mean linear CTE is α_m= 7.33 x 10^{-6} K^{-1}.[4] CTE is also of importance in the binder choice that a large CTE mismatch between the host material and binder might result in thermal, and hence residual, stresses during cooling which might in turn yield microcracking even in the absence of external loads. Addition of Ti_5Si_3 instigate microcracking in TiB_2 as a result of large difference between their thermal CTEs.[8]

Another significant thermal property is specific heat. This property is defined as the required heat per unit mass to raise its temperature by 1 K.[4] Specific heat of this material is expressed by the following equation found in open literature;[4]

$$C_p = 976 + 0.21 * (T - 273) - 426 * exp[-c_3(T - 273)] \text{ (J/kg K)} \quad (2.3)$$

As for thermal diffusivity and thermal conductivity of this material, following expression can be used;[4]

$$D = D_0 + \frac{D_1 exp[-D_2(T/K - 273)]}{D_3 + (T/K - 273)} \quad (2.4)$$

$$\kappa = \kappa_0 + \frac{\kappa_1 exp[-\kappa_2(T/K - 273)]}{\kappa_3 + (T/K - 273)} \quad (2.5)$$

2.2.4. Sintering of TiB_2

Sintering of TiB_2 is a difficult and expensive process. The required temperature to conventionally sinter this material is ≥2000 °C. However, it requires lower temperatures under applied pressure. Therefore, hot pressing method is widely employed to fabricate dense TiB_2. Although conventional method is a cheaper way to obtain dense TiB_2 compared to hot pressing, higher temperatures lead to exaggerated grain growth as a result of which the material shows lower mechanical properties. Therefore, sintering aids, such as C, Ti, Ni, Fe, Cr, SiC, $TiSi_2$ and NiB, are used to eliminate the grain growth and enhance the densification. Though the mass or volumetric fraction of the additive changes depending on its effects on the sintering process of TiB_2, it mostly ranges from 1% to 10%. While it is enough to add a metallic additive less than 2 wt% to obtain high densification, more nonmetallic additive, 5-10 wt%, is required to achieve the same.[5] Addition of a sintering aid helps not only to increase the consolidation but also to decrease the sintering temperature and time. Despite the fact that the use of metallic additives such as Ni, Fe, Co, and Cr by liquid phase sintering (LPS hereafter) yields very dense specimens as high as 99% of theoretical density (TD hereafter),[58–61] some unique properties of these samples, such as fracture toughness and hardness, decrease as a result of the extremely brittle secondary borides which form by chemical reactions between TiB_2 and metallic additives during densification process.[62] Therefore, nonmetallic additives are preferred over metallic ones to achieve high densities as well as retain the thermal properties of TiB_2. Raju et al. used ≥5 wt% $TiSi_2$ sintering aid and achieved the highest density of >99% ρ_{th} by hot pressing TiB_2 at 1650 °C for 1 hour while sintered monolithic TiB_2 to only 94.6% under the same conditions.[8] They revealed in the same study that the mechanical properties of

TiB_2 is adversely affected by an increase in the amount of the used $TiSi_2$ (10 wt%) as a result of the excessive secondary phase though achieved density is still >99% ρ_{th}.[8] Therefore, 5 wt% $TiSi_2$ was found to be the optimum amount to obtain the highest density and mechanical properties.[8] Given the good properties of TiB_2 such as high stiffness and hardness and high electrical and thermal conductivity, it has been used as a reinforcement material for copper matrix composites.[63, 64] Hence, Xu et al. used copper to obtain and densify a TiB_2-Cu matrix composite.[65] The positive effects of Cu on the densification process of TiB_2 were exhibited.[65] Most of the mechanical properties of the matrix were found to be superior to those of synthesized pure TiB_2 though it was more available to crack formation due to any thermal stress.[65] Aluminum nitride is another additive used in the sintering process of TiB_2.[52] TiO_2, which is mostly found on the surface of TiB_2, was eliminated by the addition of AlN of less than 5 wt%, so that higher densification and mechanical properties were obtained compared to pure TiB_2.[52] The reaction between TiO_2 and AlN yielded TiN and Al_2O_3 formation.[52] However, the increase in the amount of AlN (≥10 wt%) resulted in inferior consolidation and properties due to the excessive unreacted secondary phase,[52] as the same holds true for $TiSi_2$.[8] Although the binderless monolithic TiB_2 densifies at 1800 °C in 1 hour by hot pressing, the addition of $MoSi_2$ (10-20 wt%) decreases it to 1700 °C under the same pressing conditions.[47] The density of the hot pressed TiB_2 – 10 wt% $MoSi_2$ composite was found to be ~97-99% of a high Vickers hardness (~26.5 GPa) and a modest indentation toughness (~4.3 MPa . $m^{1/2}$).[47] Muraoka et al. achieved the maximum density of 98.6% in TiB_2 with the addition of 20% ZrO_2 (2 mol% Y_2O_3) under hot isostatic pressure.[66] However, TiB_2 - 30% ZrO_2 (2 mol% Y_2O_3) matrix composite showed the highest mechanical properties, fracture toughness (11.2 MPa . $m^{1/2}$)

and bending strength (680 MPa) under the same sintering conditions.[66] Silicon carbide (SiC) and silicon nitride (Si_3N_4) are the most effective sintering aids in the consolidation process of TiB_2 since they eliminate the oxides on the surface of TiB_2 as well as form an amorphous silicon oxide (SiO_2).[67, 68] The density of pure TiB_2 hot pressed at 1800 °C for 1 hour was found to be 90% while the addition of Si_3N_4 sintering aid of 2.5 wt% resulted in >99% ρ_{th} with a remarkable increase in the mechanical properties other than fracture toughness.[68] More than 2.5 wt% Si_3N_4 in the system caused a decrease in the density (and hence the mechanical properties) as a result of excessive formation of amorphous silica (SiO_2).[68] As metallic additives, 0.5 wt% chromium (Cr) and 0.5 wt% iron (Fe) were used to enhance the densification of TiB_2 by Kang et al.[69] The specimens were sintered to 97.6% and 98.8% at 1800 °C and 1900 °C in 2 hours without pressure, respectively.[69] Although the sample sintered at lower temperature showed lower density (97.6%), its strength (506 MPa) and fracture toughness (6.16 MPa . $m^{1/2}$) were superior to those of the one sintered at 1900 °C.[69] The relative densities of the specimens containing either 1 wt% Cr or 1 wt% Fe were found to be 92.6% and 93.2%, respectively, so the simultaneous addition of both sintering aids at the same amount of 0.5 wt% is more effective than the addition of each material individually.[69]

Pettersson et al. sintered $(Ti)_{0.05}$ $(TiB_2)_{0.95}$ and TiB_2 using spark plasma sintering (SPS) and hot isostatic pressing (HIP) (T=1450 °C, P=50 MPa, and t=5 min), respectively and investigated and compared their mechanical and ballistic properties.[70] All measured properties of SPS - $(Ti)_{0.05}$ $(TiB_2)_{0.95}$ were found to be superior to those of HIP - (TiB_2), and their values are; ρ_{th}=4.5 g/cm^3, H=26 GPa, K_{IC}=4.5 MPa . $m^{1/2}$, and σ_F=640 MPa for

SPS - $(Ti)_{0.05}$ $(TiB_2)_{0.95}$ and ρ_{th}=4.4 g/cm^3, H=18.5 GPa, K_{IC}=4 MPa . m$^{1/2}$, and σ_F=475 MPa for HIP - (TiB_2) as ρ_{th}, H, K_{IC}, and σ_F stand for density, hardness, fracture toughness, and bending strength, respectively.[70] Besides, the ballistic results revealed that the penetration resistance of SPS - $(Ti)_{0.05}$ $(TiB_2)_{0.95}$ is 40% higher than that of HIP - (TiB_2).[70]

2.3. Barium Titanate ($BaTiO_3$)

Barium titanate exhibits dielectric and ferroelectric properties in its cubic and tetragonal structures, respectively. Therefore, a general look on dielectrics and ferroelectrics is presented in this section followed by a specific review on $BaTiO_3$.

2.3.1. Dielectrics

A dielectric is simply an insulating material. A dielectric material under the influence of an electric field exhibits the phenomena called polarization. The charges within the material subjected to an applied voltage show a slight shift in their positions, so that an internal electric field, which reduces the total electric field in the system, occurs in the material. Charges do not flow through the sample as in a conductive material. Faraday called these materials dielectrics for the first time,[71] and they have been largely used in the capacitors. A dielectric material between two conductive plates increases the capacitance of them which is what absolutely is aimed in the capacitors.

The capacitance of a capacitor is mostly dependent on the relative permittivity of the dielectric material in the middle, i. e. the conductive plates between which the dielectric material is placed are electrically charged as one of them becomes negative and the other

one becomes positive, and this electric field generates polarization in the dielectric material. Relative permittivity, a.k.a. dielectric constant, determines the storability of charges within a material. The term "relative" is used to define the permittivity of the material with respect to vacuum. Therefore, the equation used to calculate the dielectric constant of a material is $\varepsilon_r = \varepsilon/\varepsilon_0$ (where E_r is the relative permittivity, E is the absolute permittivity of the material, and E_0 is the permittivity of the vacuum ($8.854 * 10^{-12}$ F/m)).

Another significant term when talking about a dielectric material is dielectric loss, a.k.a. loss tangent. Permittivity of a dielectric material is typically described with a mathematical expression consists of both a real and an imaginary part as $\varepsilon = \varepsilon' + i\varepsilon''$. The imaginary part of the expression in question represents the loss of the alternating electric field applied on the material. In other words, it gives an insight about the energy turns into heat due to the polarization instigated by the electric field. The real part in the expression stands for the relative permittivity of the material which is its permittivity compared to the permittivity of vacuum as explained above. The imaginary part of the above equation is zero for the dielectric materials which show no loss, such as free-space.

2.3.2. Ferroelectrics

All materials exhibit atomic polarization, which is defined as the displacement of the electrons, under an applied voltage. In a dielectric material, applied voltage results in a dipole moment that the material becomes polarized. Applied voltage, as well as lattice polarization, result in local field which aims to stabilize the polarization in the material that an atom or an ion (for ionic materials) is largely affected by this local field. This event

might cause the phenomena called spontaneous polarization. This phenomena is defined as existence of a dipole or a lattice polarization in the material even after the removal of the applied voltage. Ferroelectrics, a.k.a. ferroelectric materials, are the main materials exhibit this phenomena.[72] Ferroelectric materials exhibit high dielectric properties, i.e. high relative permittivity, due to the spontaneous polarization and asymmetry,[73, 74] i.e. dependency of the orientation of the polarization on the direction of the applied electric field. Therefore, two properties required to define a material as a ferroelectric are spontaneous polarization and reorientation of the polarization.[10]

Each ferroelectric material has a critical temperature value, which is known as the Curie temperature, above which it turns into a dielectric material.[73] The main reason of the change in the electrical properties of a material at its Curie temperature is simply the change in its spontaneous polarization at this point. Moreover, the material subjected to heat exhibits a transition from a reorientable spontaneous polarization state to an electrically neutral state over its Curie temperature. Almost all ferroelectrics exhibit this phenomena though some of the materials decompose before or at their Curie temperatures.

A ferroelectric develops a domain structure under its Curie temperature that the alignment of the polarization in each domain is the same direction. A domain wall separating two domains having different polarization directions moves with the application of an electric field, so that each domain occurs. The direction of the polarization in each domain can be changed by the application of an electric field in another direction that its reversal yields another phenomena in ferroelectrics known as domain switching.[75]

Hysteresis loop is commonly utilized to evaluate the relationship between the polarization (P) of a material and applied electric field (E). It is commonly used to identify a material, and it is such a fingerprint that it is unlikely for another material to have the same loop. Figure 2.6 depicts typical hysteresis loops of (a) $BaTiO_3$ capacitor, (b) soft PZT, (c) PLZT 8.6/65/35 relaxor, and (d) PSZT anti-ferroelectric material.[10] An anti-ferroelectric material is a nonpolar, non-ferroelectric ceramic which can turn into a ferroelectric material under an electric field of sufficient amplitude.[10] The information can be extracted from the representative hysteresis loops in Figure 2.6 are; (1) the material in (b) has a memory whereas the one in (c) is very unlikely to have a memory, (2) high remanent polarization (P_R) is coupled with high internal polarizability, strain, electromechanical coupling, and electro-optic activity, (3) coercive field (E_C) relates to the grain size for a given material, i.e. the larger the grain size, the lower the E_C is, (4) loop squareness indicates that the grain has better homogeneity and uniformity, (5) off-centered loop from the zero voltage point shows that the system has some internal electrical bias as a result of internal space charge, (6) the sharpness of a loop tip is a proof of high electrical resistivity ($>10^9$ Ωcm), (7) relaxor materials having high induced polarization show high electrostriction strain and high electro-optic coefficients, (8) the slope of the P-E loop at a given point on the loop gives the large signal dielectric constant, (9) the opening of the loop of an SFE relaxor material indicates non-ohmic contact between the electrodes and the material, and (10) an anomalous change in the polarization is mostly a result of an initial dielectric breakdown.[10]

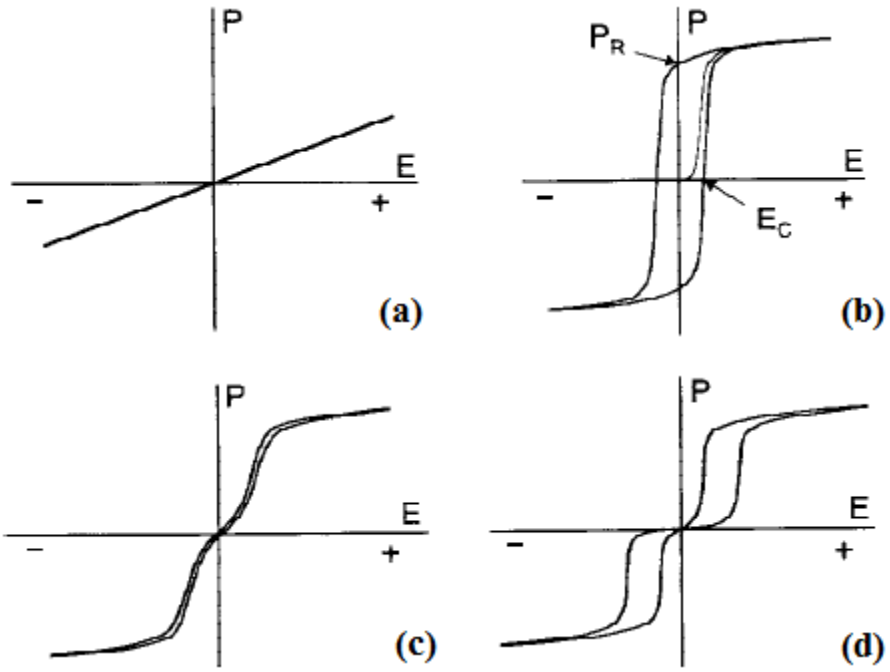

Figure 2. 6. (a) $BaTiO_3$ capacitor, **(b)** soft PZT, **(c)** PLZT 8.6/65/35 relaxor, and **(d)** PSZT anti-ferroelectric material[10]

Barium titanate ($BaTiO_3$), lead titanate (PbTiO3), lead zirconate titanate (PZT), lead lanthanum zirconate titanate (PLZT), and lead magnesium niobate (PMN) are some of the ferroelectric materials[10] among which $BaTiO_3$ has been an inevitable material since it was discovered. Perovskites are economically the most important ferroelectrics. A perovskite is basically described by the formula ABO_3. The mineral perovskite, CaTiO3, was first discovered in 1839 by mineralogist Gustav Rose and named after, in honor of, Lev Aleksevich von Perovski.[76] $BaTiO_3$, as a perovskite structure material, is the other material investigated as a part of this two pronged study.

Ferroelectrics have been used in many applications in especially multibillion dollar electronics industry. Major applications in which these materials are used are data storages, transducers, and capacitors. As a result of the need to miniaturize the circuits, multilayer

ceramic capacitors (MLCCs) of high efficiency were developed, and ferroelectric materials of sub-micron grain size have found a large space to be used in the manufacturing of these types of capacitors. Furthermore, ferroelectrics are utilized in the production of varactors for RF/Microwave circuits,[77] multiferroics,[78] high-κ dielectrics,[79] ferroelectric RAMs (F-RAMs),[80] electro-optic modulators,[81] ferroelectric tunnel junctions,[82] piezoelectric transducers,[83] and pyroelectric detectors[84].

2.3.3. Crystallography of $BaTiO_3$

Barium titanate was discovered by different scientists living in different countries, United States, Japan, and Russia, during World War II. The war caused an acceleration in the research on dielectric materials to increase the efficiency of capacitors. Prior to the discovery of $BaTiO_3$, mica, porcelain, steatite, cordierite, and rutile were used in the capacitors due to their high dielectric properties.[85] Among these material, mica was one of the most commonly used one.[85] The dielectric constant of the materials containing rutile (TiO_2) was in the range of 80-100 at that time,[86] and $BaTiO_3$, with its discovery, started attracting attentions on itself due to its high dielectric constant, 1,000, which was 10 times greater than that of any other dielectric material at that time.[85] It has also been in the center of research interest as a lead-free piezoelectric ceramic.[87]

The discovery of $BaTiO_3$ showed that a simple oxide ceramic could also show ferroelectric properties. Barium titanate has a perovskite structure, which is basically presented by a simple formula as ABO3, as mentioned earlier. Therefore, $BaTiO_3$ led other materials of perovskite structure to attract the attention of researchers working on the

dielectrics. In the first decades following the discovery of this material, studies largely focused on ferroelectricity, ferroelectric switching, phase transformation, and the crystallography of this material.[88–95] Barium titanate has rhombohedral (R3m), orthorhombic (Amm2), tetragonal (P4mm), cubic (Pm3m), and hexagonal crystalline structures at different temperature values. The Curie point, which represents the phase transformation temperature at which its electrical properties also change, of this material is ~120 °C depending on the particle size. $BaTiO_3$ turns into paraelectric cubic structure over this temperature value (120 °C) and shows no structural change till ~1400 °C above which temperature its structure is hexagonal. $BaTiO_3$ is normally tetragonal at RT and exhibits spontaneous polarization which indicates that it is a ferroelectric in this crystallographic structure. This material has orthorhombic and rhombohedral crystal structures below 5 °C and -90 °C, respectively. Because its cubic structure has high dielectric properties and its tetragonal structure shows ferroelectricity, these two structures attract more interests in especially electronics industry. Tetragonal $BaTiO_3$ has excellent piezoelectric and thermoelectric properties in addition to its outstanding ferroelectricity.[18] Corners of a $BaTiO_3$ lattice are occupied by barium atoms whereas titanium atom and oxygen atoms are located in the body center and on the center of the faces of the lattice in question, respectively, as depicted in Figure 2.7.[11] Because the titanium ion in a $BaTiO_3$ lattice is way smaller compared to barium ions, it is unlikely to be stable in its position in the body center of the lattice.[96] The minimum energy areas off the body center are towards each oxygen ion that the titanium ion in the structure is highly prone to polarization.[96, 97] Therefore, an externally applied electric field results in a shifting in the position of Ti^{+4} which leads to polarization in the lattice.[96, 97] The polarization in the cubic structure cancels

with the removal of the electric field although it does not completely vanish in tetragonal structure even under zero-electric field.

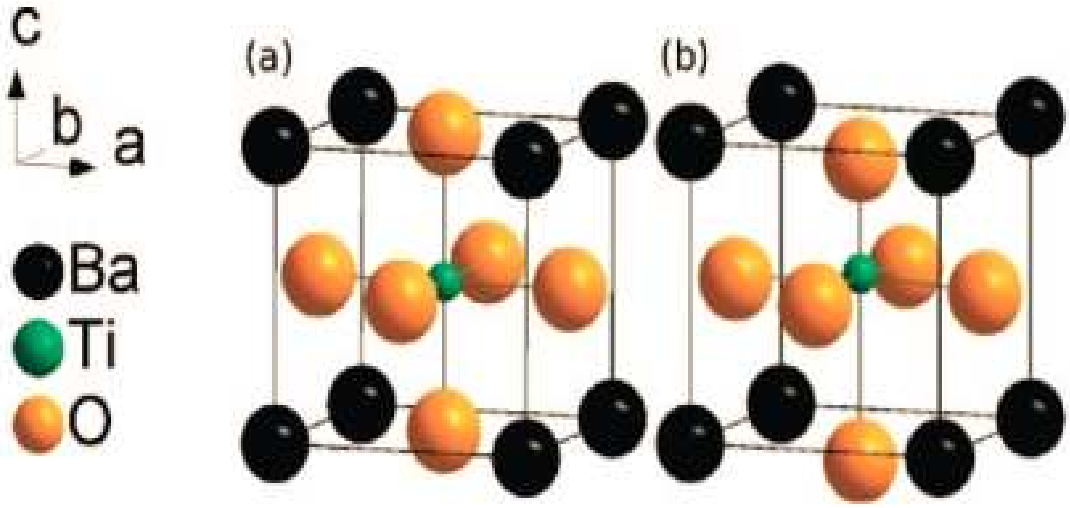

Figure 2. 7. a) Cubic structure $BaTiO_3$ (Pm3m) and **b)** tetragonal structure (P4mmm)[11]

2.3.4. Sintering of Barium Titanate

Different sintering methods including SPS, hot pressing, pressureless, and flash sintering with and without the use of sintering aids were adopted to sinter $BaTiO_3$ since it was discovered.[98–111] The main goal in almost all densification methods used on $BaTiO_3$ is to increase the density of the sample as well as increase its electrical properties, mainly the relative permittivity. Briefly, some of the sintering conditions and results found in the open literature are as follows; ~90.3% ρ_{th} at 1220 °C in 100 minutes,[112] ~95% ρ_{th} at 1100 °C in 6 hours,[113] ~96-99% ρ_{th} at 1200-1300 °C in 2 hours,[114] 90-98% ρ_{th} at 950-1200 °C under 160 MPa pressure using Pyrex glass capsules,[115] ~85% ρ_{th} after reactive sintering at 1300 °C for 2 hours,[116] ~98% ρ_{th} density after microwave sintering at 1100 °C for 30 minutes [106].

Karaki et al. employed two-step sintering method[117] to obtain fine grain $BaTiO_3$.[118] They obtained the highest dielectric properties as well as density under the experimental condition of T_1=1320 °C, T_2=1150 °C, and t_2=15 h.[118] They obtained a relative density of 98.3% after the sintering process.[118] Relative permittivity (ε_r), electromechanical coupling factor (k_p), and piezoelectric coefficient (d_{33}) of the sample were found to be 5000, 0.42, 460 pC/N, respectively.[118] They suggested in their study that high piezo and dielectric properties were not only succeeded by high density, but also by small grain size which was 1.6 μm in the experiment in which they obtained the best results.[118] Wang et al.[20] used the same method, two-step sintering, with Karaki et al.[118] to sinter $BaTiO_3$ as well as Ni-Cu-Zn ferrite. They were able to retain the grain growth suppression while the density of the sample was increasing.[20] The density of each sample they sintered was found to be ≥ 96% ρ_{th}.[20] The smallest grain size they obtained was 35 nm (10 nm prior to the experiment) with a density of 98% ρ_{th} (61% ρ_{th} prior to the experiment) under the experimental conditions of T_1= 950 °C, T_2= 900 °C, and t_2=2 h.[20]

Hsiang et al. studied the sintering behavior and dielectric properties of $BaTiO_3$ ceramics by mixing commercial $BaTiO_3$ powder with ZBS ($ZnO-B_2O_3-SiO_2$).[119] They showed that the use of 5 wt% ZBS glass decreases the sintering temperature of $BaTiO_3$ from 1300 °C to 900 °C and results in a 95% ρ_{th} without the formation of a secondary phase.[119] The dielectric constant and dielectric loss of the sample were found to be 994 and 1.6%, respectively, for the said amount of ZBS.[119] However, adding more (12 wt%) ZBS caused a decrease in the dielectric constant of the sample though its relative density was

over 95% ρ_{th}. Adding less (2 wt%) ZBS, on the other hand, yielded not enough densification due to insufficient liquid phase.[119]

Han et al. compared the results of the experiments in which $BaTiO_3$ was sintered using microwave (MW), spark plasma (SPS), and pressureless sintering (PS) methods.[87] They also showed the colossal permittivity of microwave sintered $BaTiO_3$ and the effects of annealing on its dielectric properties.[87] Sintering conditions they used and the results they acquired are as follows; 94.15% ρ_{th} and 1.29 ± 0.08 μm grain size at 1320 °C within 30 minutes using MWS and 94.15% ρ_{th} after annealing, 93.89% ρ_{th} and 0.21 ± 0.01 μm grain size at 900 °C, and 98.88% ρ_{th} and 0.67 ± 0.11 μm grain size at 1050 °C under 50 MPa pressure, 3 V maximum voltage, and 850 A maximum current within 5 minutes using SPS, and 97.16% ρ_{th} and 10.30 ± 1.39 μm grain size at 1350 °C within 2 hours using PS.[87] The dielectric properties of the sample were found to be 301,484 and 6.901 for relative permittivity and loss tangent, respectively, after MWS process.[87] They annealed the microwave sintered sample at 950-1100 °C for 12-24 hours to let the sample reoxidize to improve its insulating characteristics, and they obtained a colossal permittivity still over 10^4 and a loss tangent ~0.04 under the aforementioned annealing conditions.[87]

Billah et al. evaluated the effects of sintering time on the densification of $BaTiO_3$.[112] They performed a sintering process at a fixed temperature of 1220 °C and identified three densification and one dedensification stages during the experiment.[112] First two densification stages within the first 40 minutes and the following 50 minutes (so the first 90 minutes) showed the maximum densification rates as the first one being the highest.[112]

The third stage of the process from the end of 90 minutes to 110 minutes, the rate of consolidation was found to be very low, and the last stage of the experiment exhibited dedensification of the sample due to the atomic repulsion of the particles.[112] They suggest in their study that if one cannot obtain the desired density at the end of the second stage, increasing temperature and continuing the experiment at a higher temperature should be the next step to increase the density of the specimen.[112]

Hirata et al. compared the effects of hot isostatic pressing and conventional pressureless sintering methods on the sintering temperature, grain growth, and dielectric properties of $BaTiO_3$.[115] They carried out HIP under 160 MPa and found out that the densification temperature could be lowered by 250 °C, using HIP, compared to regular sintering temperature to obtain the same density acquired using pressureless sintering which was above 90% ρ_{th}.[115] Sintering process performed at 950-1200 °C under the said pressure using HIP yielded samples with a density of 90-98% ρ_{th}.[115] They also examined the grain size effect on the dielectric properties of $BaTiO_3$ in their study that the decrease in grain size from 3 to 0.5 μm resulted in a structural change of the material in question from tetragonal to cubic, a.k.a. from ferroelectric to paraelectric.[115] They obtained the highest dielectric constant at 1.4 μm average grain size and showed that the loss tangent decreased with an increase in the density of the sample.

$BaTiO_3$ powder was synthesized at a low temperature value using modified solid state reaction (MSSR) and sintered using microwave sintering method by Sonia et al.[106] Optimum MWS conditions were determined as T= 1100 °C and t= 30 min, and 98% ρ_{th}

was acquired.[106] The dielectric properties were found to be ~2500 and 0.03 for dielectric constant and dielectric loss, respectively.[106] They suggest that the remnant polarization (P_r= ~6 μC/cm^2), coercive field (E_C= ~1.45 kV/cm), and piezoelectric coefficient (d_{33}= 335 pC/N) of the microwave sintered $BaTiO_3$ samples are the self-evident of the outstanding effect of MWS on piezoelectric and ferroelectric properties of $BaTiO_3$.[106]

Kawashima et al. sintered the pellets of the mixture of $BaCO_3$ and TiO_2 powders at 1200, 1250, 1300, 1350, and 1400 °C for 2 hours to determine its reaction behavior.[116] They obtained the highest density of ~85% at ≥ 1250 °C.[116] Grain growth facilitated increase in the piezoelectric constant (d_{33}= ~120 pC/N) was observed on the sample sintered at 1300 °C.[116] The specimen sintered at 1250 °C showed the highest dielectric constant of >2500 among the others at 10 kHz.[116]

Since size effect on the ferroelectricity of $BaTiO_3$ attracts the attention of many researchers, Ying et al. investigated the sintering behavior and dielectric properties of nanocrystalline $BaTiO_3$.[113] They prepared nano-$BaTiO_3$ powder utilizing from a chemical dispersion and physical grinding/mixing process and sintered these samples at a temperature range of 1100-1300 °C within different time spans. A relative density of as much as ~95% was achieved by sintering the newly prepared samples at 1100 °C for 6 hours. Average grain size was found to be as small as 140 nm. Moreover, good dielectric properties, ε_r = 8000 and tanδ= $5*10^{-3}$, were obtained, and they suggested, based on their observations, that high dielectric properties could be acquired at low sintering temperature values when using nano-$BaTiO_3$.

Low temperature sintering of $BaTiO_3$ was achieved by Naghib-zadeh et al. at 900 °C by adding lithium fluoride based sintering additives.[120] They sintered the 2 wt% LiF-$SrCO_3$ doped $BaTiO_3$ at the said temperature for 2 hours and obtained a densification of ≥ 98% ρ_{th}.[120] The dielectric constant and the loss tangent of the sample they sintered under the conditions indicated above was found to be ε_r= 3160 and tanδ= 0.014, respectively.[120] Another finding they had was that the pure $BaTiO_3$ was in tetragonal structure at RT after it was kept at 900 °C for 2 hours, i.e. it showed a phase transformation from cubic to tetragonal, whereas the doped one showed no change.[120]

A sintering method which is a combination of rapid-rate sintering, rate-controlled sintering, and two step sintering was proposed to sinter $BaTiO_3$.[121] This method leads to high density as well as grain growth suppression.[121] Polotai et al. found out in their study that the oxygen partial pressure extremely affects the grain size and density of $BaTiO_3$ that decreasing it from 10^{-1} to 10^{-19} atm yields a significant decrease, from 296 to 137 nm, in the grain size and an increase, from 96.2% to 99.6% ρ_{th}, in the density of the sample as the maximum temperature and heating rate being 1300 °C and 1000 °C/h, respectively.[121]

M'Peko et al. sintered $BaTiO_3$ at 688 °C in one minute under the application of 500 V/cm adopting flash sintering method.[111] Maximum density they obtained was 94% ρ_{th} with a much finer grain size compared to conventional sintering method.[111] The grain size of the samples was as small as 300-400 nm.[111] They found out that higher electric field yields smaller grain size whereas higher current cut-off leads to larger grain size.[111]

Therefore, the relative permittivity is dependent on the applied electric field and the current passes through the sample as it is dependent on the grain size of the sample.[111] The dielectric properties of the sample they sintered under the aforementioned conditions were $\varepsilon`_m = 3.62*10^3$ and $\tan\delta_m = 2.4*10^{-2}$ for maximum permittivity and loss tangent at $T_C$, respectively.[111] The specimen they sintered at 900 °C under 150 V/cm electric field and 60 mA current flow for 15 minutes exhibited the highest dielectric properties of $\varepsilon`_m = 6.05*10^3$ and $\tan\delta_m = 2.2*10^{-2}$ for maximum permittivity and loss tangent at T_C, respectively.[111] The same sample had a density of 97.1% ρ_{th}.[111] However, given the fact that the lower electric field required higher sintering temperature as much as 900 °C and higher sintering time as long as 15 minutes, they determined the optimum flash sintering conditions as 500 V/cm electric field, 60 mA current cut-off, 688 °C sintering temperature, and 1 minute sintering time for their samples.[111]

3. Method of Attack and Experimental Methods

Flash sintering and energy dispersive x-ray diffraction (EDXRD) methods are the main processing and characterization techniques used in this study, respectively. The fact of the ultra-high energy x-ray photons which EDXRD technique provides makes it unrivaled in in-situ experiments which require data collection from the body center of a specimen with a kinetic of ≤5 seconds under several boundary conditions such as thermal and electric fields as in the experiments performed for the present dissertation study. This section deals in detail with BMD setup, EDXRD methods, the way we carried out our experiments using these techniques, and other characterization methods we utilized from.

3.1. The Experimental Setup for Flash Sintering

FS is the main processing method used in the experiments carried out for the present study. An in-house custom made hot stage (HS) was used to apply a dc electric field on the sample of interest while it was being heated. This hot stage was designed as being suitable for in-situ EDXRD experiments. Therefore, it perfectly fits on the positioning stage in front of the beam as enabling one to place the gauge volume (GV), discussed in detail later, at the body center of the specimen. The HS consists of two ceramic insulating plates that one platinum electrode is attached on inner surface of each. The specimen is placed between these electrodes whereby the electric field is directly imposed on it. Insulating plates holding the sample fixed are spring loaded to keep the sample and electrodes in contact in case of any shrinkage in the pellet during densification. The specimen between the plates is resistively heated by a kanthal wire surrounding the plates as seen in Figure 3.1.[12] Electric and thermal fields are provided by two power sources connected to the entire

assembly. Typical heating rate is 15 – 20 °C, and applied electric field is 16 – 320 V/cm depending on the material and experiment. Maximum temperature till which the HS is heated is ~1000 °C.

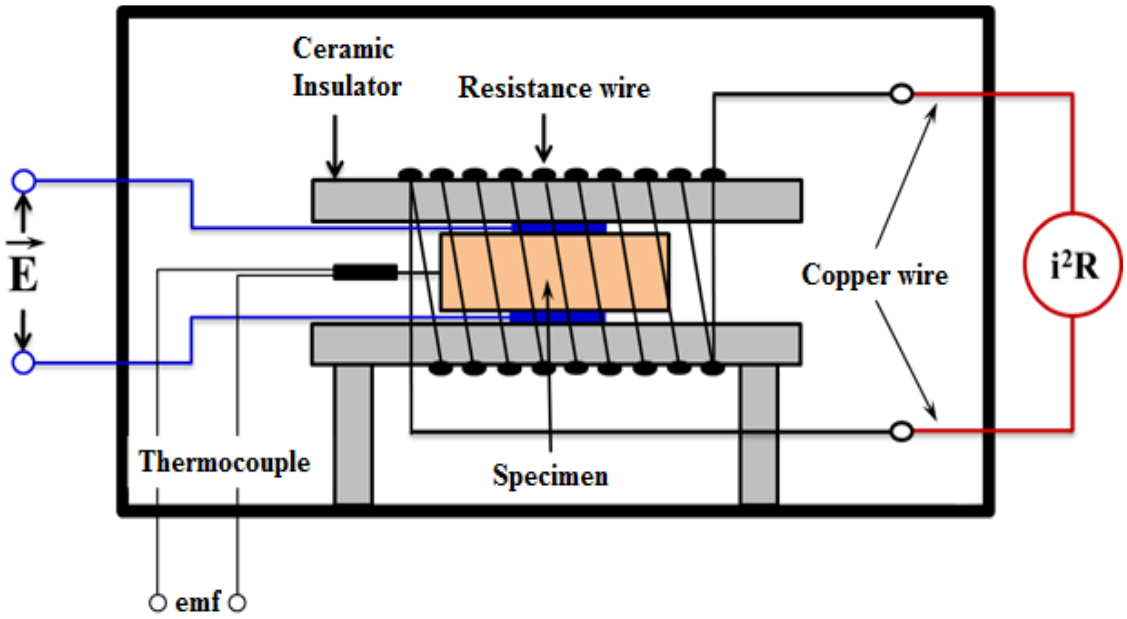

Figure 3. 1. Schematic illustration of the hot stage used in in-situ flash sintering experiments in X17-B1 in NSLS1 of Brookhaven National Laboratory[12]

3.2. Synchrotron Energy Dispersive X-Ray Diffraction

In conventional powder x-ray diffraction instruments, electrons are created in a filament by the application of filament voltage followed by their acceleration as a result of the application of acceleration voltage. These accelerated electrons strike the target as a result of which x-ray radiation occurs. The energy of the x-ray obtained this way is typically 8 keV. In National Synchrotron Light Source of Brookhaven National Laboratories, electrons of 100 keV energy are first generated by a triode electron gun. After that, they are accelerated up to an energy level of 120 MeV followed by a further process boosting them as their energy goes up to 750 MeV. Finally, they are injected into an x-ray ring, so

that their energy reaches 2.584 GeV.[122] Electrons orbit around the final ring and goes under a change in their angular momentum, and this event results in white beam. Comparison of these two methods, in terms of the energy of x-ray photons they provide, reveals that EDXRD is far better than conventional powder x-ray diffraction to conduct in-situ experiments.

All of the energy dispersive x-ray diffraction (EDXRD) measurements were performed in X17-B1 beamline of the Brookhaven National Laboratory's (BNL) National Synchrotron Light Source (NSLS). The frequency of the beam coming from the source is increased by a superconducting wiggler, so a polychromatic x-ray radiation of ultra-high energy photons, as high as 200 keV, is obtained. Figure 3.2 shows the schematic illustration of the particulars of EDXRD.[12] A cryogenically cooled Ge detector was utilized to collect data from the diffracted beam. The EDXRD used in this study is based on Laue mode diffraction (a.k.a. transmission mode diffraction). The sample of interest is placed on a stage which can be positioned in three coordinates by a micropositioner. The gauge volume (a.k.a. diffraction volume) can be placed at the body center of the sample, thereby enabling one to measure the bulk phenomena. X17-B1 beamline enables one to collect data as frequent as 1 second thanks to the super conducting wiggler. In this study, the data collection interval was chosen as ≤ 4 seconds. All experiments were performed in-situ, so that all mass transport phenomena and phase transformations were observed on the spot.

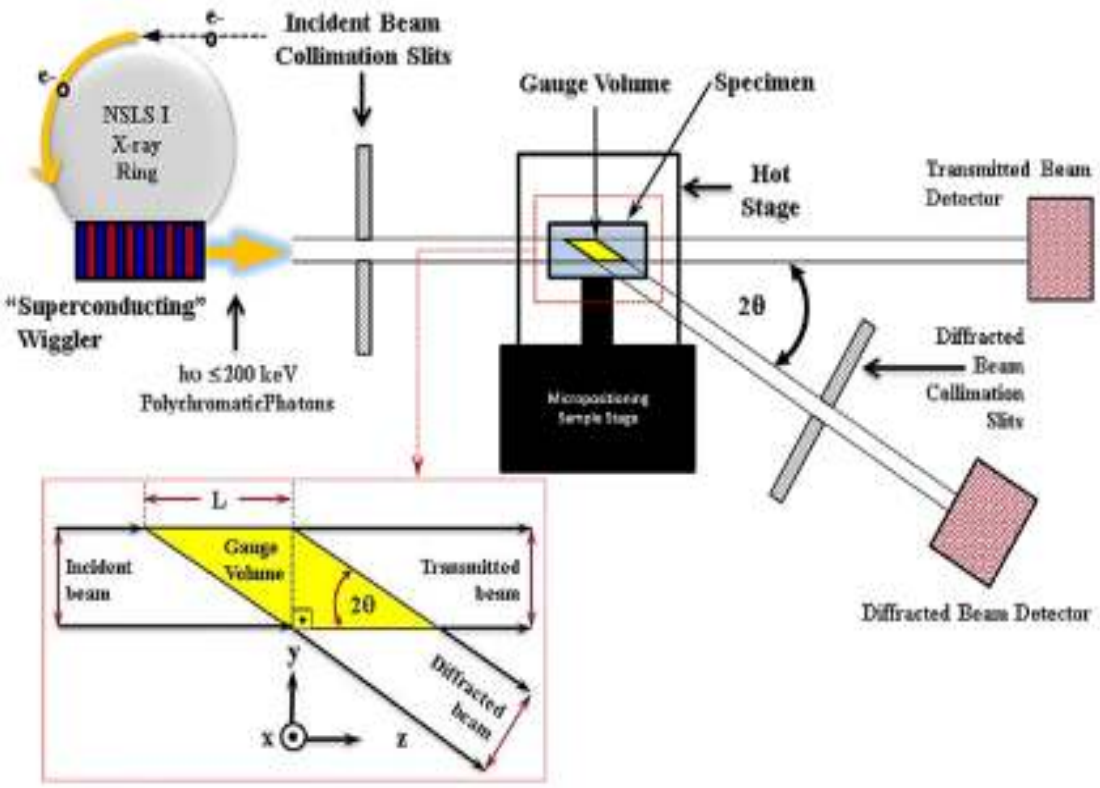

Figure 3. 2. Schematic illustration of Energy Dispersive X-Ray Diffraction[12]

3.3. Data Analysis of EDXRD Experiments

The governing equation for EDXRD technique is obtained by combining Planck Einstein equation[123] $E=h\nu$ (where $\nu=c/\lambda$) with the Bragg's law[124–127] $n\lambda=2d_{hkl}\sin\theta$ as follows;

$$E_{hkl} = \frac{{}^{1}/_{2}\,({}^{hc}/_{\sin\theta})}{|d_{hkl}|} \tag{3.1}$$

where h is the Planck's constant (4.135 x 10^{-15} eV), c is the speed of light (2.9979 x 10^{8} m/s), θ is the Bragg's angle which is always constant in EDXRD unlike Bragg-Brentano technique, d_{hkl} is the interplanar spacing of the (hkl) reflection in Angstrom, and E_{hkl} (in

eV) is the scattered energy from the (hkl) reflection which is directly measured during each experiment. Because $1/|d_{hkl}|$ is equal to $|Q_{hkl}|$ which is the magnitude of the reciprocal lattice vector of the (hkl) reflection, EDXRD method directly measures the changes in the interplanar spacing. Thus, the accuracy of the results obtained by using EDXRD is much higher than that obtained by Bragg-Brentano diffraction method.[126, 128–133] When the constants are substituted in the Equation 2.7, one obtains the final equation as follows;

$$E_{hkl}(\text{keV}) = \frac{6.199}{d_{hkl}\sin\theta} \tag{3.2}$$

The gauge volume has a parallelepiped shape which is controlled by two factors one of which is the Bragg angle and the other one is the slit 1 opening (see Fig. 3.2 and Fig. 3.3). Higher Bragg's angle causes the dimension of the parallelepiped in the transmission direction (a.k.a. gauge length, L) and the intensity to become smaller. The slit 1 can be controlled in –x and –y directions of the coordinate system, so that the dimensions of the rectangular shape of the slit opening on the local area of the specimen from where the data is collected can be adjusted, if necessary, depending on the material being worked on and experiment's purpose. The Bragg's angle was chosen as ~1.5° for the all experiments performed for this study. The slit 1 opening was adjusted as 50 μm x 50 μm for each experiment, unless otherwise specified. The samples used in this study were typically of 2.5 mm - 3 mm thickness and 12 mm diameter, so that the gauge volume was smaller than the dimensions of the sample.

Figure 3. 3. Schematic illustration of the gauge volume geometry at low angles. Slit 1 determines the size of the gauge volume in the –x and –y directions. Slit 2 is completely open with respect to Slit 1 (the same holds true for Slit 4 with respect to Slit 3)

A simple expression for the gauge length (G_L) can be derived with a geometric consideration as follows;

$$G_L = \frac{S3}{\sin 2\theta} + \frac{S1}{\tan 2\theta} \tag{3.3}$$

One can easily identify the phases existing in the material by calibrating the channel number, hence the interplanar spacing and energy. Peak shifts on the spectra we obtained during this study were the self-evident of the expansion in the unit cell volume. The strain occurred during each experiment can easily be calculated using the following equation:

$$\varepsilon = \frac{\text{Channel \# of peak} - \text{Channel \# of peak}_0}{\text{Channel \# of peak}_0} \tag{3.4}$$

Quantitative phase analysis to determine the amount of the oxide phases in each TiB_2 sample was done using integrated intensity of each phase. Although reference

intensity ratio (RIR) was intended to be used at the beginning, small differences and mismatches, as expected, between the pdf cards created using powder x-ray diffraction and EDXRD data led us to do the calculations by dividing total integrated intensity by that of the phase being examined.

Energy calibration for the Ge detector was accomplished by using Ag, Au, Cu, CeO_2, and LaB_6 standards. The peak broadening was measured as $\Delta E/E_0$, where ΔE is the width of the peak examined at half of maximum intensity, and E_0 is the centroid coordinate of the peak. The Ge detector mostly dominates the instrumental broadening with ~1%.[134] Gaussian and pseudo-Voigt profile shape functions were used to measure the centroid and width of each peak used to calculate the crystal parameters, and hence the unit cell volume, using traditional lattice parameter calculations. The unit cell volumes were calculated using $V = a^3$, $V = a^2c$, and $V = \frac{\sqrt{3}}{2}a^2c$ for cubic, tetragonal, and hexagonal structures, respectively.

3.4. Thermodynamic Approach

As an electric field is applied on the sample being attempted to sinter, changes in the current leakage and power are monitored. Power curve, as a function of time, is integrated, and the work done by electric field during the burst (flash) event during which the most of oxidation (in TiB_2) and densification (in $BaTiO_3$) works are done. Since TiB_2 powder used for this study contains considerable amounts of oxide phases, those phases are also included in the calculations. Final temperature in the case of assuming zero heat loss and 100% electric to heat conversion, which actually defeats the second law of

thermodynamics, is calculated using the following equations for TiB_2 and $BaTiO_3$, respectively.

$$W = n\int_{T_0}^{T_f} C_P^{TiB_2} dT \; + n\int_{T_0}^{T_f} C_P^{TiO_2} dT \; + n\int_{T_0}^{T_f} C_P^{TiBO_3} dT \tag{3.5}$$

$$W = n\int_{T_0}^{T_f} C_P^{BaTiO_3} dT \tag{3.6}$$

where W is the work done by applied electric field, n is molar value, C_P is specific heat equation of each material, T_0 is the temperature at which the burst event starts, and T_f is the final temperature value if the applied electric field completely turns into heat.

Although another specific heat equation (Eq. 2.3[4]) of TiB_2 was provided in the scientific background section, Eq. 3.7[135] was used in thermodynamic calculations for correspondence with TiO_2. Due to the lack of information on $TiBO_3$ in the literature, average of Eq. 3.7 and 3.8[135] was used as its specific heat equation (Eq. 3.9). Specific heat equation (Eq. 3.10) of $BaTiO_3$ was obtained using the data reported by Babu et al.[136] All C_P expressions exhibited here are in J/mol K. Approximate molar value of each crystalline phase in a TiB_2 sample is 0.0043, 0.0020, and 0.00123 for TiB_2, TiO_2, and $TiBO_3$ at RT, respectively, and that of $BaTiO_3$ is 0.0043.

$$C_P^{TiB_2} = 56.379 + 25.857 * 10^{-3} * T - 1.745 * 10^{6} * T^{-2} - 3.347 * 10^{-6} * T^{2} \tag{3.7}$$

$$C_P^{TiO_2} = 73.346 + 3.054 * 10^{-3} * T - 1.703 * 10^6 * T^{-2} \quad (3.8)$$

$$C_P^{TiBO_3} = 64.8625 + 14.4555 * 10^{-3} * T - 1.724 * 10^6 * T^{-2} \quad (3.9)$$

$$C_P^{BaTiO_3} = -3 * 10^{-5} * T^2 + 0.0866 * T + 83.042 \quad (3.10)$$

3.5. Post Characterization

Although most of the characterization work was done utilizing from EDXRD, powder x-ray diffraction and scanning electron microscope (SEM) were also used for, especially, post characterization of $BaTiO_3$ samples. Density measurements were made using Archimedes method after each experiment. Piezoelectric coefficient (d_{33}) measurement was also conducted on one sintered $BaTiO_3$ sample.

Due to resolution issues, discussed in detail later, with EDXRD, powder x-ray diffraction became a complementary method to confirm the signs of structural phase transformation observed in EDXRD data of $BaTiO_3$ specimens. Measurements were performed for 5 minutes in Panalytical X'Pert® X-Ray Diffractometer instrument with Cu-Kα radiation of wavelength λ = 1.54059Å. The spectrum obtained after each measurement was analyzed using XRD analysis software, MDI Jade. Each peak on each spectrum was cross-checked with appropriate pdf cards retrieved from this software. Powders and dense $BaTiO_3$ samples were examined using Zeiss Σigma® field emission scanning electron microscope (FESEM) under an accelerating voltage of 5 kV.

Appendix A presents the d_{33} measurement result and its comparison to literature value. It also highlights the challenge of performing reliable electrical properties measurements due to the difficulties having the samples keep their circular shapes.

4. Experiments and Results

This section consists of two main parts. In the first part, Section 4.1, effects of the electric field on TiB_2 are presented, whereas the second part, Section 4.2, deals with the results of the experiments done on $BaTiO_3$.

4.1. Titanium Diboride Study

4.1.1. Preamble

Commercial TiB_2 powder[137] of 58 nm primary particle size as reported by the manufacturer and 125 nm median aggregate (secondary) size as measured by laser diffraction was uniaxially pressed into disks of 12 mm diameter and ~2.5 mm thickness, unless otherwise specified, under 4 tons. SEM image of the powder is seen in Figure 4.1. Typical as-pressed density of such specimens was ~50% ρ_{th}.

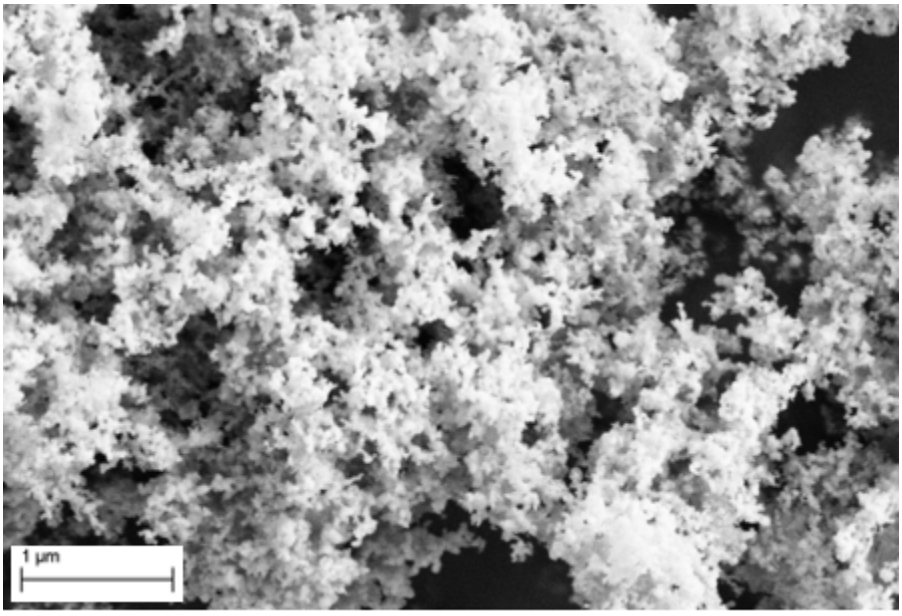

Figure 4. 1. SEM image of as-received TiB_2 powder

In this part of this study, four EDXRD experiments were conducted on TiB_2 specimens. Three different magnitudes of electric field was applied on TiB_2 samples while they were being heated, and the effect of the electric field on the behavior of TiB_2 was determined. Results were compared to those obtained under thermal field alone.

In the following experiments, various magnitude of electric field was applied on TiB_2 samples. Typical electric fields imposed on the specimens were 16 and 40 V/cm for non-isothermal experiments and 45 V/cm for the isothermal experiment. In the non-isothermal experiments, chosen electric field was applied from the beginning of each experiment till the system started to be cooled down. Temperature at which the burst event occurred in each experiment was observed to be different, as expected, depending on the applied field. After a while the burst event occurred in each experiment, samples were cooled down under zero electric field. Data was collected with a frequency $\leq$3 seconds in each experiment. Experiments were carried out in 100% Argon gas flowing at $\geq$1

atmosphere pressure. Also, we have collected x-ray spectra at the beginning and after the completion of each experiment at RT to establish a net footprint of the thermal and/or electrical cycle to which the specimens were subjected.

4.1.2. Experimental Results

Here, the results are organized in four sections in each of which the results of the experiments done under different conditions are presented. Effects of thermal and electric fields on the crystal parameters of TiB_2, phase transformation between oxides existent in TiB_2 samples, and the oxidation of this material are evaluated in detail.

4.1.2.1. Behavior of TiB_2 under Thermal Field

A ~2.5 mm thick specimen was heated with a ~20 °C/min heating rate under zero electric field until its temperature reached 600 °C, and then it was cooled down during which experiment data was collected with Δt=3 seconds, so that we obtained a baseline for the evaluation of the effects of an applied electric field. This experiment was performed under 100% Argon gas flowing as the other experiments. This section exhibits the results on the behavior of TiB_2 under thermal field.

4.1.2.1.1. Effects of Thermal Field on TiB_2 at Unit Cell Scale

Changes in the unit cell of the sample subjected to a thermal field is revealed and interpreted in this section of the present study. As a known fact, the unit cell volume of a material exposed to heat gradually expands as a result of the increase in its crystal parameters. Because TiB_2 has a hexagonal crystal structure, its lattice parameters, a and c,

which are its dimensions in horizontal and vertical directions are of significance. Figure 4.2 shows a gradual increase in the unit cell parameters of hexagonal TiB_2. As the temperature increased from 25 °C to 600 °C, the crystal parameters, a and c, changed from 3.0267 Å to 3.0351 Å and from 3.2255 Å to 3.2420 Å, respectively. This figure reveals that the increase in the parameters were gradual and in an equilibrium state. The changes in the slope of the expansion is simply due to the small changes in the heating rate.

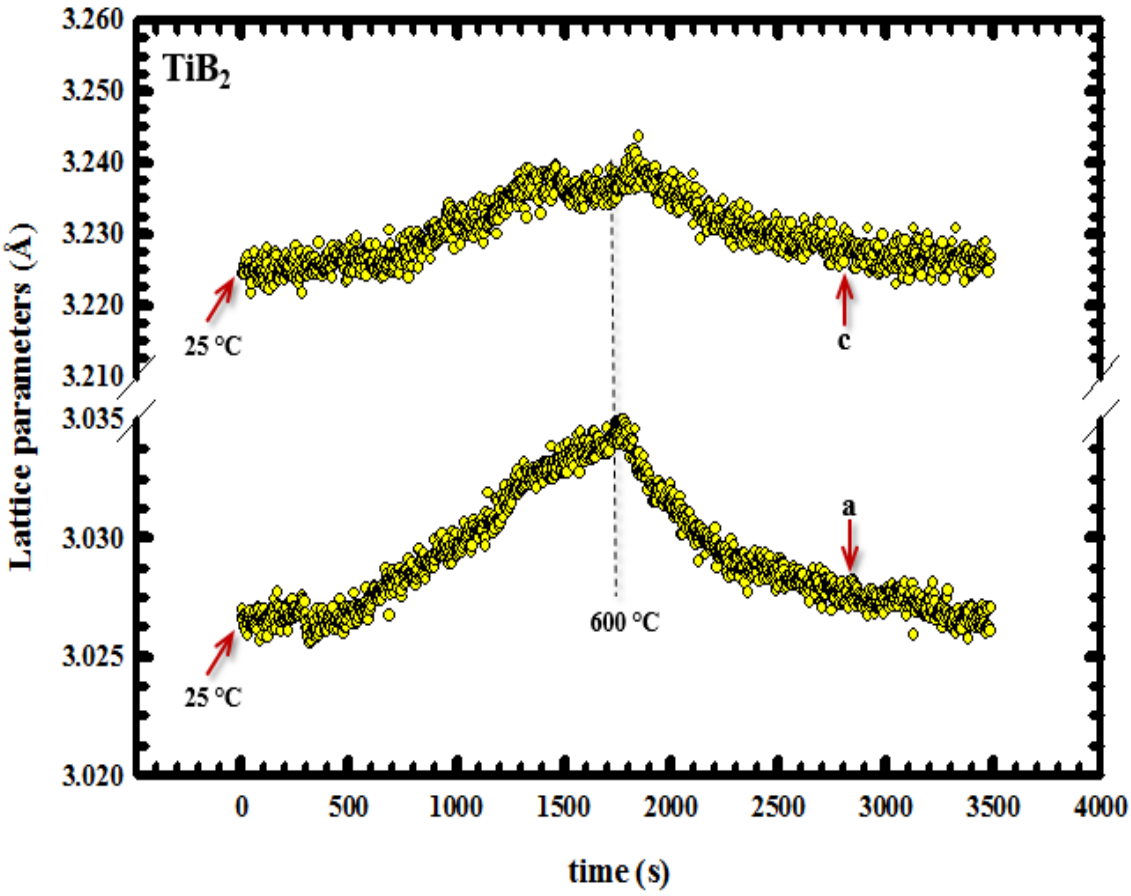

Figure 4. 2. Crystal parameters, a and c, of TiB_2 upon heating

Figure 4.3 illustrates the thermal expansion of the unit cell volume of TiB_2. Unit cell volume tends to expand in a gradual and steady trend with temperature increase as it

is expected. Temperature increased from 25 °C to 600 °C in 1700 seconds, and the total expansion in the unit cell volume was found to be 0.95%, from 25.5899 Å^3 to 25.8330 Å^3.

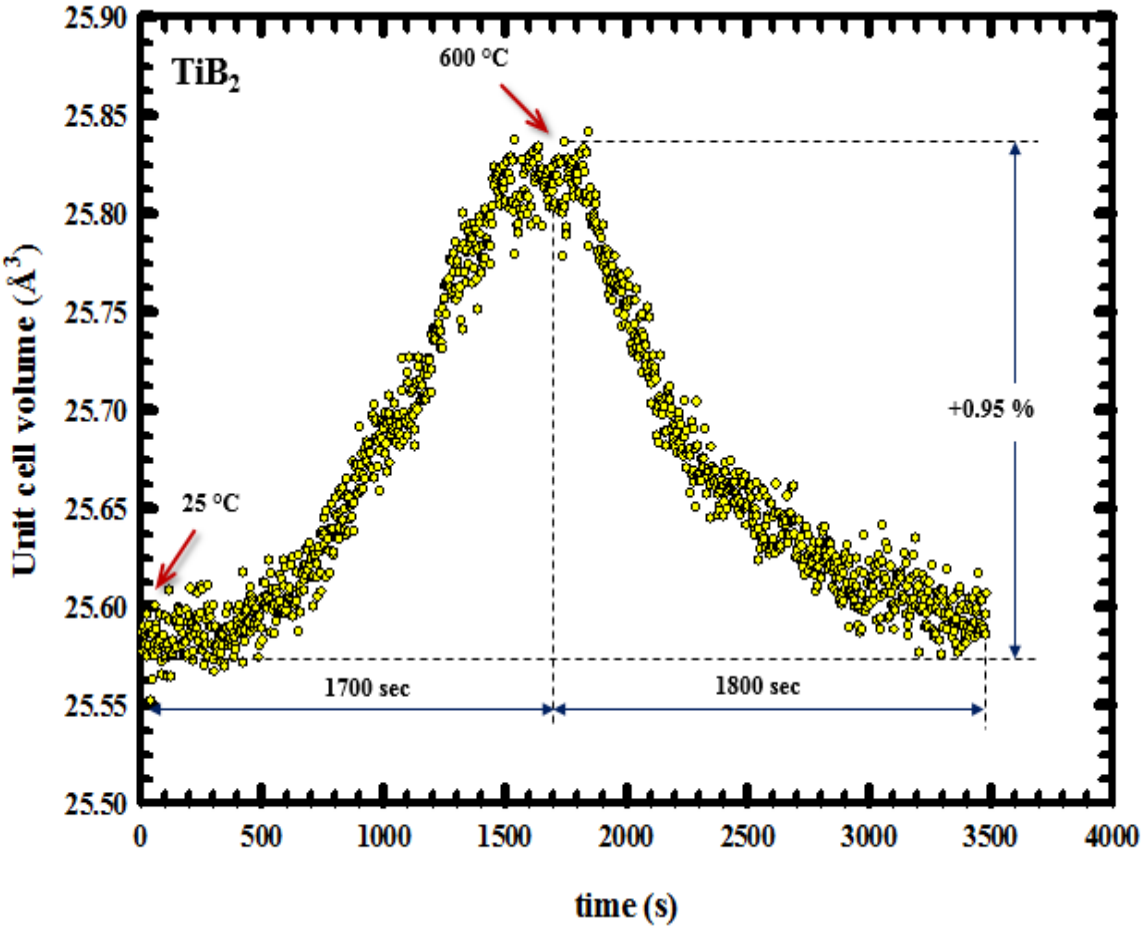

Figure 4. 3. Thermal expansion of TiB_2

Results obtained under applied thermal field revealed that TiB_2 showed no abnormal behavior at atomic scale unlike the TiB_2 samples subjected to electric field which will be discussed in detail in the following parts. No sudden change in the interplanar spacing of the peaks was detected as (100) peak represents in the plot in Figure 4.4. This figure sees three different circumstances which are (i) just before experiment at RT, (ii) when the furnace temperature reaches its maximum of 600 °C, and (iii) after the experiment

at RT. Peak widths (β) are indicated on each peak. As mentioned above, there is no anomalous change in the peak positions, and the peak widths also seem to be almost equal. Since the conventional sintering temperature of TiB_2 is at least 2000 °C, the maximum reached temperature, 600 °C, in this experiment is not high enough for this material to consolidate. The fact that the peak widths showed almost no change supports the previous statement.

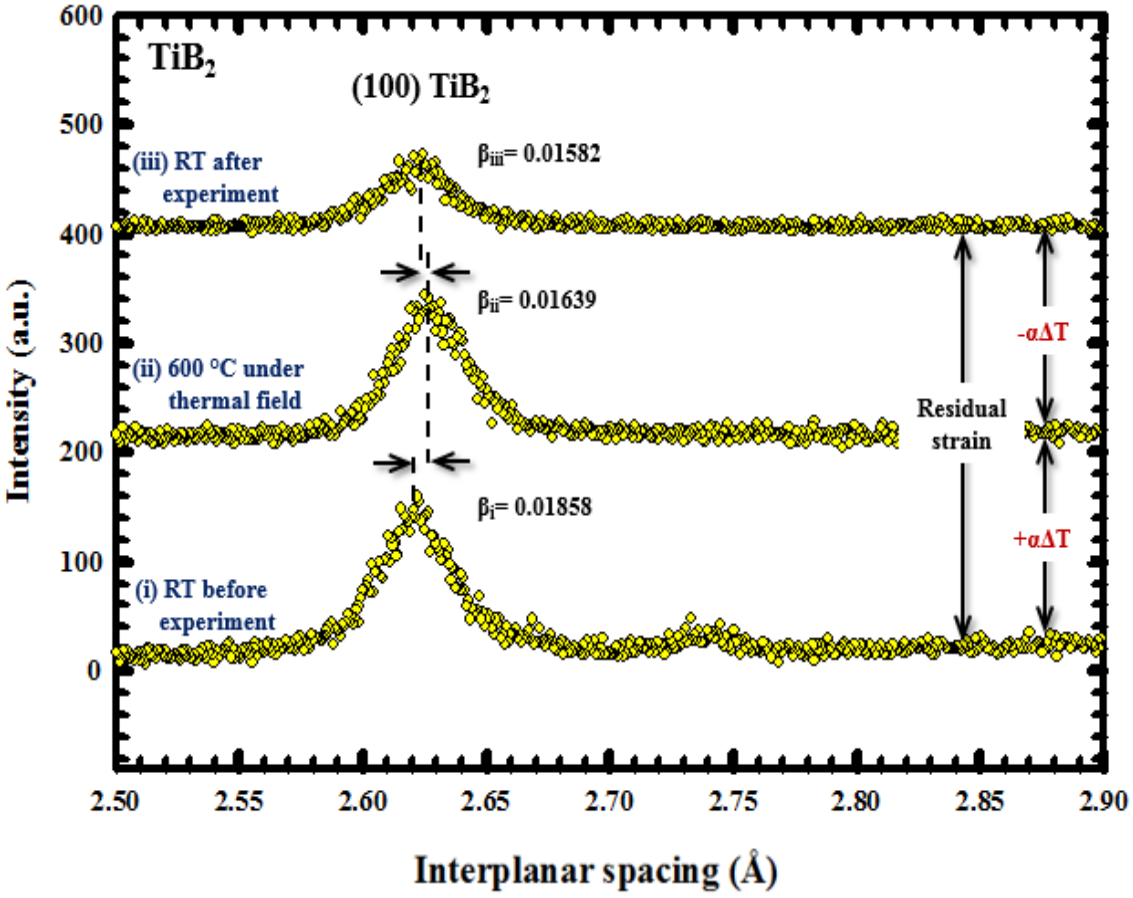

Figure 4. 4. Comparison of the (100) peak position at different temperature values: (i) at RT prior to experiment, (ii) at the maximum furnace temperature, 600 °C, (iii) at RT after the experiment. The residual strain for (100) peak at RT after the experiment is $\varepsilon_{(100)}$= -0.002%

4.1.2.1.2. Patterns of TiB_2 at Different Temperature Values

Examination of oxidation process and the phase transformation between the existing oxides in TiB_2 is one of the main purposes of this dissertation study. The applicability of the flash sintering process to TiB_2 seems to be difficult based on our observations because an applied electric field instigates different mechanisms in the material in question as a result of which new $TiBO_3$ peaks appear on the spectra in as short as 30 seconds. The behavior of TiB_2 under thermal field alone seems to be completely different from that under an applied dc electric field. Since the material subjected to thermal field is not aggressively perturbed, it shows no drastic change. Figure 4.5 depicts the spectra (d spacing vs intensity) of this material taken at different temperatures. $TiBO_3$ (104) peak of very low intensity at RT prior to the experiment completely disappeared at ~160 °C. No drastic and significant decomposition or oxidation is seen on these spectra.

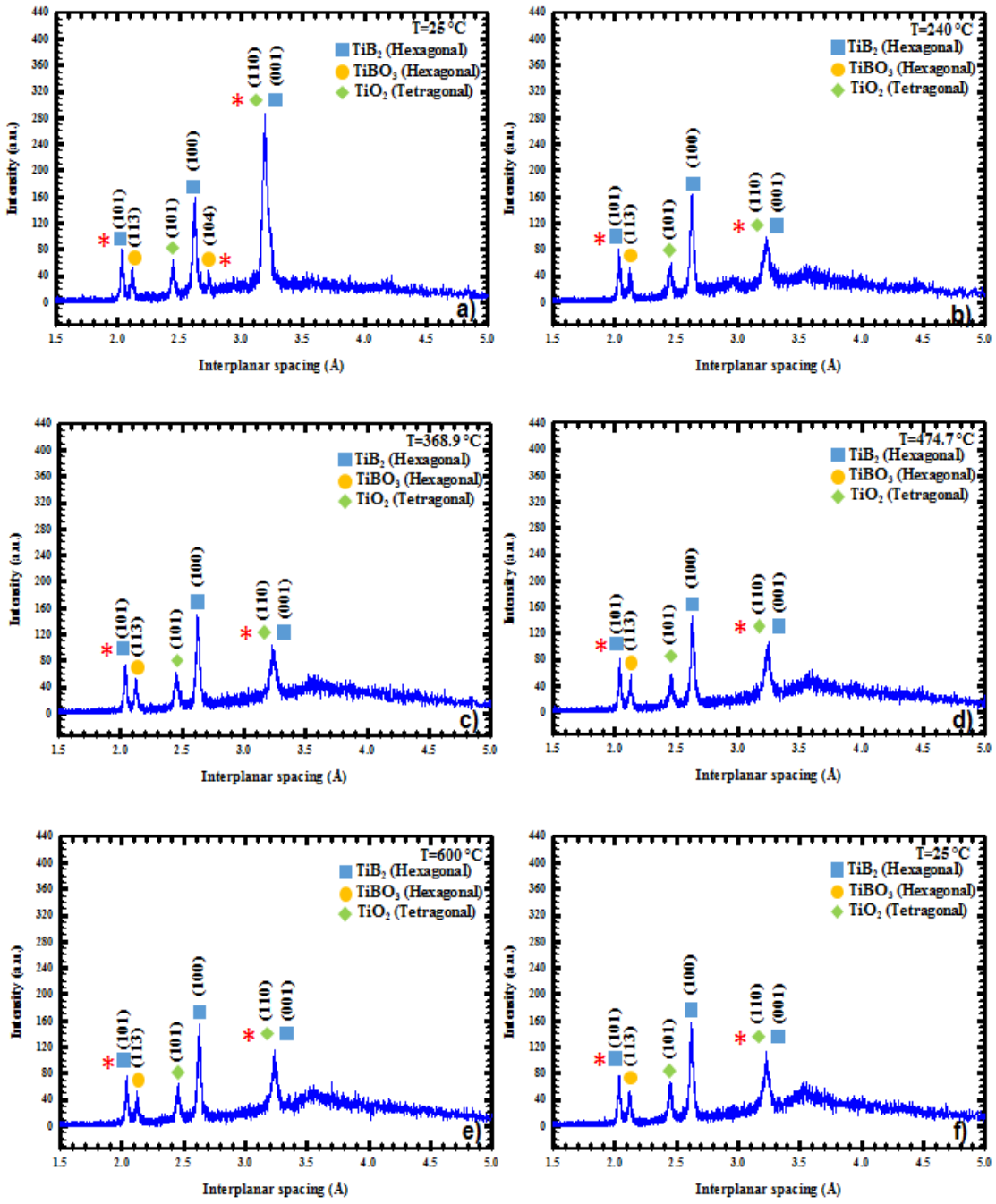

Figure 4. 5. Synchrotron energy dispersive x-ray diffraction spectra of TiB_2 at different temperature values under applied thermal field (* on the spectra represents 100% peaks)

Figure 4.6 shows the hump observed on the spectrum of TiB_2 at RT prior to the experiment as well as at the maximum furnace temperature of 600 °C the system had

reached. As seen in the figure that the hump does not disappear with temperature increase. This hump might be corresponding to amorphous B_2O_3 which is mostly found in the materials such as TiB_2 and ZrB_2.

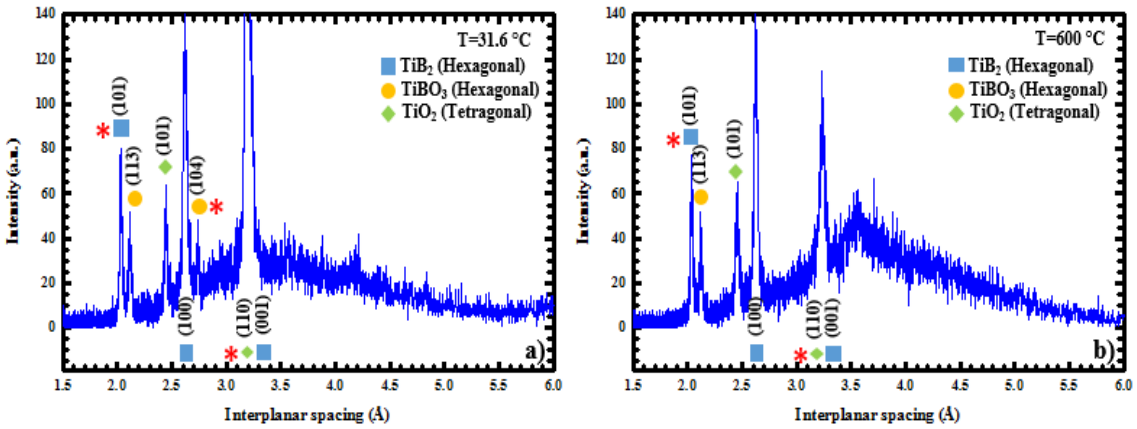

Figure 4. 6. The hump observed at RT and 600 °C (* on the spectra represents 100% peaks)

Figure 4.7 represents 13 spectra taken at different stages of the experiment. This figure exhibits the fact that the material does not go under a drastic change when only thermal field is applied on it.

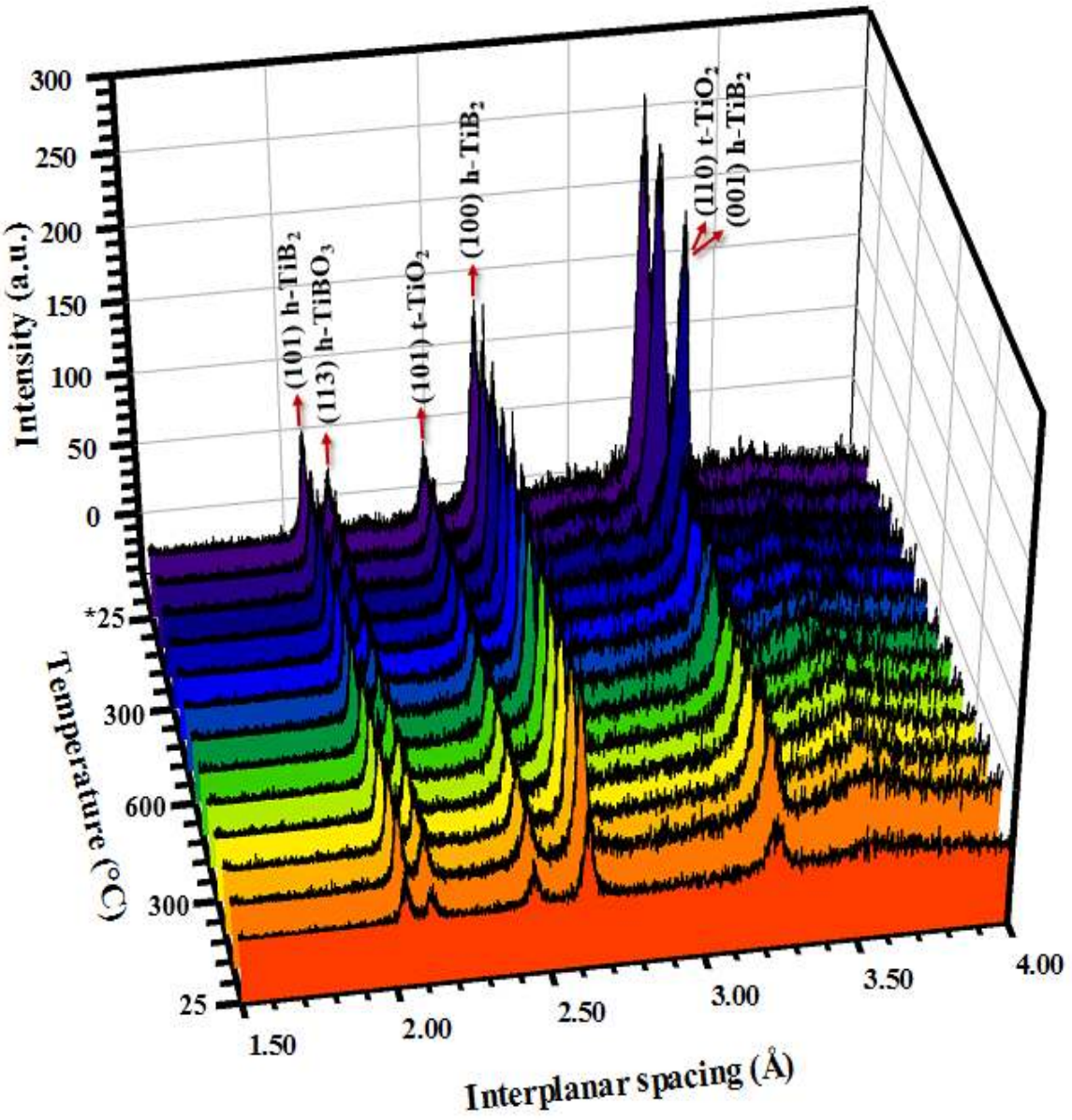

Figure 4. 7. Time-resolved synchrotron energy dispersive x-ray diffraction spectra showing no decomposition or oxidation under thermal field (h: hexagonal, t: tetragonal, * represents the beginning of the experiment)

4.1.2.2. Behavior of TiB_2 under Thermal Field and Non-isothermally Applied 16 V/cm Electric Field

A dc 16 V/cm electric field was imposed on a TiB_2 specimen while it was being heated with a ~20 °C/min heating rate in an inert, Argon, atmosphere. Thermal and electric fields were continuous till the system started to be cooled down. EDXRD data was collected every 3 seconds during the experiment. This section deals with the effects of the said electric field on the crystal parameters and oxidation of the material in question.

4.1.2.2.1. Effect of 16 V/cm Electric Field on TiB_2 at Unit Cell Scale

Figure 4.8 illustrates the effect of an applied electric field of approximately 16 V/cm on the unit cell of TiB_2. Crystal parameters show a sudden rise once the material becomes conductive and the current reaches its maximum. As seen in the figure, the current leakage increases from 0.1A to 4.5A at 520 °C which event is called the burst of charges in the sample. This instantaneous change in the current leakage yields an abnormal activity in the material at unit cell scale. The crystal parameters of TiB_2 increases from 3.0344 to 3.04 and from 3.2384 to 3.2481 for a and c, respectively. A second burst takes place 760 seconds later following the first burst with an increase in the absorbed power by TiB_2. The increase in the lattice parameters of a and c are from 3.0438 to 3.0463 and from 3.2471 to 3.2535, respectively. Time interval at which each burst occurs and results in an instantaneous increase in the crystal parameters is a lot shorter than the required time to obtain the same magnitude of expansion under thermal field alone.

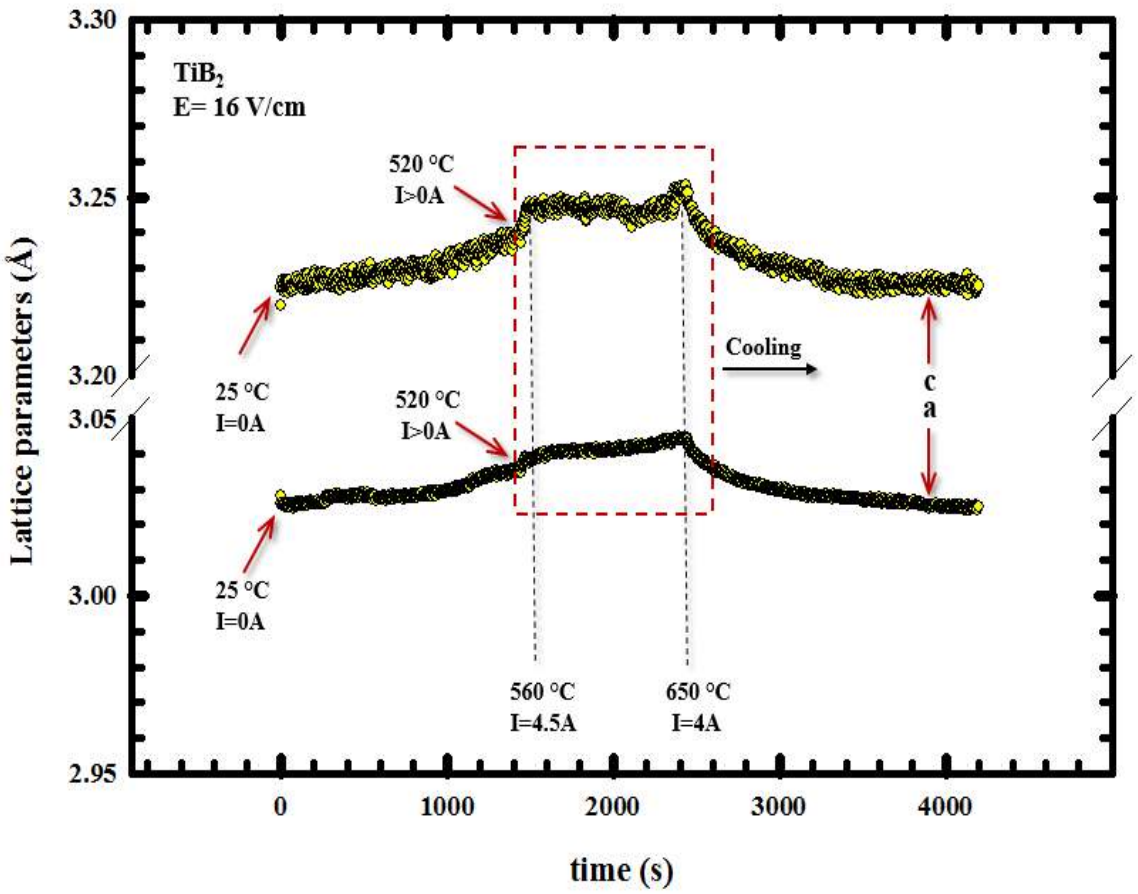

Figure 4. 8. Crystal parameters, a and c, of TiB_2 under thermal field and 16 V/cm electric field

Unit cell volume expansion of TiB_2 under 16 V/cm is depicted in Figure 4.9. Specimen lets the current draw reach from 0.1 A to 4.5 A once the temperature reaches 520 °C, and it shows an abnormal expansion at the unit cell scale. Furnace temperature reaches 560 °C in 150 seconds. Total unit cell volume dilation is 0.6% due to the first burst. 0.43% expansion in the unit cell volume is adiabatically done by the first burst of the charges in ~50 seconds. The following 0.17% of the total 0.60% first abnormal expansion might be due to the Joule heating as well as some other additional processes, such as electromigration, in the material. Therefore, later (0.17%) might be non-adiabatic. The same holds true for the second anomalous expansion as well. The total expansion with the

second burst is 0.41%. However, because this event takes place in over 200 seconds, the effect of the Joule heating on this expansion might be more than that on the first one. Another point we should pay our attention on is the difference between current values during the first and second anomalous unit cell volume expansions. In the first burst of the charges where the material completely became conductive for the first time during the experiment under examination, the current leakage reached its maximum of 4.5A and then decreased and stayed almost stable up until the temperature reached 590 °C. The current value was found to be 2.5A at this point. The second burst which yielded an approximately 0.41% dilation in the unit cell volume occurred at this temperature value as a result of the second sudden rise in the current leakage from 2.5A to 4A. Since the power absorbed by the material is dependent on not only the current but also the voltage, and the power source used to apply the electric field adjusts the voltage value itself depending on the response of the material to the applied field, the expansion values on the graph is not stable and constant.

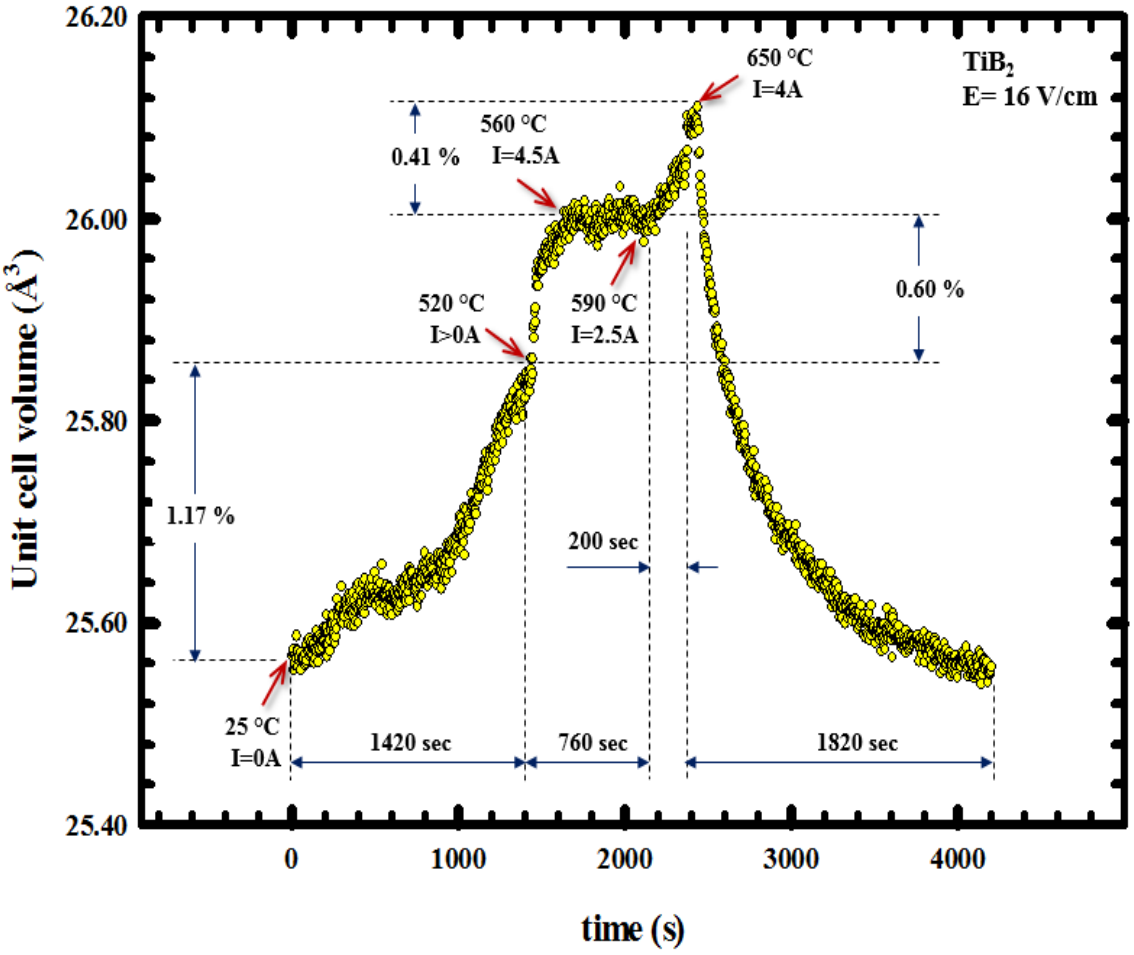

Figure 4. 9. Unit cell volume expansion of TiB_2 under an applied electric field of 16 V/cm and thermal field

Figure 4.10 shows the variation in the interplanar spacing over the sudden rise in the current leakage. As seen in the figure, TiB_2 (100) peak drastically shifts, and its d spacing value exhibits an enormous change as opposed to our observations under zero electric field. Change in the width (β) of the peak being examined is not appreciable that not a worthwhile, but only 10%, densification was obtained. Also a new peak, $TiBO_3$ (104), which did not exist at RT has appeared with the application of a dc electric field. This peak also shifts to the position at which it is supposed to be at RT upon the removal of the electric field. It is a known fact that the oxidation tendency of this material, in

addition to its low self-diffusion coefficient, is responsible for its low sinterability that our study has also confirmed this fact.

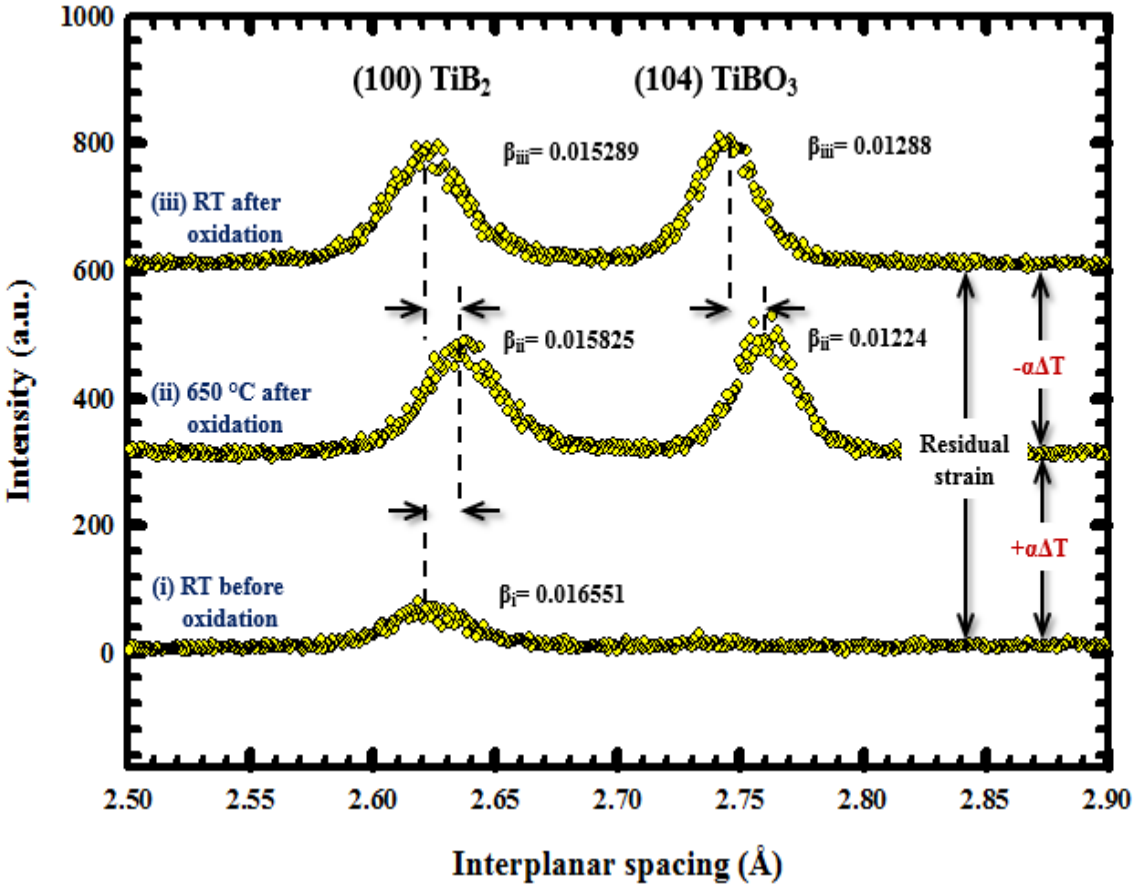

Figure 4. 10. Comparison of the positions of TiB_2 (100) and $TiBO_3$ (104) peaks at different circumstances under 16 V/cm: (i) at RT prior to experiment, (ii) at the maximum furnace temperature, 650 °C, (iii) at RT after the experiment. The residual strain for (100) peak at RT after the experiment is $\varepsilon_{(100)}$= 0.08%

Figure 4.11 represents shifting in the position of the same peak, TiB_2 (100), in detail upon an electric field of 16 V/cm. The effect of, particularly, the first burst on the interplanar spacing of the peak is explicitly seen in the figure.

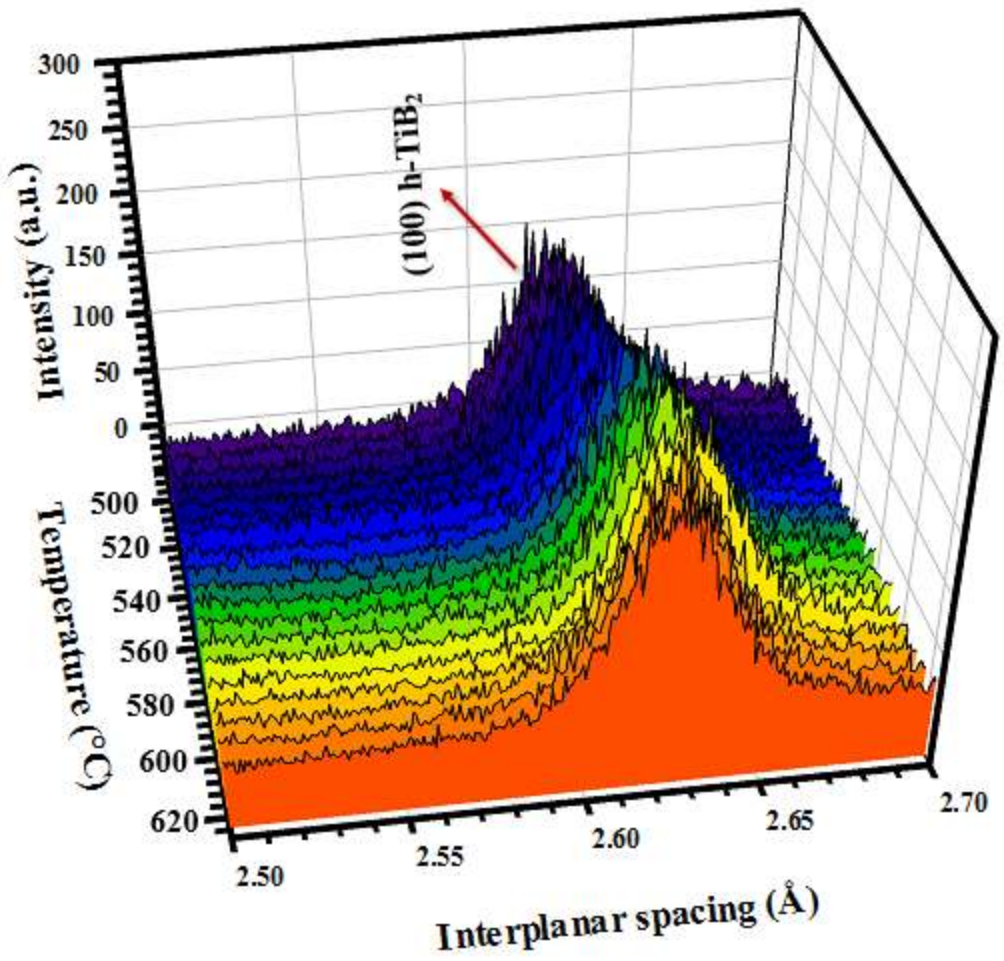

Figure 4. 11. The effect of the burst of charges on the interplanar spacing of TiB_2 (100) peak

4.1.2.2.2. Effect of 16 V/cm on Oxidation and Phase Transformation between Oxides in TiB_2

Sudden rise in the current normally results in density increase in other materials such as YSZ, B_4C, and $BaTiO_3$; however, due to the low self-diffusion coefficient of TiB_2 and high oxidation tendency, it yields oxidation in this material. Oxidation of TiB_2 under different magnitude of electric fields is examined in this study. The lowest electric field we applied on TiB_2 and collected EDXRD data was 16 V/cm. Application of the electric field of magnitude, even, as low as 16 V/cm leaded to oxidation and phase transformation

between existing oxides in TiB_2. Figure 4.12 shows EDXRD spectra of TiB_2 taken at different temperatures. The sample became conductive at a temperature value <500 °C, and the burst took place at 520 °C. One of the most significant observations we made in our experiments was forming of new oxide peaks on the spectra of TiB_2 almost instantaneously while the charges burst into the particles. In this experiment which was carried out under 16 V/cm electric field, the current increased from 0.1A to 4.5A with the first burst. As seen in Figure 4.12, although there is no new oxide peak, specifically $TiBO_3$, on the spectra till 520 °C, $TiBO_3$ (012) peak of very low intensity shows up followed by an intensity increase and the formation and development of some other oxide peaks such as low intensity $TiBO_3$ (110) and high intensity $TiBO_3$ (104). All oxidation process was found to be irreversible, i.e. new oxides do not disappear with the removal of applied electric field.

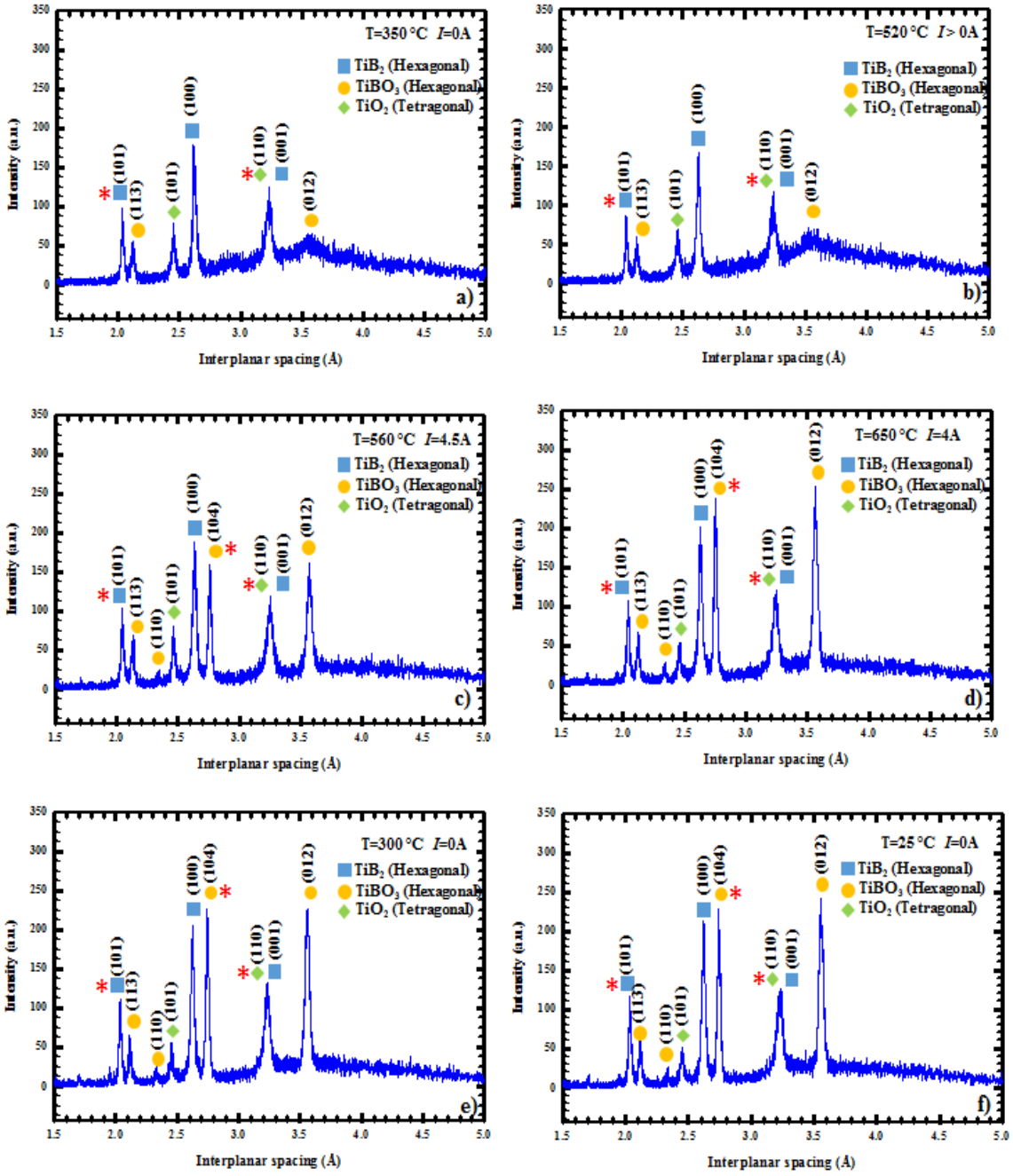

Figure 4. 12. Synchrotron energy dispersive x-ray diffraction spectra of TiB_2 under 16 V/cm electric field in addition to thermal field (* on the spectra represents 100% peaks)

The pre-existent hump at RT before the experiment still exists at 650 °C under 16 V/cm as seen in Figure 4.13. It seems that 16 V/cm has not much effect on the amorphous content in the powder.

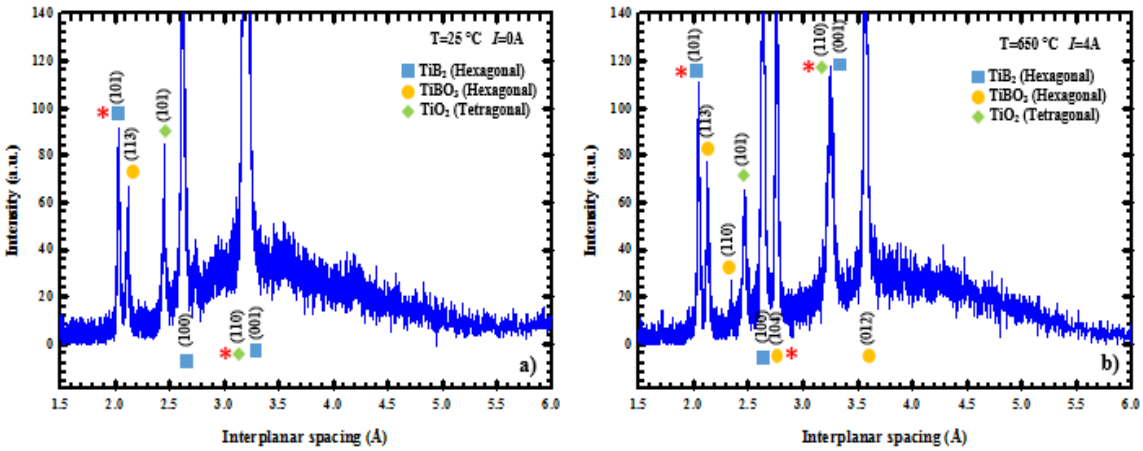

Figure 4. 13. The hump observed at RT and 650 °C (* on the spectra represents 100% peaks)

Figure 4.14 shows the evolution of new oxides under 16 V/cm. As seen in the figure, the oxidation process begins with an increase in the current leakage at 520 °C. Intensities of new phases increase very fast with the first burst, and they become prominent enough at 560 °C. Second increase in the intensities of the peaks occur with the second abnormal expansion in the unit cell volume as a result of an increase in the power absorbed by the sample, i.e. the second burst. The effect of the electric field, even of low magnitude, is clearly seen in this figure that the composition of the phases in the sample completely change because the system is perturbed by an electric field as a result of which it goes under a non-equilibrium condition.

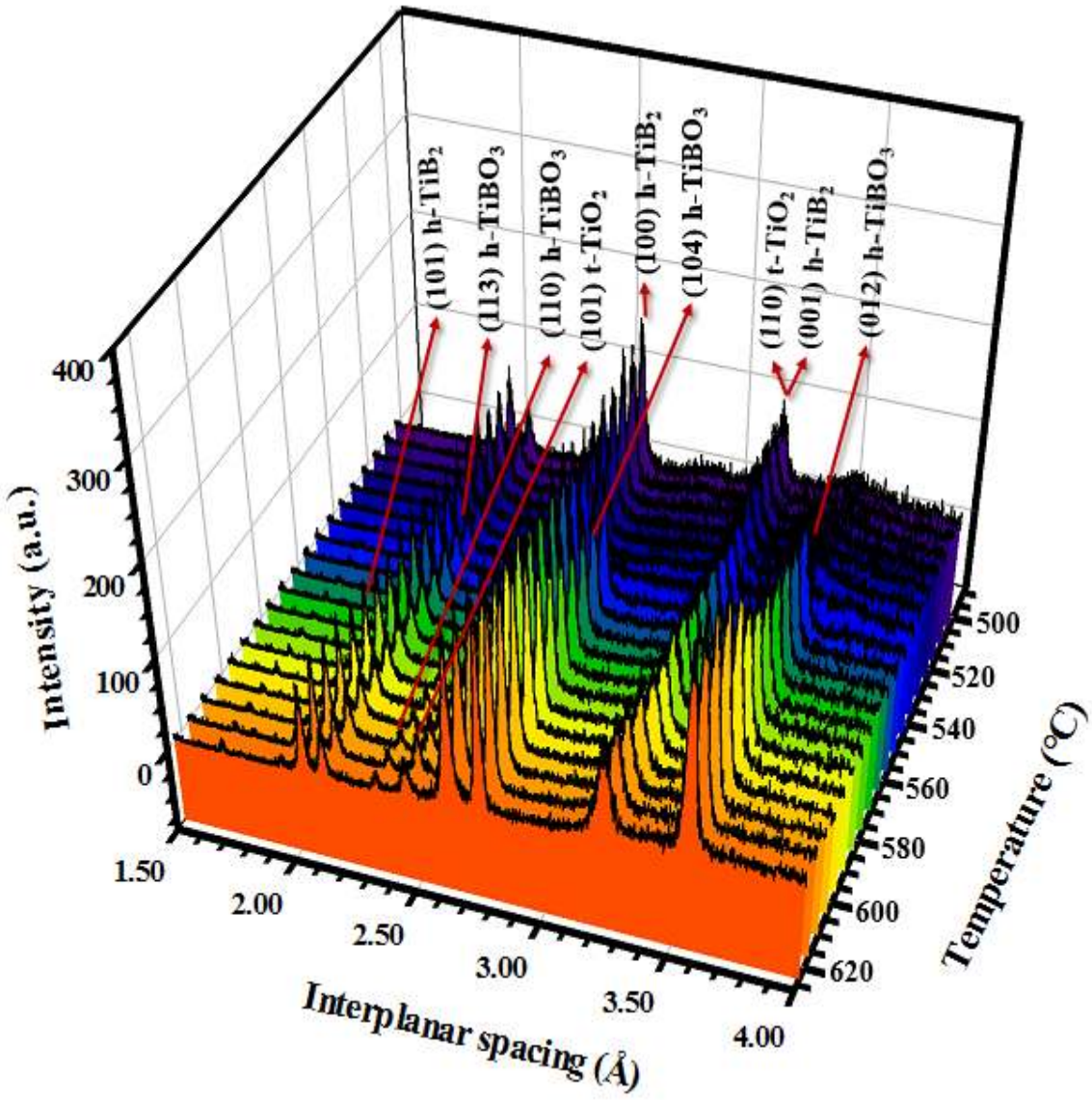

Figure 4. 14. Evolution of the oxide peaks under thermal field and 16 V/cm electric field. New $TiBO_3$ peaks begin forming at 520 °C and their intensities quickly increase in less than a minute. Second burst in the material triggers an increase in the intensities of the new oxide peaks (h: hexagonal, t: tetragonal)

Figure 4.15 shows the quantitative analysis results of the transformation between oxide phases as well as oxidation under applied 16 V/cm dc electric field. This figure exhibits the instant increase in the amount of $TiBO_3$ upon the first burst as well as the second one. Phase composition of $TiBO_3$ increases from 24% to 31% in ~50 seconds due

to the first burst of charges. After that, the amount of $TiBO_3$ in the system keeps increasing slowly. Once the temperature reaches 590 °C, the specimen lets the current leakage increase suddenly again. Therefore, the second burst and as a result of which the second sudden rise in the phase composition of $TiBO_3$ occur as seen in the figure. While the phase composition of $TiBO_3$ increases, that of TiB_2 and TiO_2 decreases due to chemical reaction in the system. The details of the possible reactions yielding oxidation and phase transformation due to the electric field is discussed later in detail. Phase composition of TiO_2 decreases from 27% to 22% in ~50 seconds and keeps decreasing slowly with an increase in the temperature up to 590 °C at which point second sudden decrease in its composition occurs. TiB_2 shows not an abnormal change in its composition due to the first burst, but the effect of the second burst on its composition can clearly be seen in the figure.

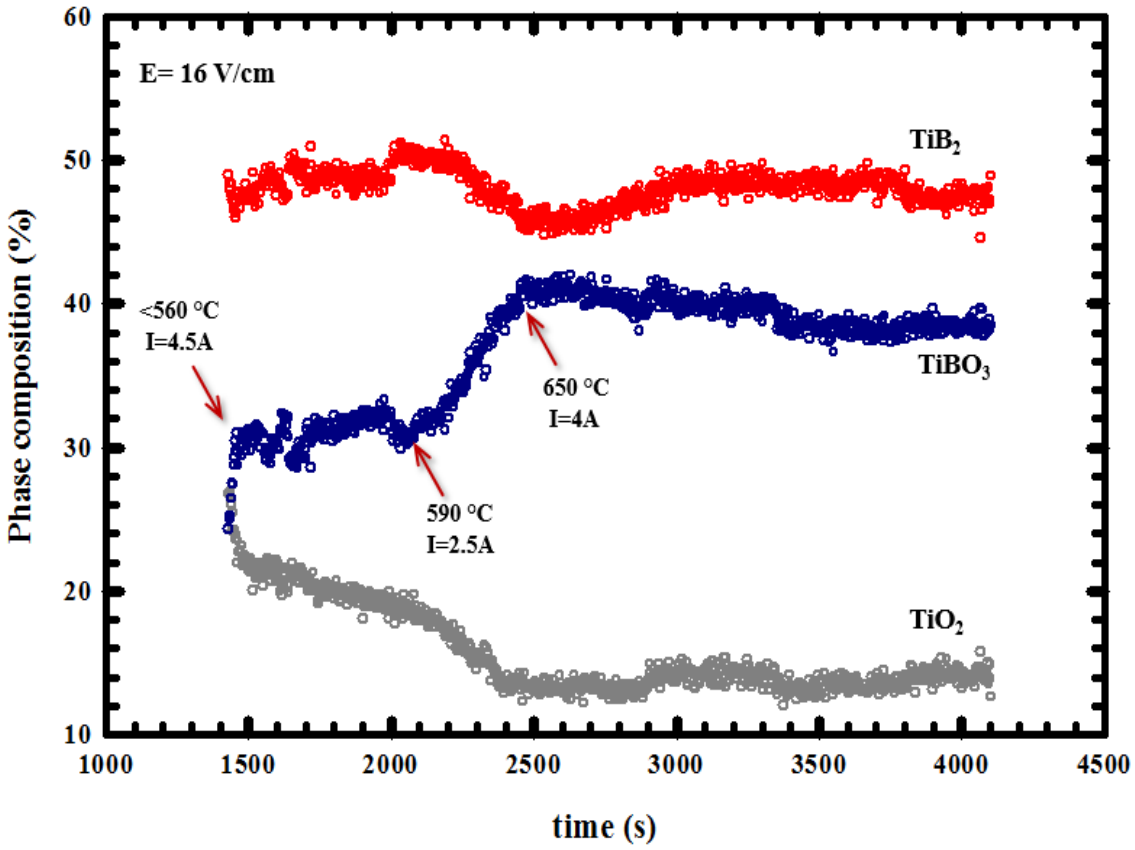

Figure 4. 15. Changes in the composition of each phase existing in a TiB_2 specimen upon 16 V/cm applied electric field

4.1.2.2.3. Thermodynamic Approach to the Burst Event in TiB_2 under 16 V/cm Electric Field

Figure 4.16 illustrates the response of a TiB_2 sample to 16 V/cm electric field and the changes in the power imposed on the specimen. Since all experiments were carried out in current control mode, power sources adjusted the voltage depending on the changes in the current flow at different stages of the experiments. As seen in the following figure, there are three stages occurring under thermal and electric fields which are named as incubation, onset, and burst where the oxidation takes place in. No electric field is observed in the incubation stage. In the onset stage, the material becomes conductive, but the current

leakage flowing through the sample is not high enough to instigate densification (in most materials) or oxidation (in TiB_2). In the burst stage, which is named after the burst of the charges, the current as a result of which the power increases to its maximum in a very short time. The most of the work of phase transformation and oxidation is done in this stage. The current increases from 0.12 A to 4.5 A in 51 seconds as a result of which the power rises from ~0.5 W to 18 W.

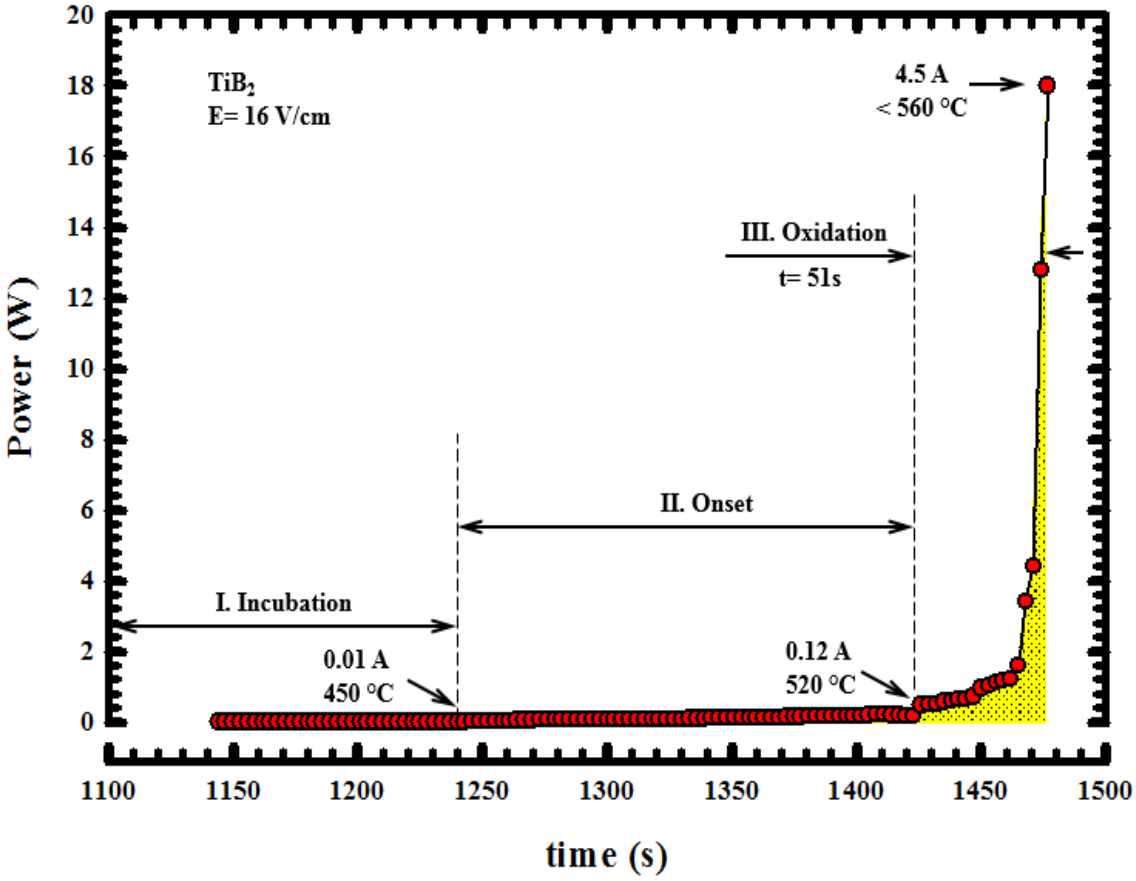

Figure 4. 16. Power (W) vs time (s) graph obtained under 16 V/cm electric field

Integration of the area highlighted by yellow color in the above figure yields the work (124.392 Joule) done by 16 V/cm electric field. Assuming 100% electric to heat

conversion, which is normally impossible to be true, final internal temperature of the sample should be 740 °C based on the solution of Equation 3.5 for the power curve in Fig 4.16.

4.1.2.3. Behavior of TiB_2 under Thermal Field and Non-isothermally Applied 40 V/cm Electric Field

40 V/cm electric field was applied on a TiB_2 specimen which is same in size with the ones used in other experiments. This magnitude of electric field was imposed on the specimen from RT till the furnace reached its maximum temperature of ~500 °C during the experiment. This experiment was carried out in an inert atmosphere as the other ones. Data collection was done with a kinetic of Δt= 2 seconds. System was cooled down under zero thermal and electric fields. This section reveals the results of the experiment done under the said conditions.

4.1.2.3.1. Effect of 40 V/cm Electric Field on TiB_2 at Unit Cell Scale

Figure 4.17 illustrates the behavior of crystal parameters under 40 V/cm electric field while it is being heated. Electric field is applied from the beginning of the experiment at RT till the system is started to be cooled down. The material becomes conductive under 300 °C, and the burst, i.e. the sudden rise in the current leakage, takes place at 305 °C temperature value. Current draws 0.1 A at 305 °C whereas it reaches 10 A in 38 seconds after the burst at 375 °C. The earlier burst observation, compared to the experiment performed under 16 V/cm, is an explicit result of the difference between the applied electric fields. Lattice parameters, a and c, increase from 3.0432 Å to 3.0570 Å and from 3.2575 Å

to 3.2670 Å, respectively. Another increase in the crystal parameters is observed at 458 °C. Joule heating might have a small contribution to the temperature increase in the system.

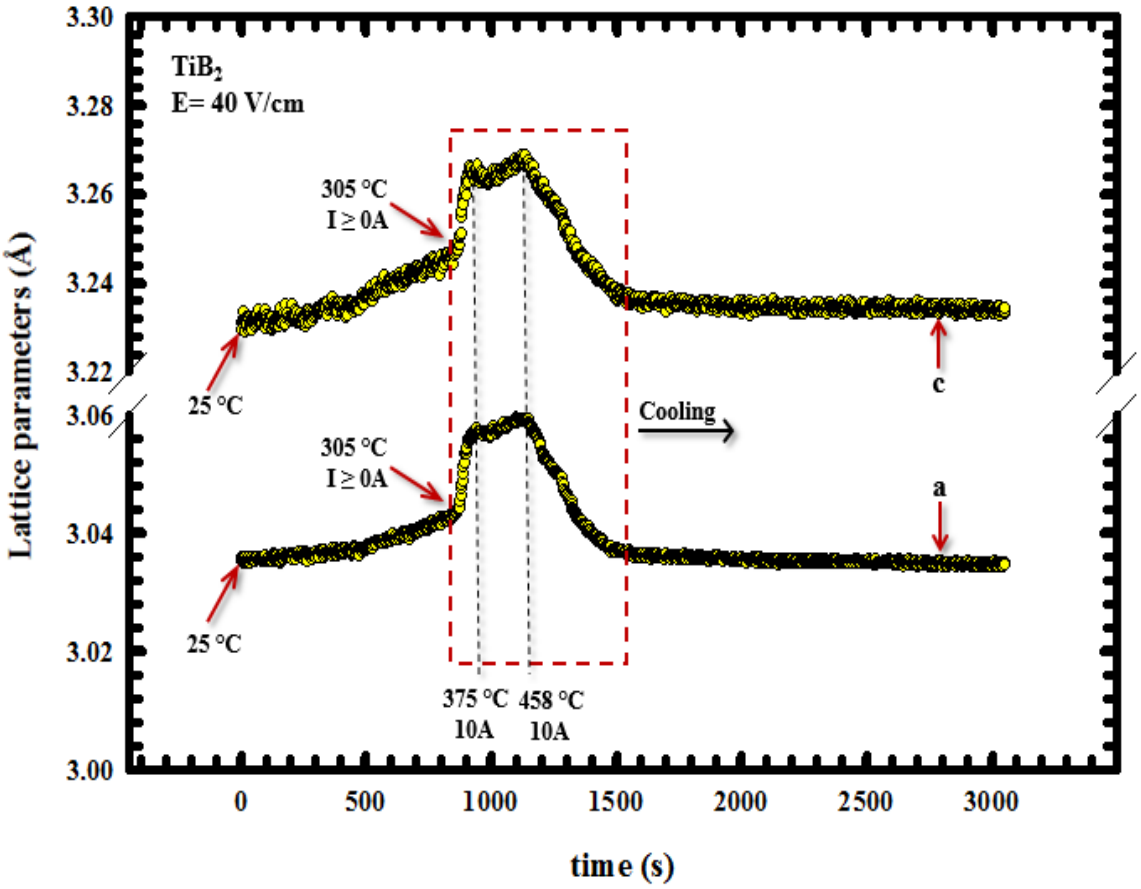

Figure 4. 17. Crystal parameters of TiB_2 under heat and 40 V/cm dc electric field

Unit cell volume expansion of TiB_2 under the application of 40 V/cm dc electric field is shown in Figure 4.18. As mentioned earlier, the specimen on which 40 V/cm electric field is applied becomes conductive before the temperature reaches 300 °C, and the burst of the charges occur at 305 °C as a result of which the unit cell volume exhibits an anomalous expansion. Furthermore, it expands in a steady state by 1.12 % in 873 seconds from RT to 305 °C under the effect of largely thermal field; however, the sudden

rise in the current leakage from 0.1 A to 10 A in 38 seconds instigates an abnormal dilation in the unit cell volume by 1.42% as seen in the figure. Another abnormal increase in the unit cell volume occurs 199 seconds later the first burst, but the magnitude of the second expansion, 0.38%, is much lower than the first one. Since the second abnormal expansion due to the increase in the power absorbed by the specimen follows a more linear behavior and takes more time compared to the first one, this expansion might be attributed to the Joule heating. The furnace temperature after the second expansion is 458 °C. The system was started to be cooled down at a temperature value <500 °C.

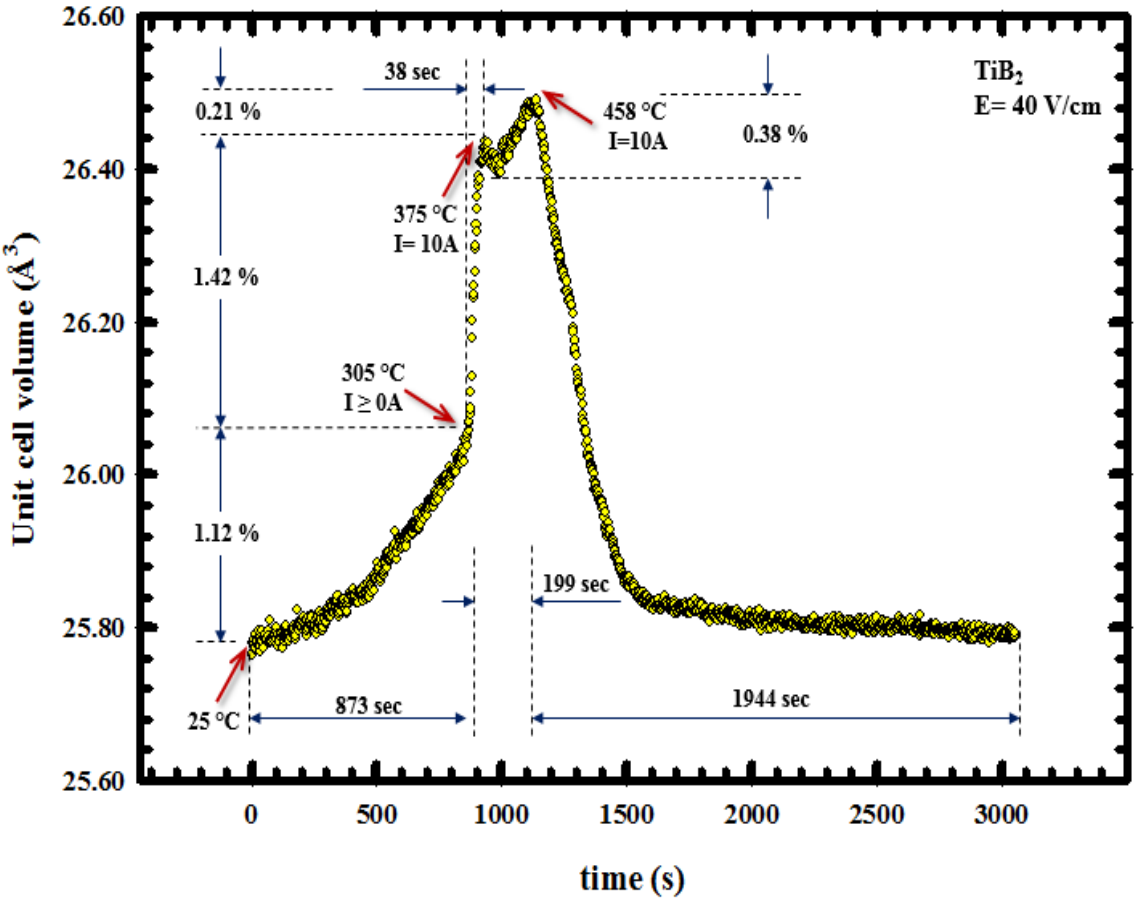

Figure 4. 18. The behavior of unit cell volume of TiB_2 under an applied electric field of 40 V/cm and thermal field

Figure 4.19 exhibits the shifting in the positions of TiB_2 (100) and $TiBO_3$ (104) peaks. Peak width (β) of each peak at different stages of the experiment is presented on each peak. A little decrease in the said property is observed upon applied electric field. $TiBO_3$ (104) peak pops up on the spectrum with the increase in the current leakage. A shifting to where it belongs to at RT occurs with a decrease in the furnace temperature.

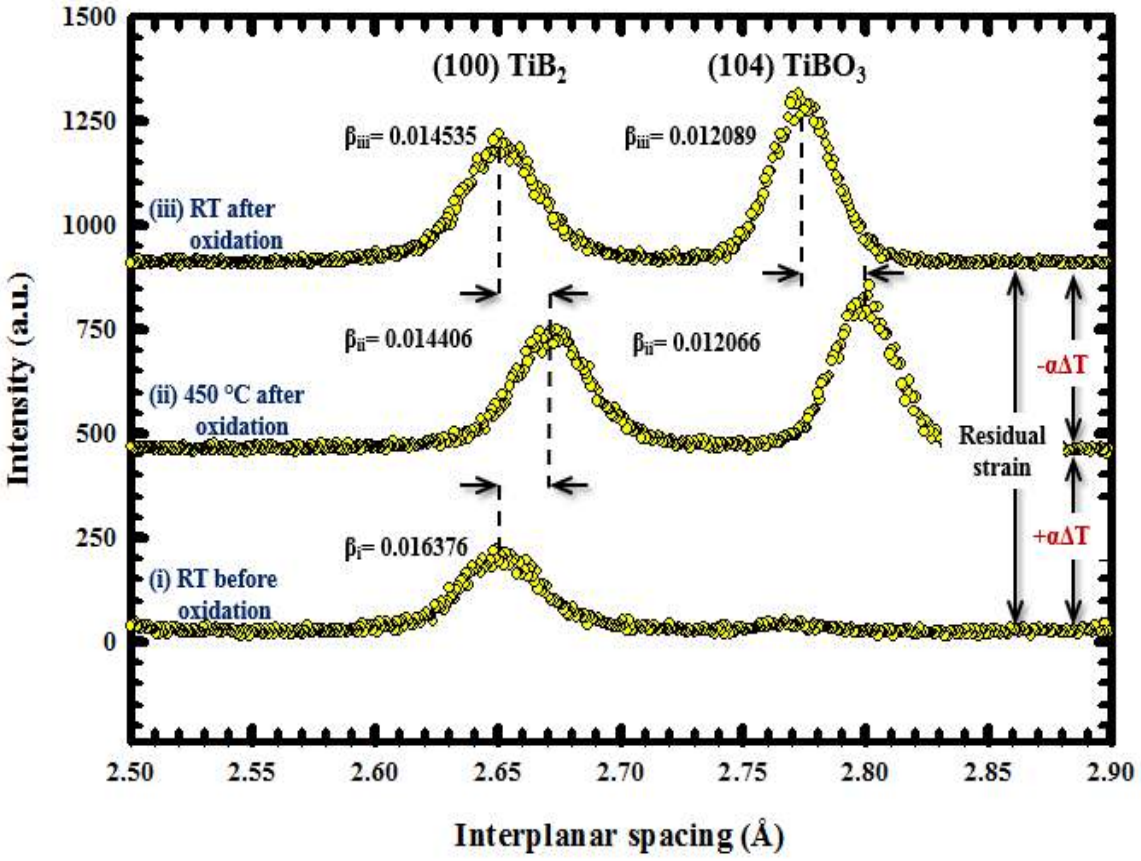

Figure 4. 19. Changes in the interplanar spacing of TiB_2 (100) and $TiBO_3$ (104) peaks at different stages of the experiment conducted under 40 V/cm electric field: (i) at RT prior to experiment, (ii) at a high furnace temperature, 450 °C, (iii) at RT after the experiment. The residual strain for (100) peak at RT after the experiment is $\varepsilon_{(100)}$= 0.06 %

Shifting in the position of TiB_2 (100) peak under 40 V/cm electric field is seen in detail in Figure 4.20. The burst mode occurs at ~305 °C, and the temperature reaches 375

°C at the end of the event. The peak under examination, as well as the other ones, shifts anomalously during the burst event as seen in the figure.

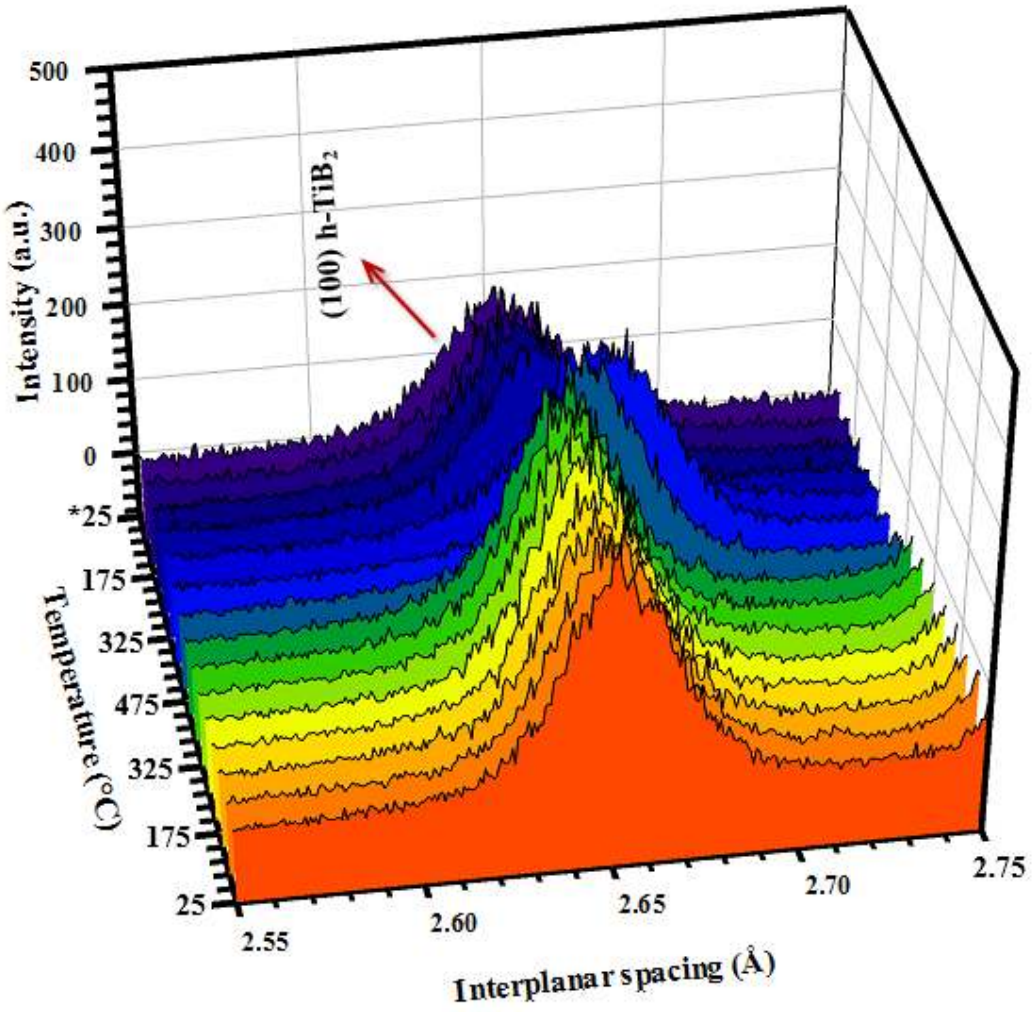

Figure 4. 20. Shifting in the position of TiB_2 (100) peak upon the burst under 40 V/cm (* on the axis represents the beginning of the experiment)

4.1.2.3.2. Effect of 40 V/cm on Oxidation and Phase Transformation between Existing Oxides in TiB_2

Figure 4.21 shows different spectra taken at different circumstances during the experiment carried out under the influence of 40 V/cm and thermal field. This figure shows

that no new peak appears on the spectrum till 300 °C. However, new oxide peaks, $TiBO_3$ (012) and $TiBO_3$ (104), show up on the spectrum over the said temperature as a result of the burst, i.e. the increase in the current flow from 0.1 A to 10 A. Intensity of $TiBO_3$ (104) quickly increases and reaches almost that of the major peak TiB_2 (100) in 38 seconds. It, then, dominates all other peaks, including the host TiB_2 peaks, on the spectrum in a while and becomes the strongest one with the highest intensity as a result of the applied electric field. Intensity of $TiBO_3$ (012) also increases very fast and becomes one of the three strongest peaks exist on the spectrum. TiO_2 (101) peak existing at RT disappears with the application of 40 V/cm electric field.

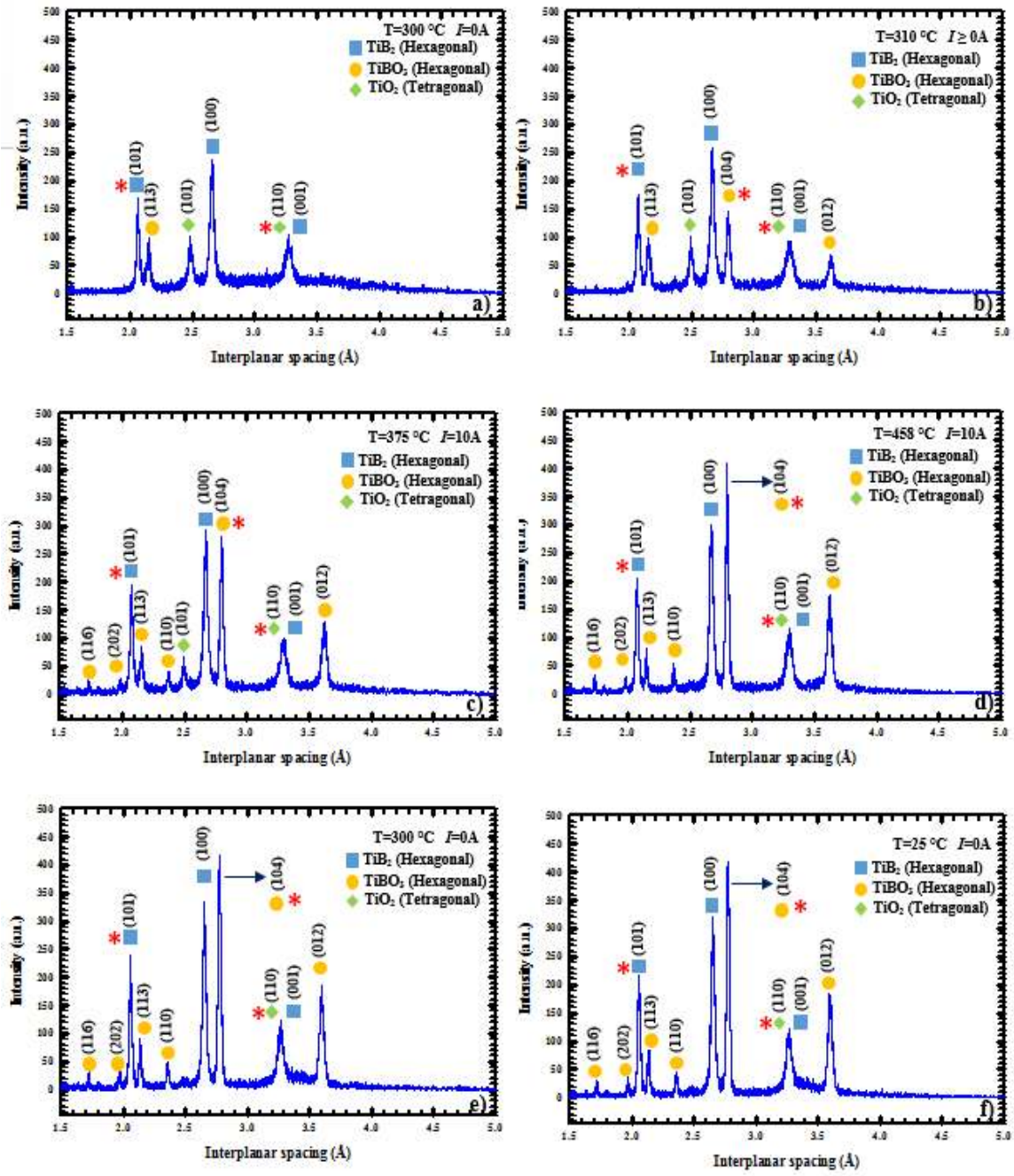

Figure 4. 21. Synchrotron energy dispersive x-ray diffraction spectra of TiB_2 taken at different circumstances during the experiment under 40 V/cm electric field as well as thermal field (* on the spectra represents 100 % peaks)

Figure 4.22 illustrates the insets of the spectra taken at RT and 458 °C. The hump observed on the spectrum at RT disappears once the material becomes conductive and the burst mode takes place under the influence of 40 V/cm dc electric field.

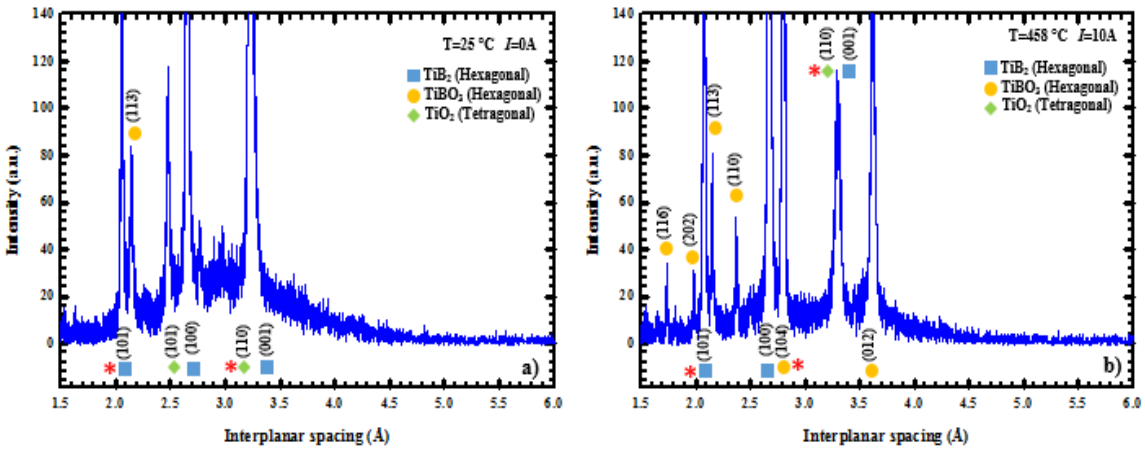

Figure 4. 22. Insets of the spectra of TiB_2 at **a)** RT and **b)** 458 °C. The hump existing at RT disappears upon an electric field of 40 V/cm (* on the spectra represents 100 % peaks)

Formation of new oxide peaks is shown in detail in Figure 4.23. New peaks corresponding to the $TiBO_3$ phase start forming over 305 °C with a sudden rise in current leakage, from 0.1 A to 10 A. As seen in the figure and mentioned earlier, their intensities increase quickly, and $TiBO_3$ becomes the major phase in the specimen. Also TiO_2 (101) peak existing at RT disappears after an increase in the current flowing through the material due to the burst event.

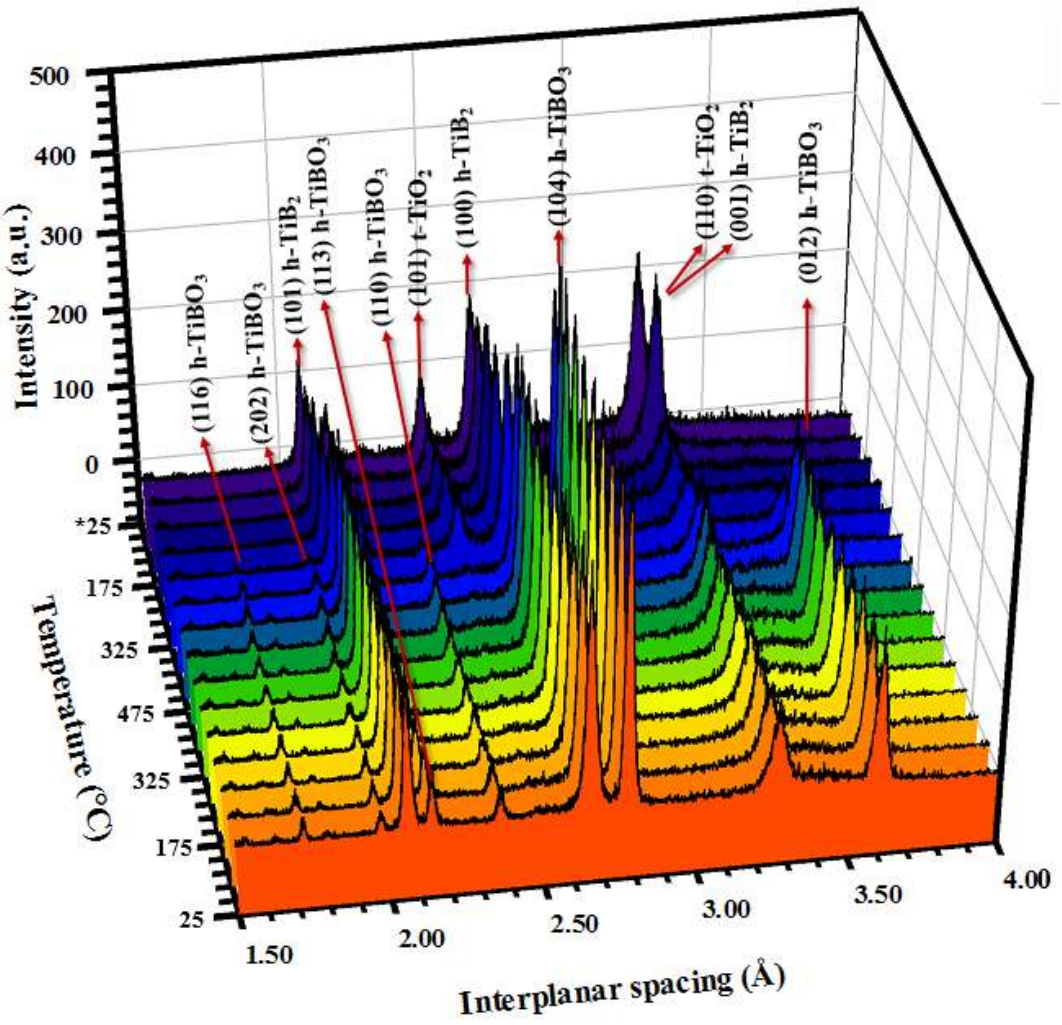

Figure 4. 23. Formation of the oxide peaks under thermal and 40 V/cm electric fields. The burst event occurs when the temperature reaches 305 °C, and the new peaks begin forming as a result of an anomalous increase in the current flow from 0.1 A to 10 A (h: hexagonal, t: tetragonal)

The effect of the applied electric field of 40 V/cm can be seen in Figure 4.24 by a sharp change in the compositions of $TiBO_3$ and TiO_2. The composition of $TiBO_3$ increases from 18% to 38% in 38 seconds. Then, it keeps increasing as the current keeps flowing through the sample. $TiBO_3$ exhibits another sudden increase in its composition with the second burst which is much less than the first one. On the other hand, TiO_2 shows a sharp decrease in its composition upon the burst event. It decreases from 32% to 12% as a result

of the first burst and keeps decreasing slowly till the second burst where it completely transforms to $TiBO_3$. While anomalous changes in the compositions of oxide phases occur in the system, TiB_2 exhibits less change though it is also affected by each burst as seen in the figure.

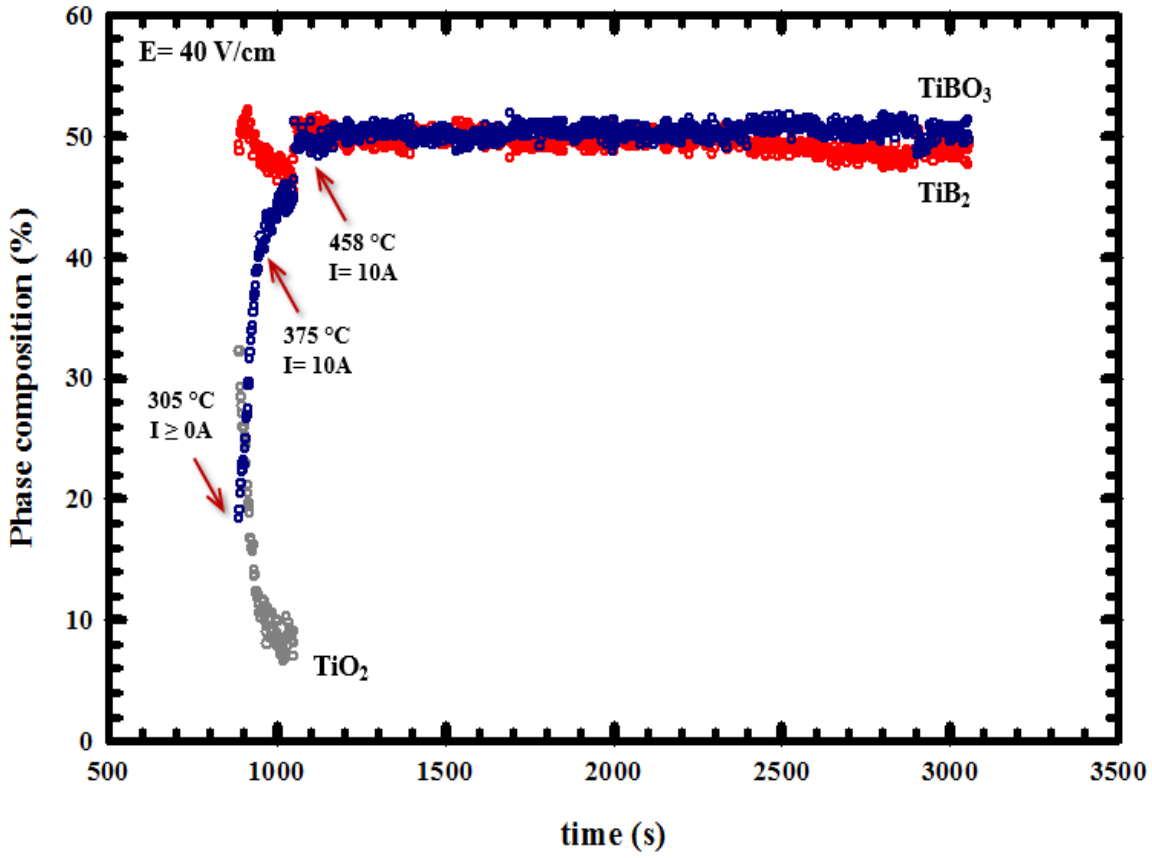

Figure 4. 24. Changes in the phase composition in the specimen subjected to 40 V/cm applied electric field

4.1.2.3.3. Thermodynamic Approach to the Burst Event in TiB_2 under 40 V/cm Electric Field

Figure 4.25 depicts the changes in the power imposed on the specimen under 40 V/cm electric field. The burst event starts at 305 °C, and it takes 38 seconds for the current

to reach its maximum value of 10 A. The onset begins at 280 °C till which no current flow is observed in the system. The power on the specimen increases from ~0.6 W to 100 W with the sudden rise in the current leakage, so that the most of the work for phase transformation between the oxides is done in this time span. The work done by the electric field is found to be 297 J from the integration of the area under the power curve, and the theoretical internal temperature limit for the specimen is calculated as 842 °C using Equation 3.5.

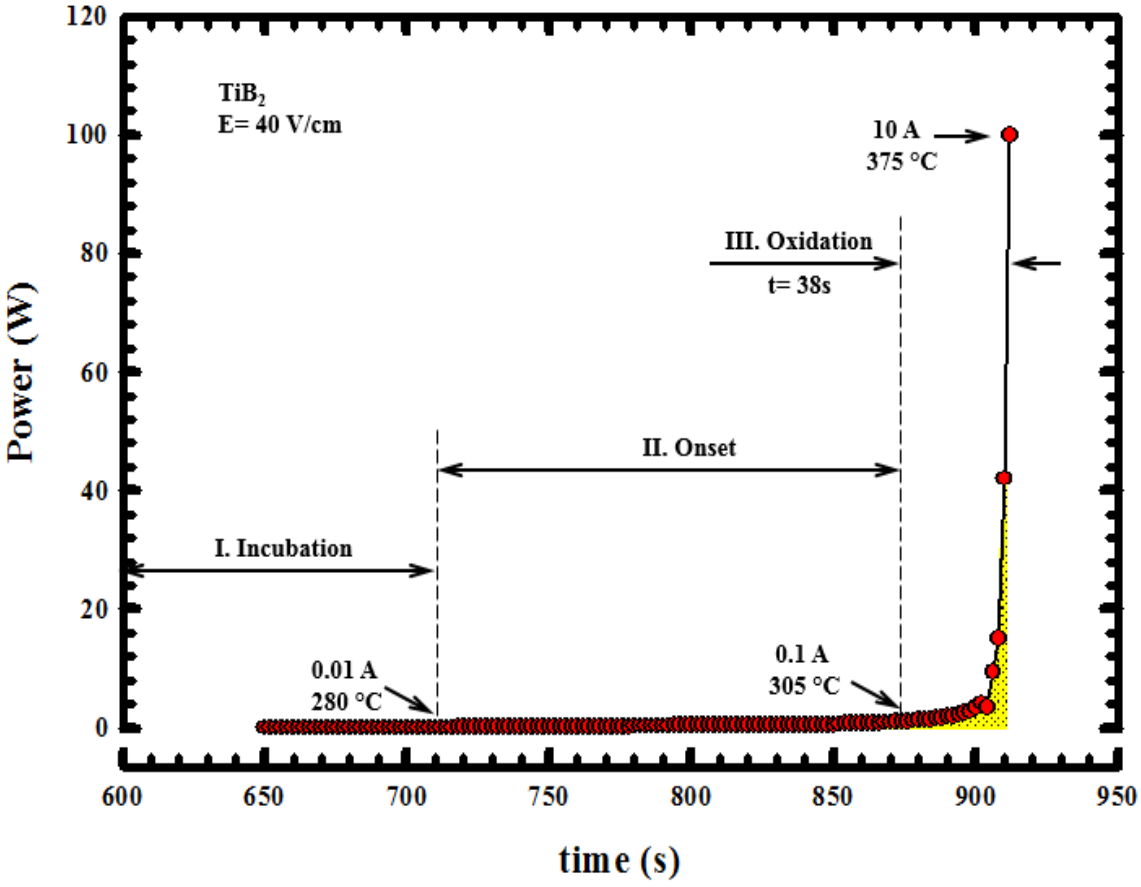

Figure 4. 25. Power (W) vs time (s) graph obtained under 40 V/cm electric field

4.1.2.4. Behavior of TiB_2 under Thermal Field and Isothermally Applied 45 V/cm Electric Field

A TiB_2 pellet was heated under zero electric field, unlike the other experiments, till 330 °C at which point a dc electric field of ~45 V/cm was imposed on it. The sample was then further heated to 640 °C under the same amplitude of electric field, and then it was left to cool to room temperature under zero field while data collection was continues with Δt= 3 seconds.

4.1.2.4.1. Effect of Isothermally Applied 45 V/cm Electric Field on TiB_2 at Unit Cell Scale

A dc electric field of 45 V/cm was isothermally applied on TiB_2, i.e. the specimen was heated up to 330 °C under zero electric field, and then the said electric field was imposed on it. Temperature was increased till 640 °C. The specimen became conductive as soon as it was subjected to the electric field, and a sudden jump in the current leakage from ~0.1 A to 10 A was observed at 360 °C. Lattice parameters, a and c, were found to be 3.0336 Å and 3.2419 Å at the point where the burst started, and they reached 3.0444 Å and 3.2532 Å in 55 seconds and 3.0495 Å and 3.2612 Å in 141 seconds, respectively, due to the current flow. Figure 4.26 shows the variation of the crystal parameters under the given experimental conditions.

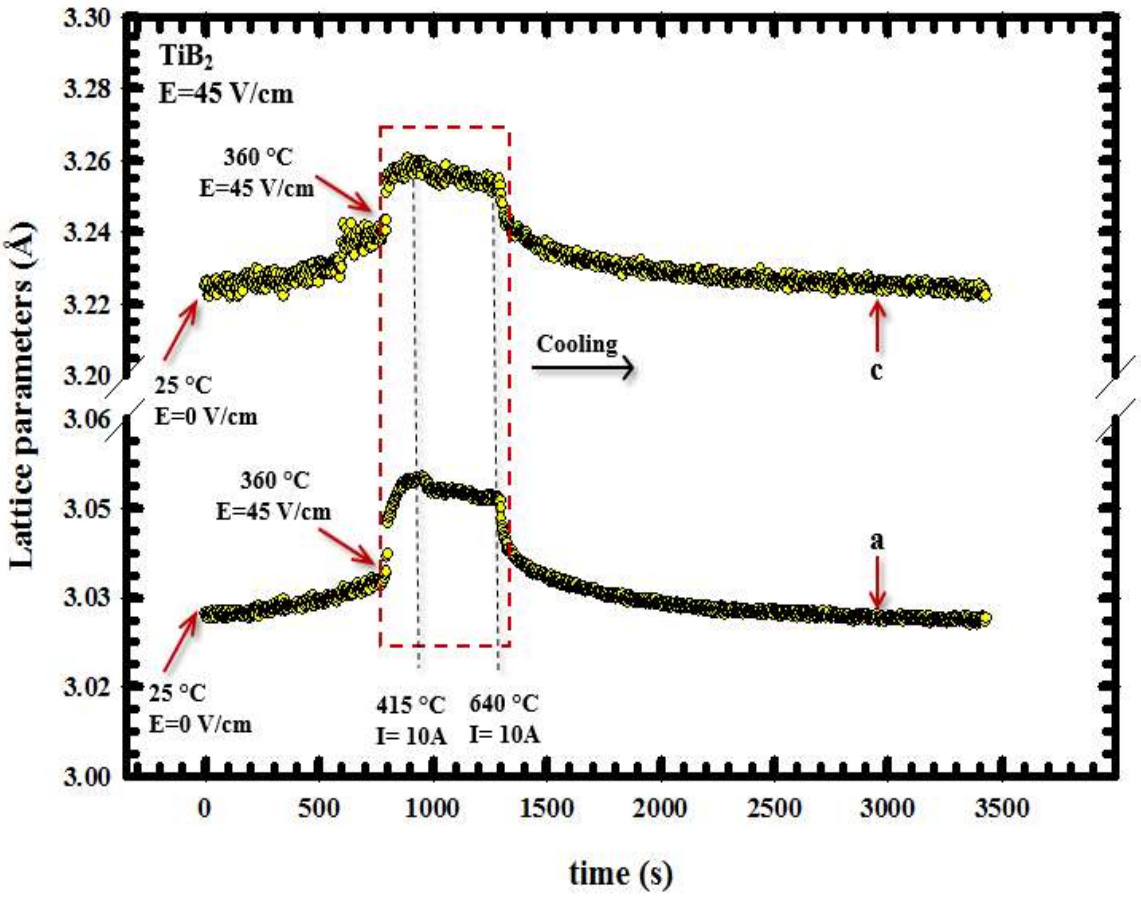

Figure 4. 26. Crystal parameters of TiB_2 under isothermally applied 45 V/cm dc electric field

Figure 4.27 shows the effects of isothermally applied 45 V/cm on the unit cell volume of the material in question. As shown in the figure, no electric field is applied till the temperature reaches 330 °C. 360 °C is the temperature at which the burst of charges take place. Also, new oxide peaks, which will be discussed under the oxidation section, become prominent enough at this temperature value, 360 °C, which fact enables one to measure the FWHMs and integrated intensities of each of them. Thermal expansion in the unit cell volume is 0.67% in 773 seconds from RT to 360 °C. Burst of the charges at 360 °C instigate the unit cell to expand by 1.75% in 141 seconds. The work done in ~55 seconds is 1.54 %. The rest of the work done to expand the unit cell volume by 1.75% might be

attributed to Joule heating in addition to the work done by electric field itself. The work done after the first seconds of the unit cell volume expansion (+1.54%) till the end of the total dilation of 1.75% might be non-adiabatic. Although the heating rate was intended to be kept constant, it increased from 360 °C to 415 °C during the burst due to the contribution of Joule heating. System was started being cooled at 640 °C under zero field.

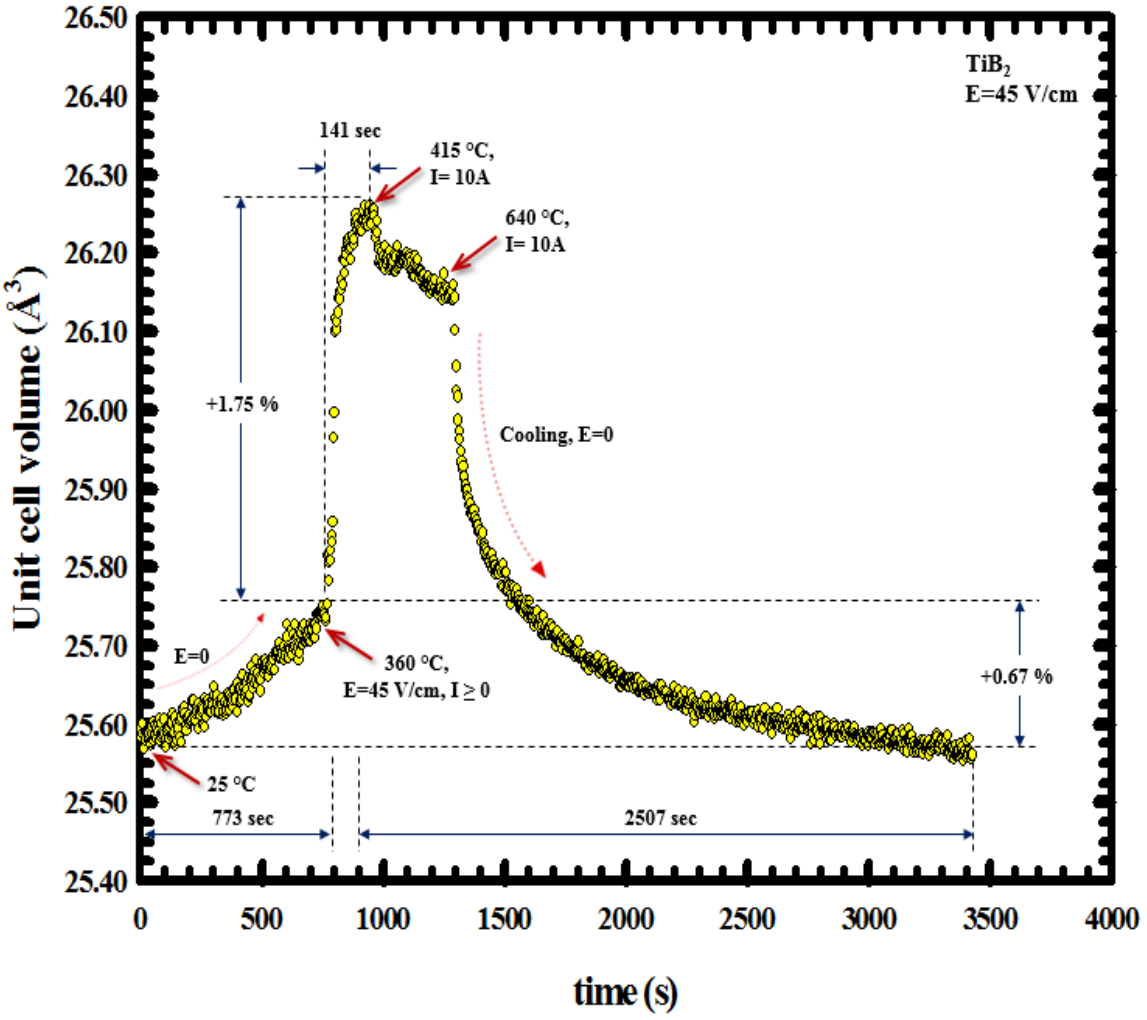

Figure 4. 27. The effect of an applied electric field of approximately 45 V/cm on the unit cell volume of TiB_2

Peaks presented in Figure 4.28 shifts upon applied electric field of 45 V/cm. $TiBO_3$ (104) peak appears on the spectrum with the application of 45 V/cm electric field as seen in the figure, and it moves toward left with the removal of electric and thermal fields. The peak width of TiB_2 (100) decreases with an increase in the current flow, but it increases again with its removal. The residual strain for TiB_2 (100) peak at RT at the end of the experiment was found to be $\varepsilon_{(100)}$= 0.021 %.

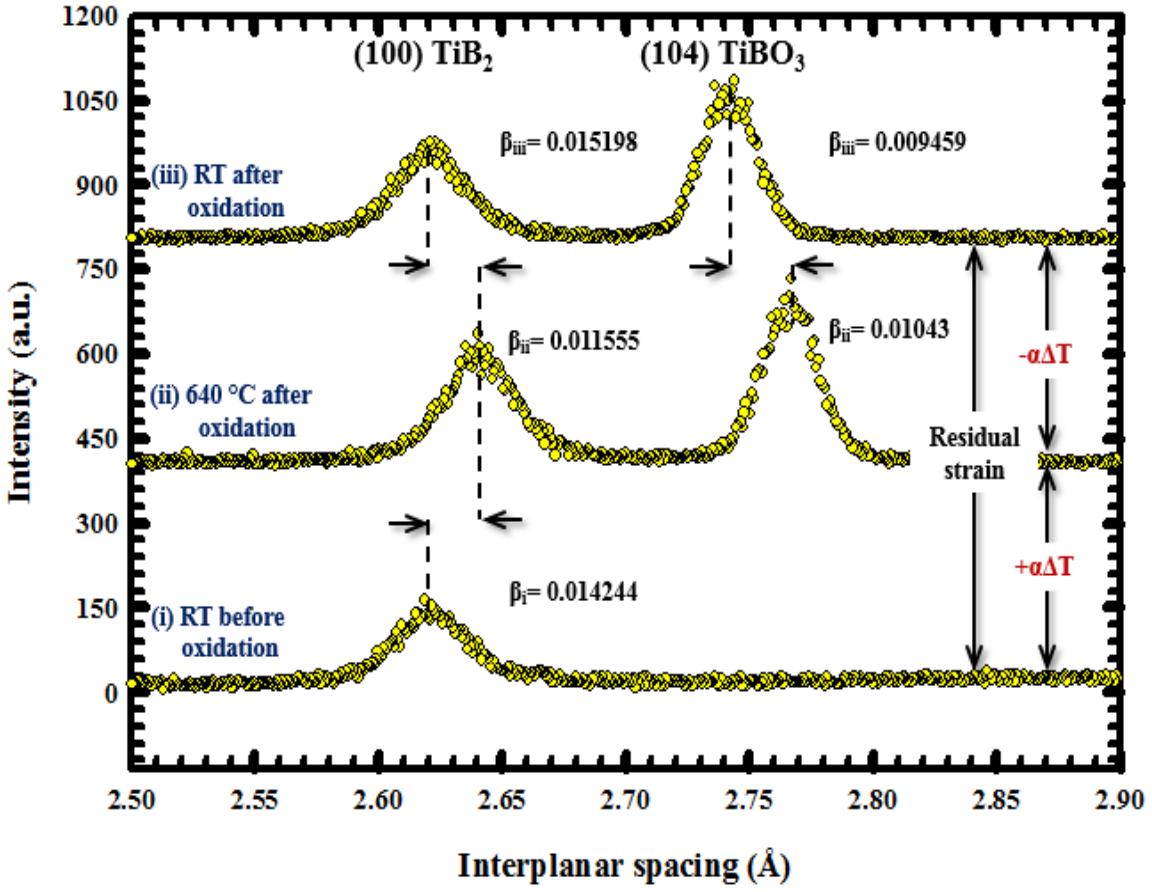

Figure 4. 28. Positions of the peaks TiB_2 (100) and $TiBO_3$ (104) at different circumstances under thermal and 45 V/cm electric fields: (i) at RT prior to experiment, (ii) at a high furnace temperature, 640 °C, (iii) at RT after the experiment. The residual strain for TiB_2 (100) peak at RT after the experiment is $\varepsilon_{(100)}$= 0.021 %

Figure 4.29 depicts the shifting in the position of TiB_2 (100) peak due to a sudden-rise in the current leakage under an isothermally applied 45 V/cm electric field. The said electric field is applied at 330 °C, and the current leakage exhibits an enormous increase at 360 °C.

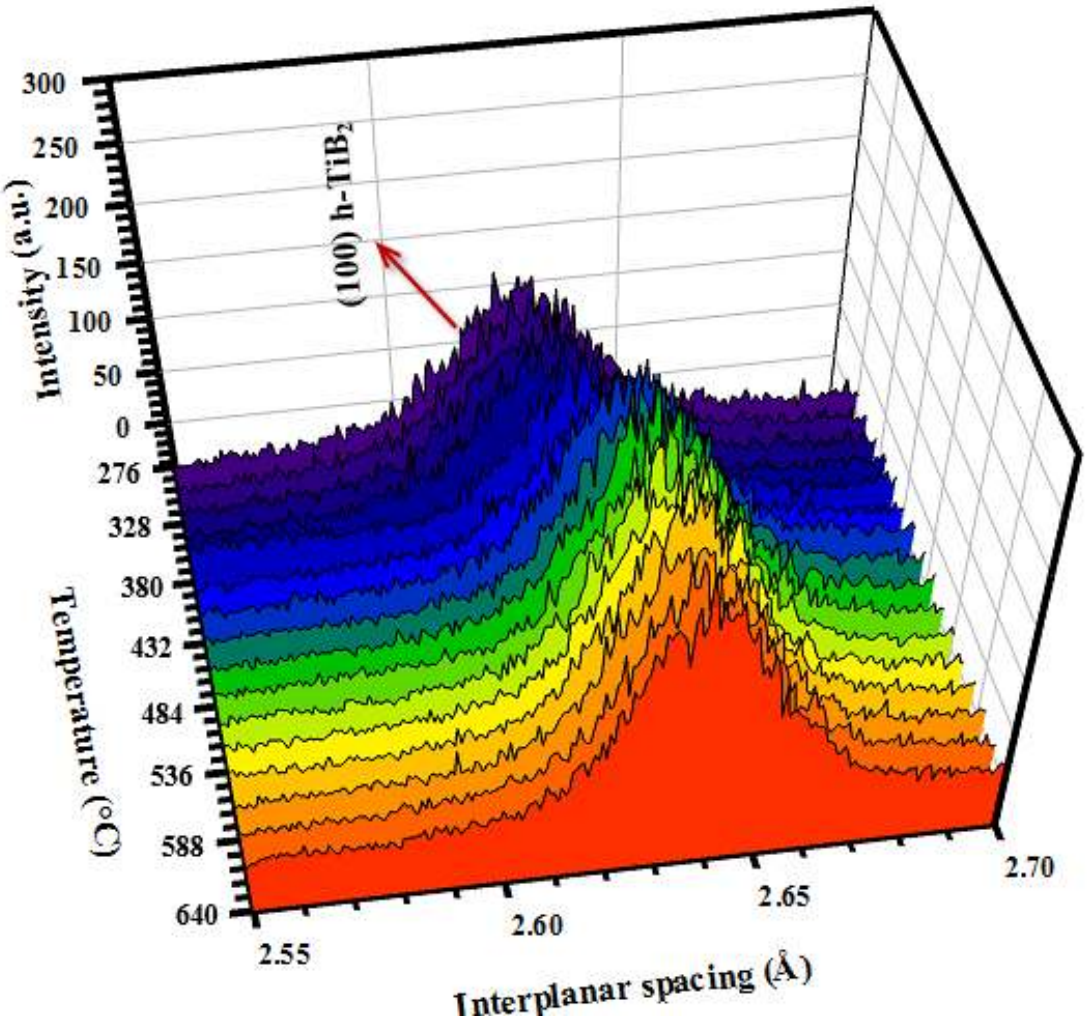

Figure 4. 29. Shifting in the position of TiB_2 (100) peak with a sudden-rise in the current flow under isothermally applied 45 V/cm electric field

4.1.2.4.2. Effect of 45 V/cm Electric Field on Oxidation and Phase Transformation between Existing Oxides in TiB_2

The behavior of TiB_2 under ~45 V/cm dc electric field and a thermal field is as in Figure 4.30. As soon as a dc electric field of ~45 V/cm is applied on the sample, $TiBO_3$ (104) and $TiBO_3$ (012), in addition to an unknown peak, form in 20 seconds. The unknown peak disappears in the following 15 seconds. Intensities of $TiBO_3$ (104) and $TiBO_3$ (012) anomalously increase in less than a minute. Additionally, $TiBO_3$ (110) forms in 50 seconds right after the electric field is applied. Its intensity increases enormously up to 960 a.u. followed by a decrease to 25 a.u. in less than 40 seconds. Sharp changes in the intensity of this peak in a very short time span can be attributed to the preferred orientation in the specimen. TiO_2 (101) peak disappears in the following 3 minutes after the electric field is applied that it probably contributes to the new oxide phases. Low intensity $TiBO_3$ (116) and $TiBO_3$ (202) peaks which appear in a minute under the electric field can also be seen in Figure 4.30.

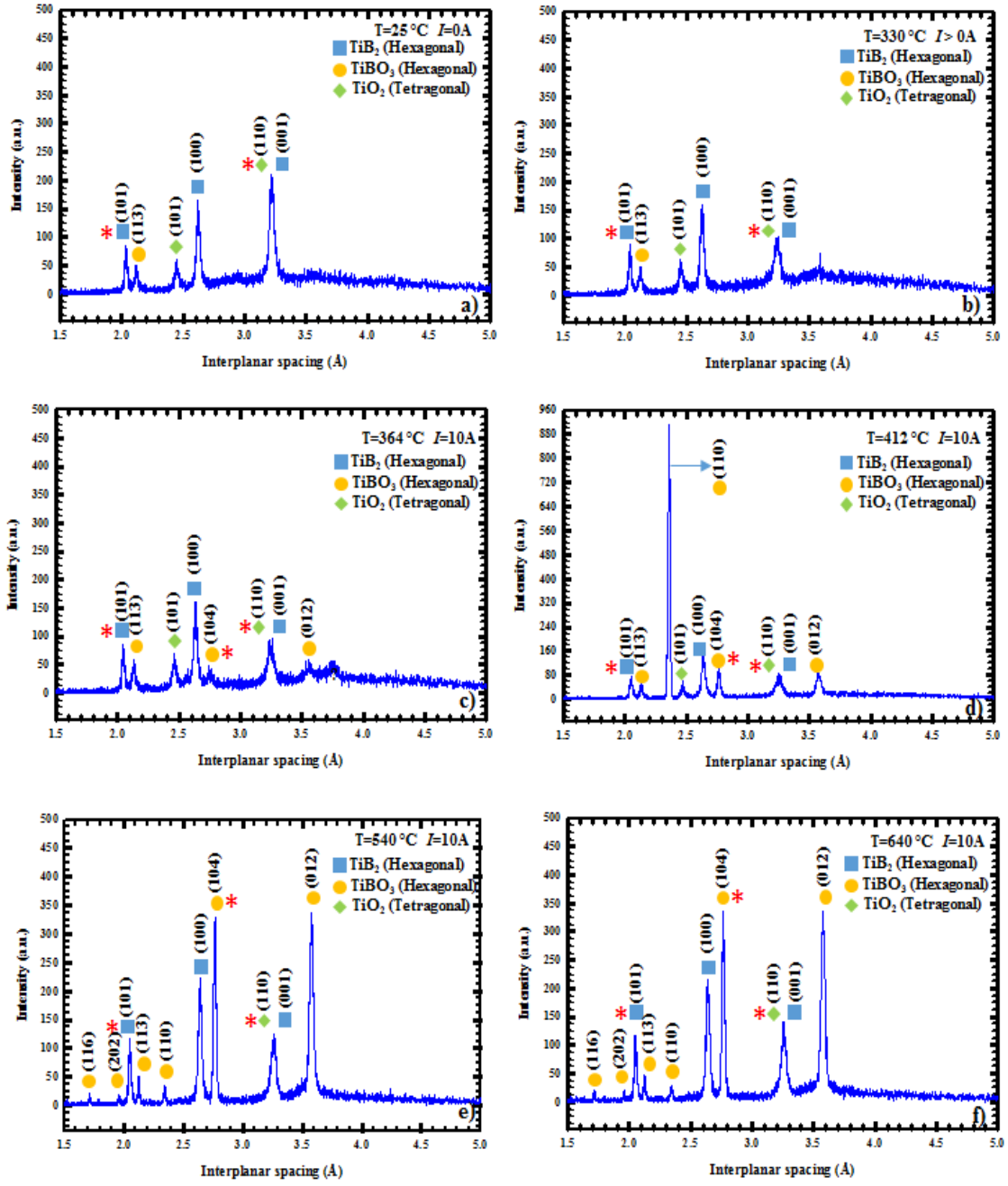

Figure 4. 30. Synchrotron energy dispersive x-ray diffraction spectra of a TiB_2 sample under applied thermal and electric fields. A dc electric field of ~45 V/cm is applied at 330 °C (* on the spectra represents 100 % peaks)

Figure 4.31 shows the insets of the spectra of TiB_2 obtained at RT prior to the experiment and at 640 °C under the influence of ~45 V/cm electric field. The hump existing

at RT disappears with the application of the electric field and yields new oxide phases as the same was observed under non-isothermally applied 40 V/cm.

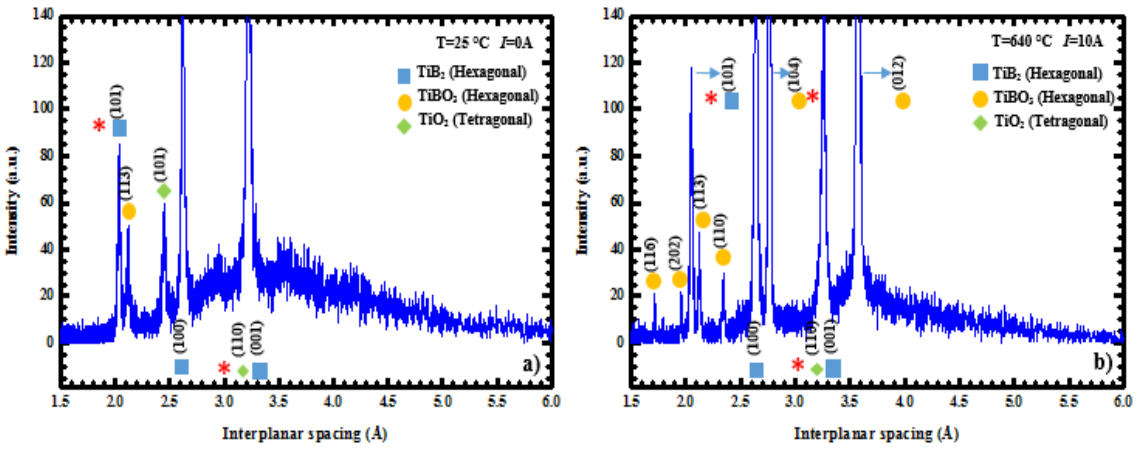

Figure 4. 31. Insets of the spectra of TiB_2 at **a)** RT and **b)** 640 °C. The hump existing at RT disappears with the application of ~45 V/cm dc electric field (* on the spectra represents 100 % peaks)

Evolution of the new phases under applied electric field between 330 °C and 420 °C is demonstrated in Figure 4.32. Effect of the applied electric field of ~45 V/cm at 330 °C on the development of new oxides can be clearly seen in this figure.

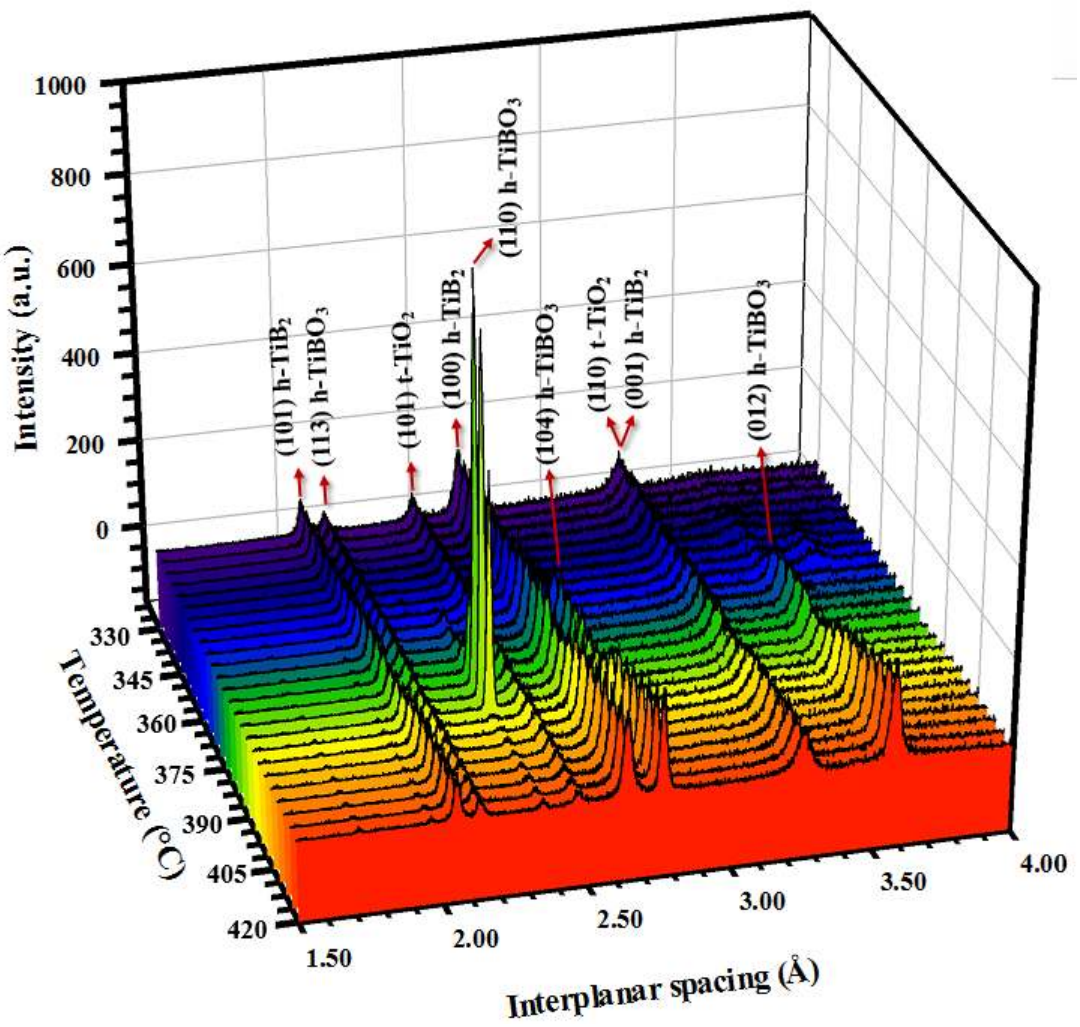

Figure 4. 32. Evolution of new oxide phases in a TiB_2 specimen subjected to ~45 V/cm dc electric field in 330 °C – 420 °C temperature range (h: hexagonal, t: tetragonal)

Figure 4.33 exhibits the quantitative analysis results of the oxidation and phase transformation processes in the specimen on which ~45 V/cm dc electric field was imposed at 330 °C. Only thermal field was applied on the sample till the said temperature, and no drastic change was observed in the composition of the phases. As mentioned earlier, new peaks became prominent enough at 360 °C, and their intensities increased enormously in a very short time. Sudden rise in the current flow triggered the composition of $TiBO_3$ to increase from 21.80% to 49.45% in less than 100 seconds. The composition of $TiBO_3$ kept

increasing slowly up to 52%, and it was found to be 51.41% at the end of the experiment. TiO_2 had a composition of 28.20% at 360 °C; however, it dissolved and disappeared in the same time span due to the burst. TiB_2 showed a small increase in its composition from 48.61 to 54.08 % in ~30 seconds and then exhibited a decrease to 47.60% in the following ~70 seconds. Finally, it was found to be 48.27% at the end of the experiment.

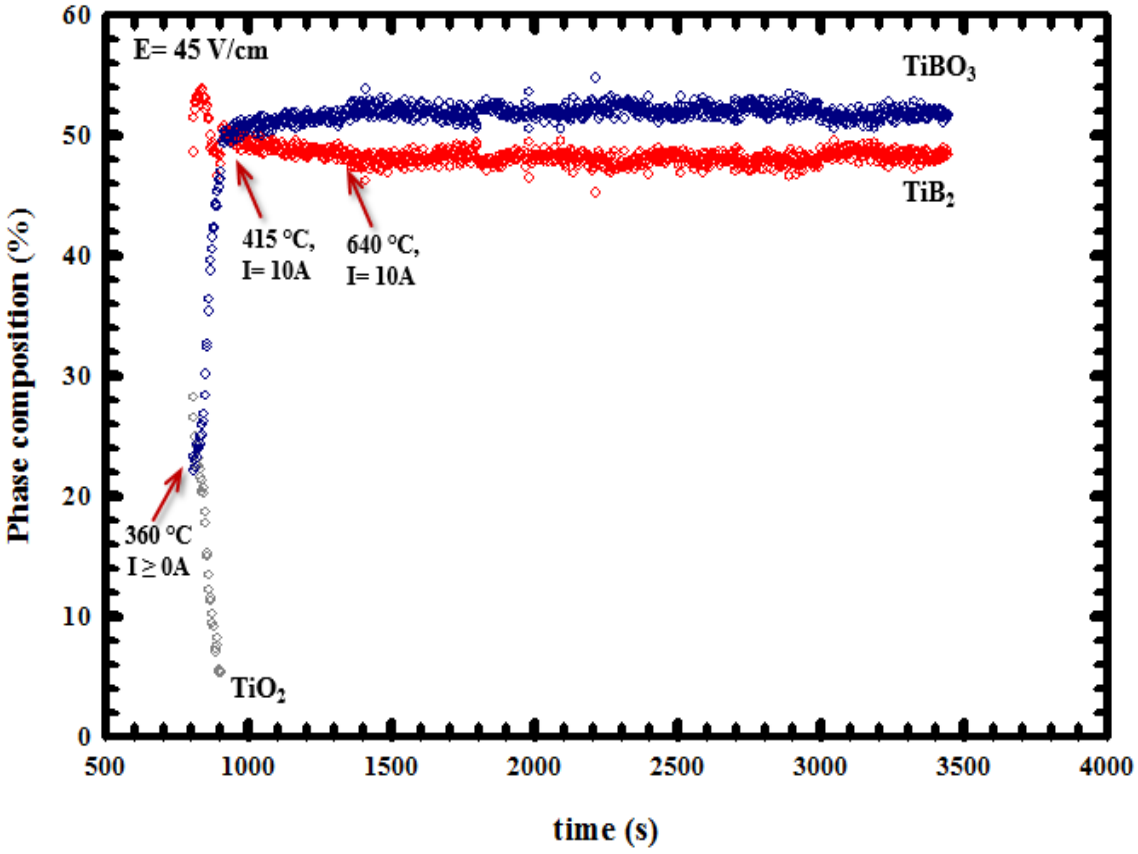

Figure 4. 33. Effect of 45 V/cm electric field on the oxidation and phase transformation processes between the existing oxides in TiB_2

4.1.2.4.3. Thermodynamic Approach to the Burst Event in TiB_2 under 45 V/cm Electric Field

Figure 4.34 illustrates the changes in the power (W), current (A), and voltage (V) values depending on the changes in the conductivity of the specimen exposed to 45 V/cm electric field. The said electric field is applied at 330 °C, and the specimen immediately lets the current flow through itself as seen in the figure. The current leakage is 0.01 A at 330 °C, and it reaches 0.1 A with an increase in the temperature to 360 °C at which point the burst event takes place. The current leakage and temperature reach 10 A and 415 °C in 52 seconds, respectively. The power imposed on the system changes from 0.52 W to 120 W as a response to the change in the conductivity of the material. The most of the oxidation work is done during the burst of which integration yields 732.6 J. Calculation on the theoretical temperature limit due to the Joule heating leads to 1577 °C.

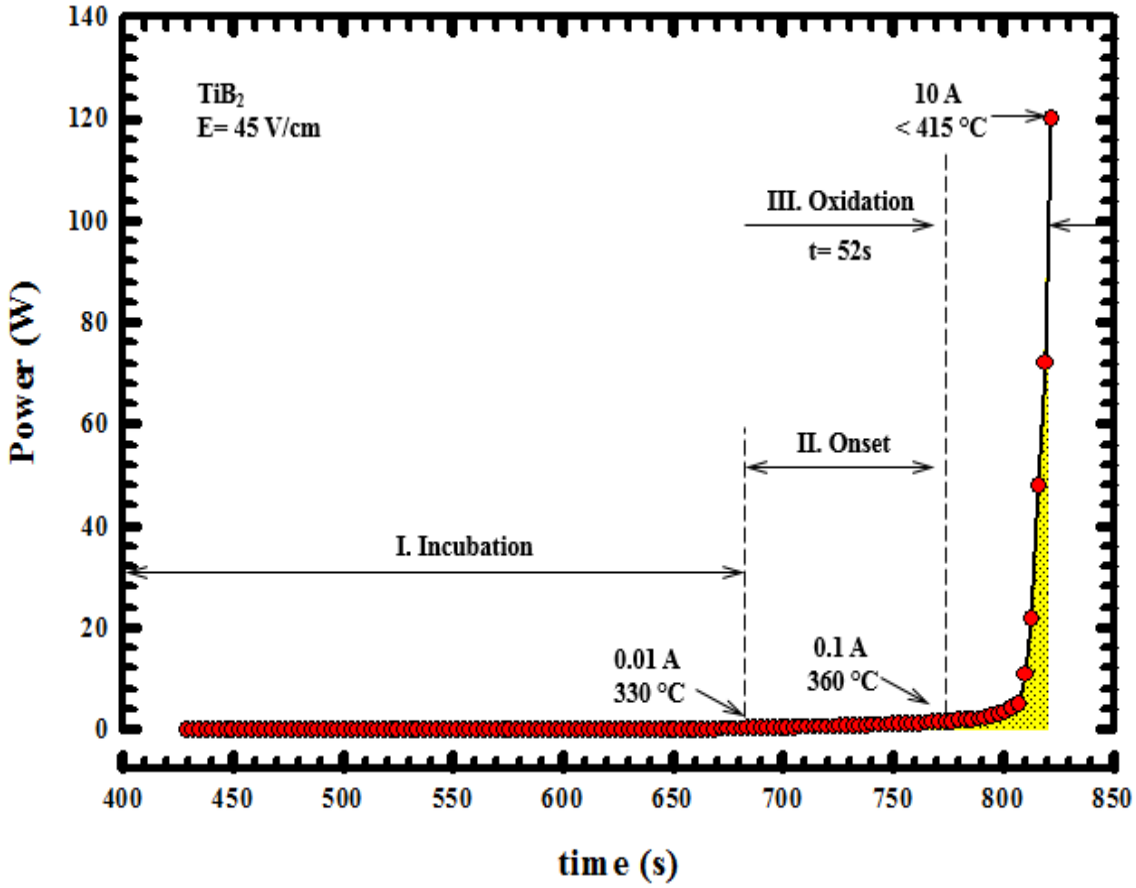

Figure 4. 34. Power (W) vs time (s) graph obtained under isothermally applied 45 V/cm electric field

4.1.2.5. A Tentative Model for the Oxidation of TiB_2 under Electric Field

Since TiB_2 powder which we used in our experiments had already contained a serious amount of oxide phase (≥20 %) at RT, electric field mostly caused a phase transformation between them. The hump observed at RT and discussed in detail in the above subsections disappeared with the application of high magnitude of electric fields though same was not true for low electric fields such as 16 V/cm. In an effort to identify the composition of this hump, we matched it with amorphous B_2O_3 because this oxide is almost always found in amorphous phase in nature. Given the fact that the powder we used

contain TiO_2, $TiBO_3$, and B_2O_3 (as an amorphous form) in addition to host TiB_2 particles, possible reactions which the applied electric field triggers are as follows;

$$4TiO_2 + 2B_2O_3 \rightarrow 4TiBO_3 + O_2$$

$$4TiB_2 + 9O_2 \rightarrow 4TiBO_3 + 2B_2O_3$$

Second reaction might be taking place under lower electric field more compared to higher electric fields because the quantitative analysis of phase composition in the samples reveal that TiB_2 is more involved in lower field experiment (Figure 4.15). A tentative model exhibiting the oxidation of a TiB_2 particle is seen in Figure 4.35. This model suggests the following steps;

(i) Diffusion of O_2 in ambient atmosphere

(ii) Dissolution of O_2 at interface (1)

(iii) Diffusion of O_2 in oxygen layer

(iv) Chemical reaction of O_2 with TiB_2 passing interface (2)

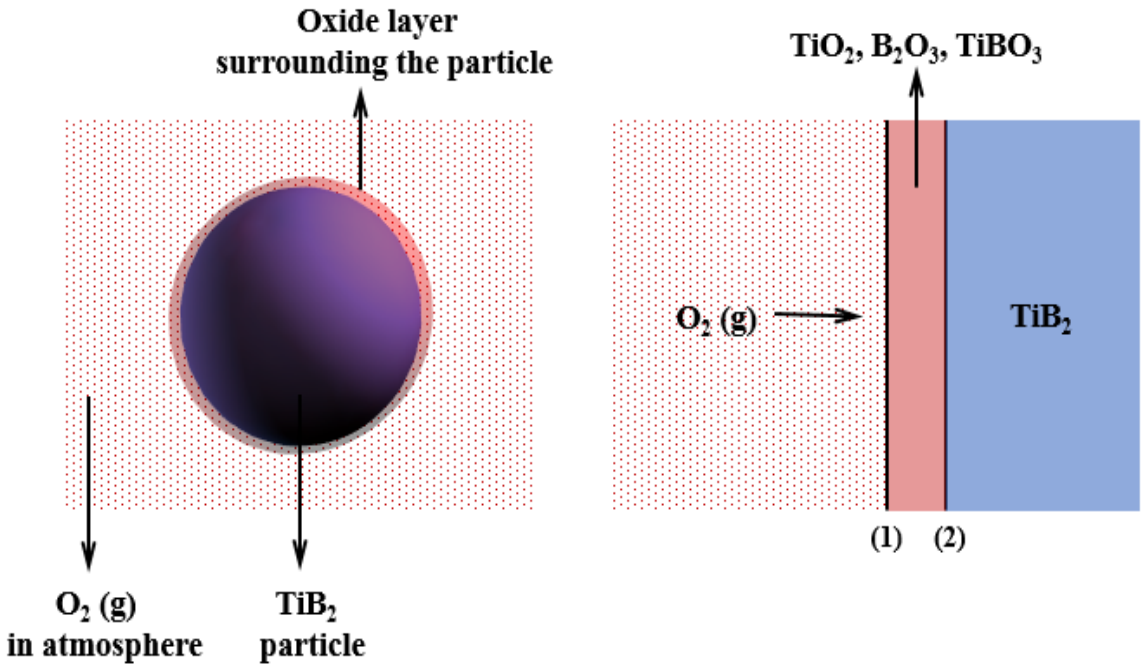

Figure 4. 35. A tentative model on the oxidation of TiB_2 under an applied electric field which suggests (i) diffusion of O_2 in ambient atmosphere, (ii) dissolution of O_2 at interface (1), (iii) diffusion of O_2 in oxygen layer, (iv) chemical reaction of O_2 with TiB_2 passing interface (2)

4.2. Barium Titanate Study

4.2.1. Preamble

In this part of the study, results showing the variation of crystal parameters, structural phase transformation, and densification of $BaTiO_3$ upon an applied electric field are revealed. A baseline acquired under the application of a thermal field is used for a further understanding of the effects of the electric field on this material. Also, the required temperature values to acquire the same work done by electric field when no electric but a thermal field is applied on this material is calculated. Due to the time limitation at Brookhaven National Laboratory, some experiments were conducted at Nanomaterials Lab at Rutgers University. Specimens were also characterized using SEM and powder x-ray diffraction.

Two commercial cubic $BaTiO_3$ powders purchased from two different companies (US Research Nanomaterials Inc. and Sigma Aldrich Co. LLC.) were used for this part of the study. Figure 4.36 illustrates the SEM images of the powders. Particle size of both powders are ≤100 nm as reported by the provider companies.[13, 14]

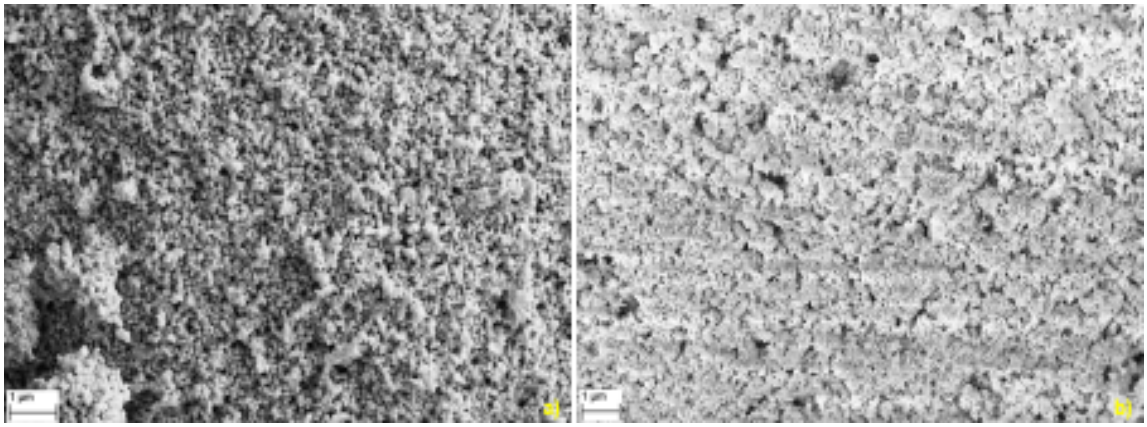

Figure 4. 36. SEM images of cubic $BaTiO_3$ powders purchased from **a)** US Research Nanomaterials Inc.[13] and **b)** Sigma Aldrich Co. LLC.[14]

Powder x-ray diffraction patterns of both cubic powders are presented in Figure 4.37.

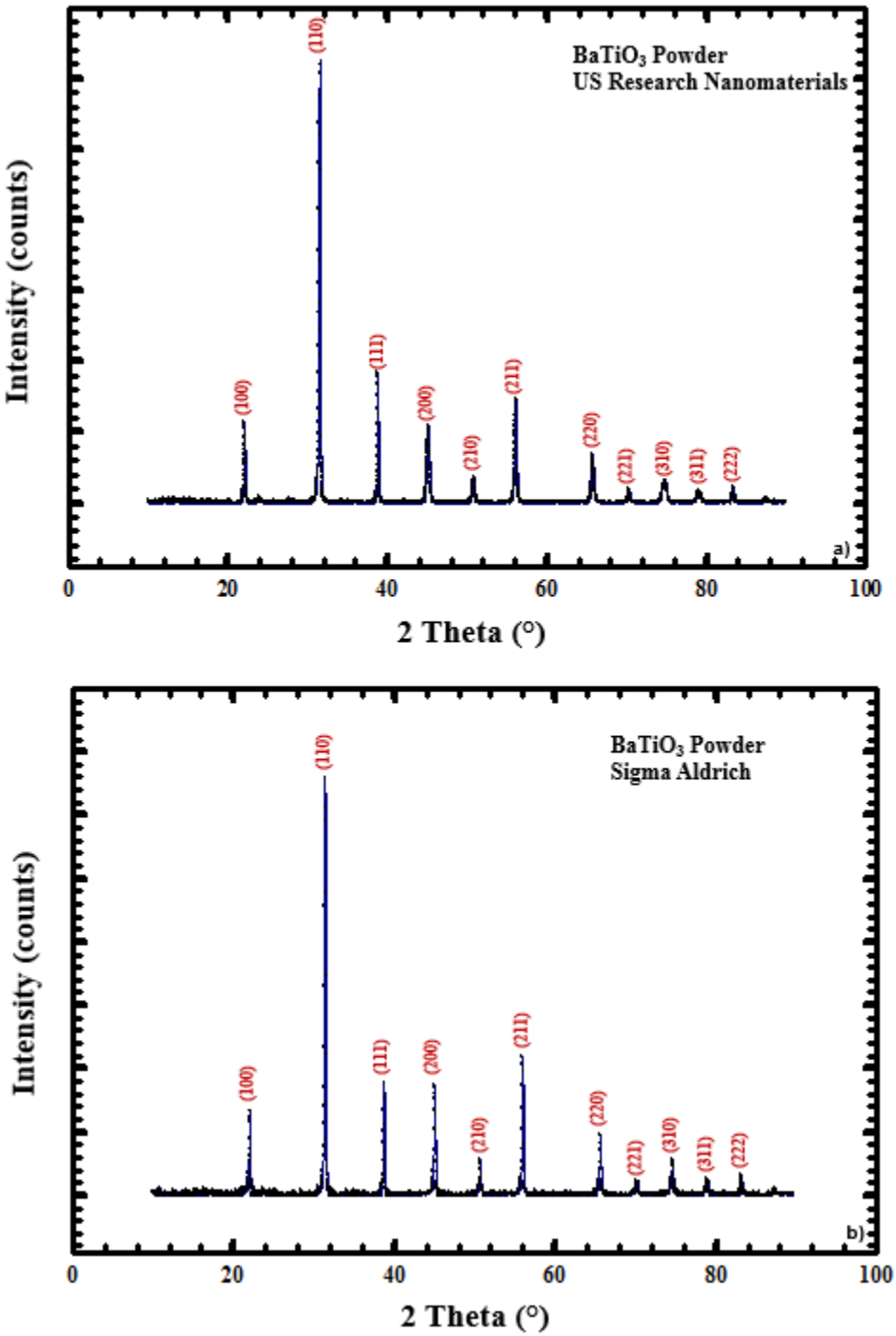

Figure 4. 37. Powder x-ray diffraction spectra of cubic $BaTiO_3$ powders purchased from **a)** US Research Nanomaterials Inc.[13] and **b)** Sigma Aldrich Co. LLC.[14]

4.2.2. Behavior of $BaTiO_3$ under Thermal Field

Figure 4.38 demonstrates the changes in the crystal parameter, a, of cubic $BaTiO_3$[13] under thermal field. Temperature was increased from RT to 700 °C, and the response of the specimen to heating was monitored with 3 seconds frequency using EDXRD.

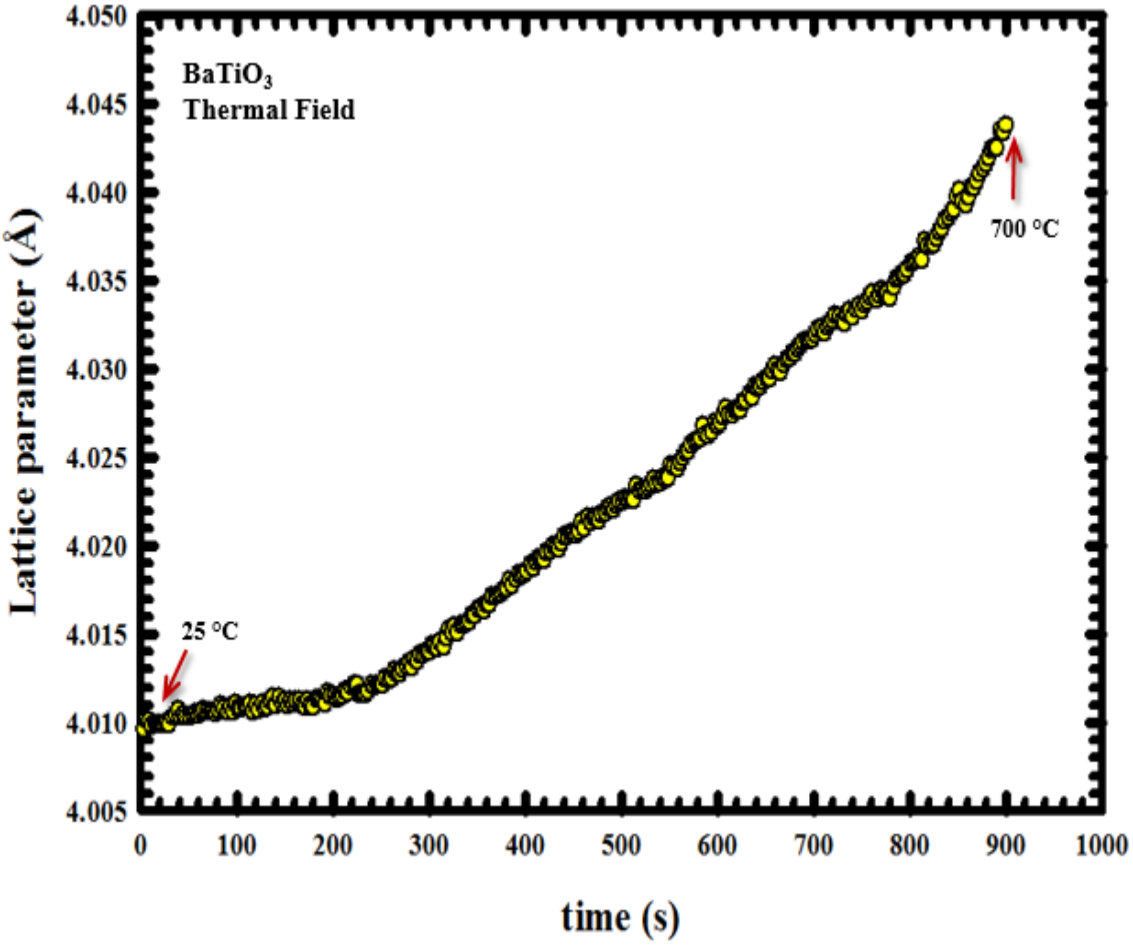

Figure 4. 38. Variation of crystal parameter, a, of cubic $BaTiO_3$[13] under thermal field

Figure 4.39 exhibits the changes in the unit cell volume of $BaTiO_3$ calculated using the data presented in Figure 4.38. Unit cell of the specimen subjected to a thermal field expands obeying a stable quadratic behavior. It exhibits no change or ambiguity in the way

it expands upon thermal field. In other words, no kink on the plot is observed as opposed to its behavior under an applied electric field as discussed in detail below.

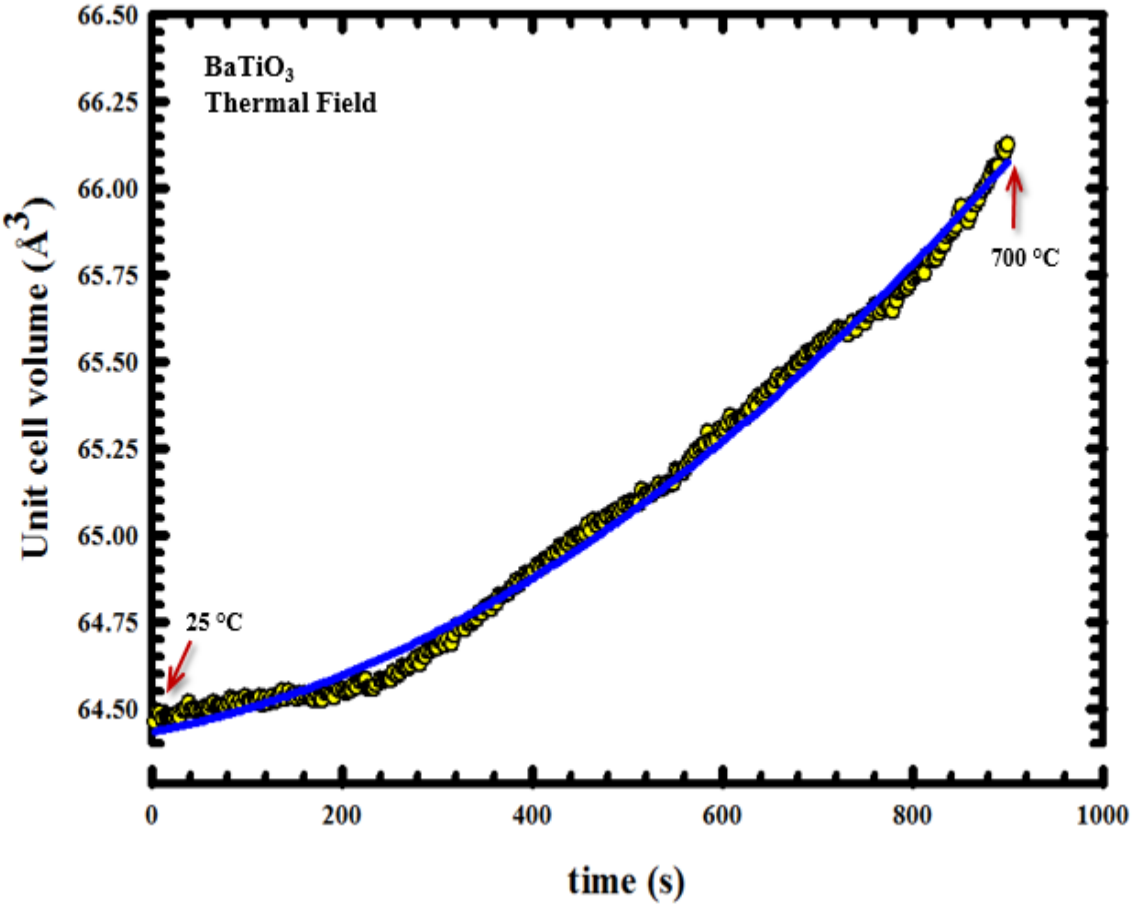

Figure 4. 39. Unit cell volume expansion of $BaTiO_3$[13] under the application of thermal field

4.2.3. Structural Phase Transformation of $BaTiO_3$ upon Applied Electric Field

Figure 4.40 shows the topographic view of all spectra collected using EDXRD during the flash sintering process of $BaTiO_3$ under270 V/cm[13]. Sintering of the material in question was achieved at ~390 °C as the lowest sintering temperature. An electric field of

270 V/cm was applied on the specimen, and the burst, i.e. sudden rise in the current leakage, was observed at 390 °C at which point the unit cell volume exhibited an anomalous expansion. Consolidation of the material took only 24 seconds. The material was in a cubic structure as discussed in the part in which the characterization results of the powder were covered. However, the sudden rise in the current flow caused an instant increase in the power absorbed by the specimen which in turn caused a structural phase transformation in the material from cubic to tetragonal phase. As seen in the figure, cubic $BaTiO_3$ peaks (200), (210), (211), (220), (221), (310), and (311) showed splitting and became (200 : 002), (210 : 201 : 102), (211 : 112), (220 : 202), (221 : 212), (310 : 301 : 103), and (311 : 113), respectively. Furthermore, a small peak of low intensity, (110 : 101), was observed with the flow of current through the specimen.

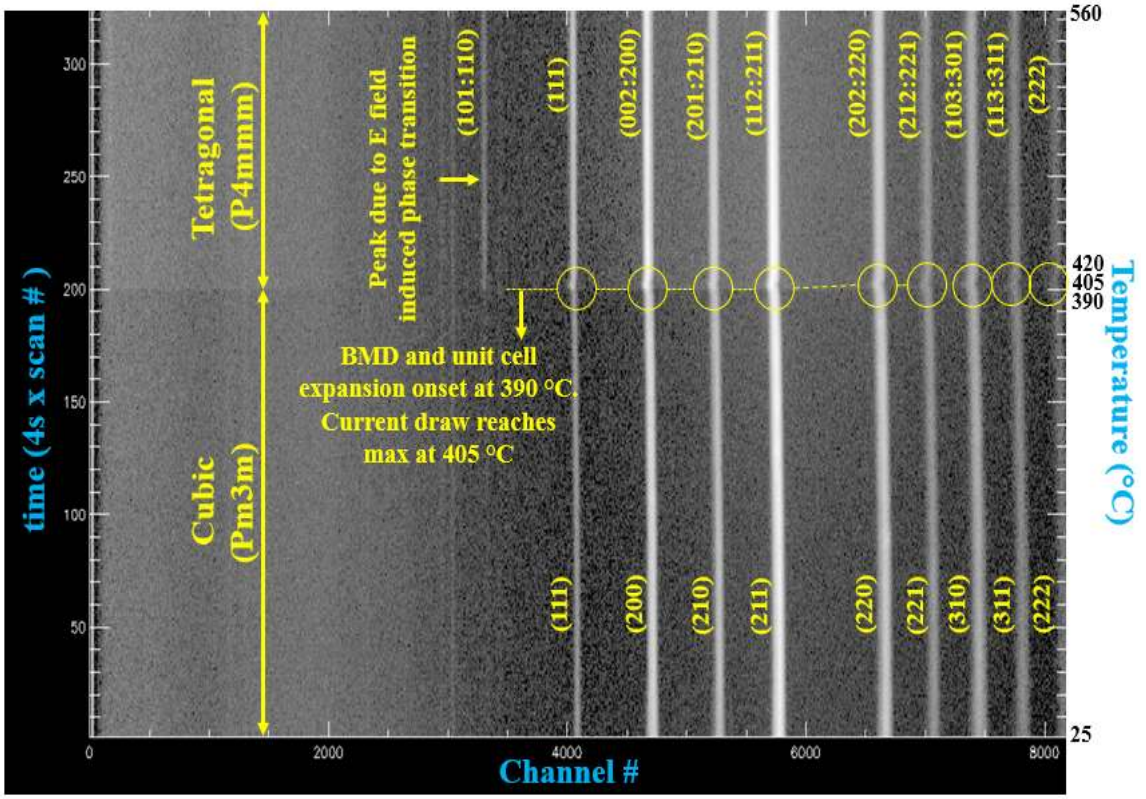

Figure 4. 40. Topographic view of all spectra collected during the densification of nano-$BaTiO_3$ under 270 V/cm electric field and ~1 A current cut-off

Figure 4.41 shows the variation in the crystal parameters of $BaTiO_3$ under thermal and 270 V/cm dc electric fields. The said electric field was applied from the beginning of the experiment till the temperature reached 405 °C which was the end of the burst. The specimen was only subjected to thermal field from 405 °C to 560 °C temperature value after which the system was started being cooled down. Although the system expands in a slow and stable condition till and after the burst, sudden increase in the current flow instigates an anomalous expansion in the crystal parameters. Although the starting $BaTiO_3$ was in cubic structure, the burst of charges led the specimen to a tetragonal phase. Therefore, the figure shows the only lattice parameter, a, of cubic structure till ~400 °C, and both crystal parameters, a and c, of tetragonal structure after this temperature value.

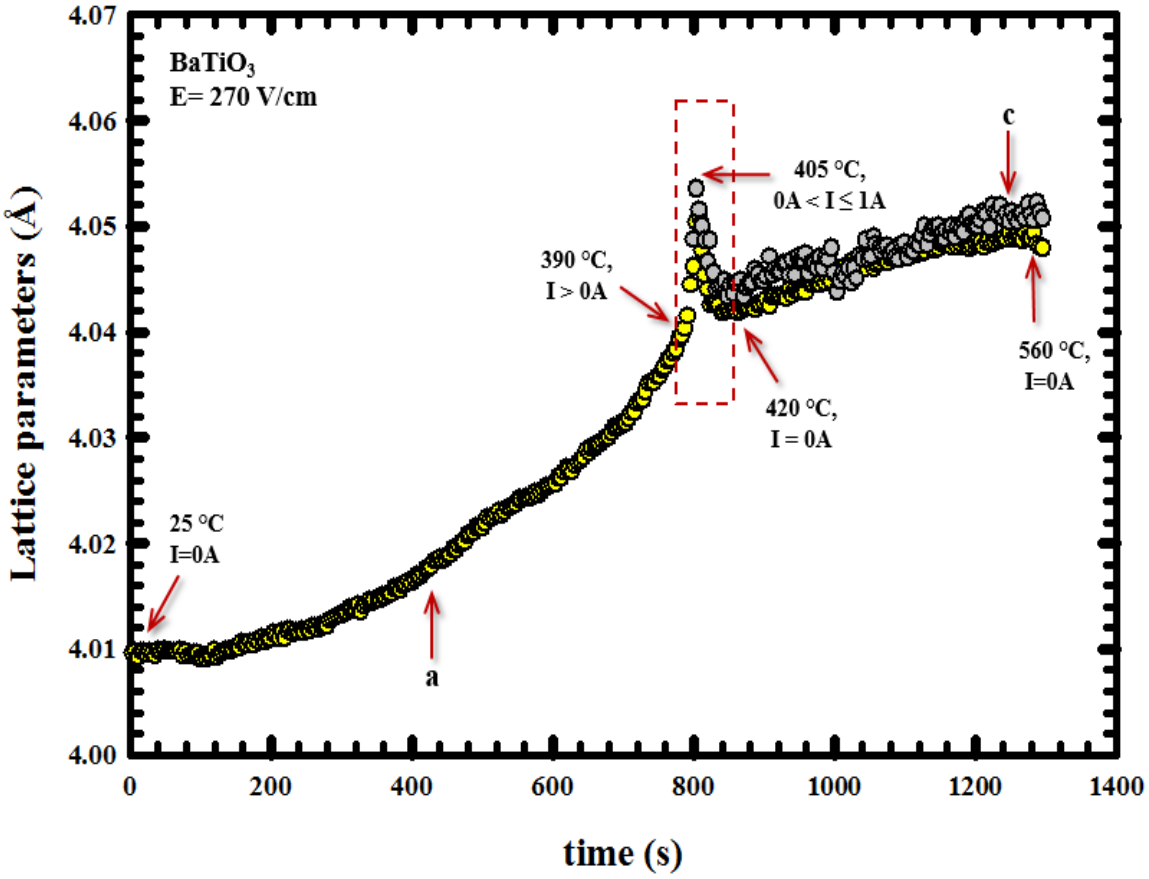

Figure 4. 41. Variation of crystal parameters of $BaTiO_3$ under thermal and electric fields

Figure 4.42 depicts the unit cell volume of $BaTiO_3$ upon the electric and thermal fields. Before the burst takes place, the unit cell volume expansion follows a quadratic behavior. On the other hand, sudden rise in the current leakage causes a structural phase transformation from cubic to tetragonal phase whereby the unit cell volume exhibits a linear dilation as seen in the figure. This plot presents a similar behavior with the coefficient of thermal expansion behavior of $BaTiO_3$ in cubic and tetragonal structure reported by He.[138] The unit cell volume expands by 2.26% in 784 seconds from RT to 390 °C at which temperature the burst occurred. Most of the densification work was done in 24 seconds during the burst, and the increase in the current leakage caused an anomalous dilation in

the unit cell volume by 0.88%. Though Joule heating has some effect on the system, it is unlikely for it to be the sole or the major cause of the abnormal unit cell volume expansion and density increase in the specimen. Temperature changed from 390 °C to 405 °C during the burst. Current leakage reached its maximum of ~1 A at the later temperature value and then dropped down to zero because the electrode broke. Temperature reached 420 °C after the burst, and the system was heated up to 560 °C under zero electric field.

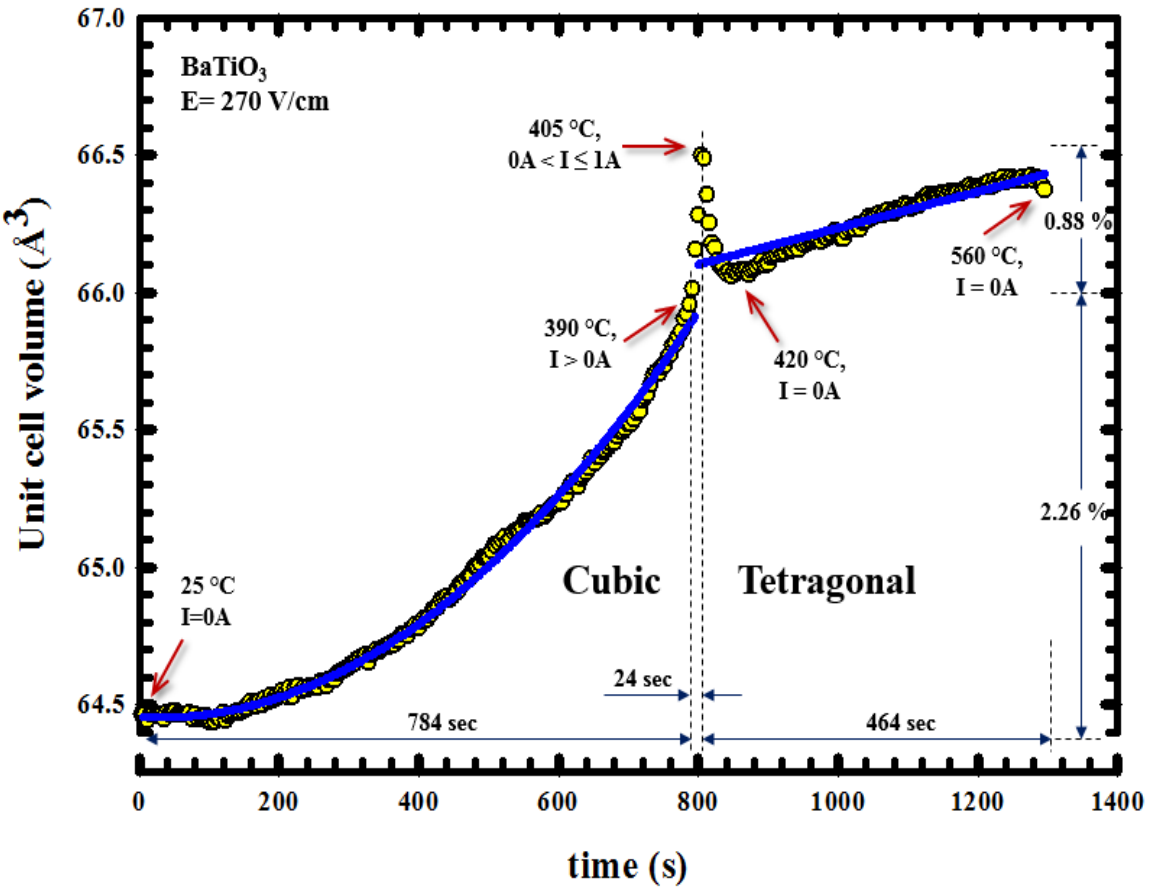

Figure 4. 42. Unit cell volume expansion and structural phase transformation in nano-$BaTiO_3$ upon thermal and electric fields

Figure 4.43 illustrates shifting in the position of (211) $BaTiO_3$ peak under the current flow. Lower data represents the peak position in question at RT at the beginning of

the experiment whereas the upper one shows that of the same peak at around 405 °C at which the current leakage reached its maximum. As seen in the figure, the applied electric field, and hence, the sudden rise in the current leakage, triggers an expansion in the material at the unit cell scale as a result of which the peak being examined shifts in the right direction. The peak width is β_i= 0.009497 at RT, however, it is β_{ii}= 0.009038 at the later temperature.

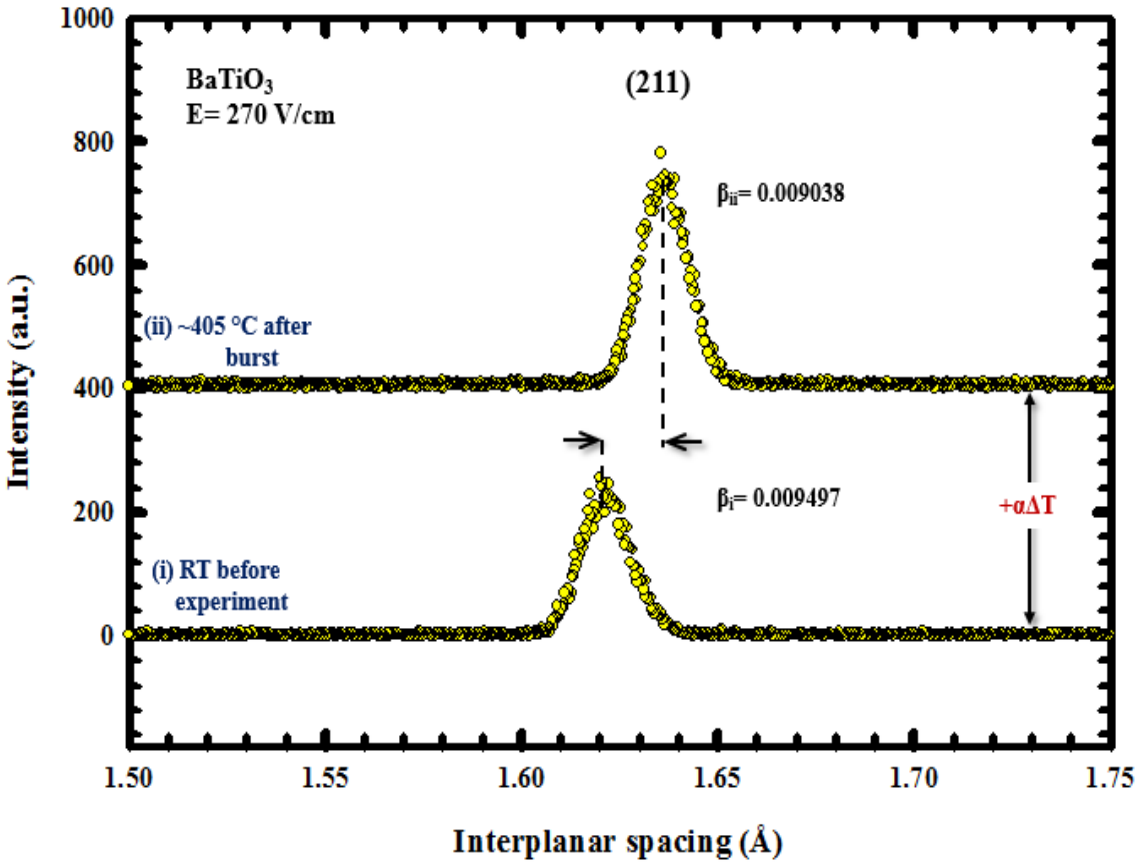

Figure 4. 43. Shifting in the position of $BaTiO_3$ (211) peak upon the burst of the charges in a temperature range of 390 – 405 °C

Figure 4.44 shows the effects of the current flow on the position of (211) peak in detail. 14 different spectra acquired at different temperatures are presented in this figure, so that the shifting in the peak position upon the current leakage can clearly be seen.

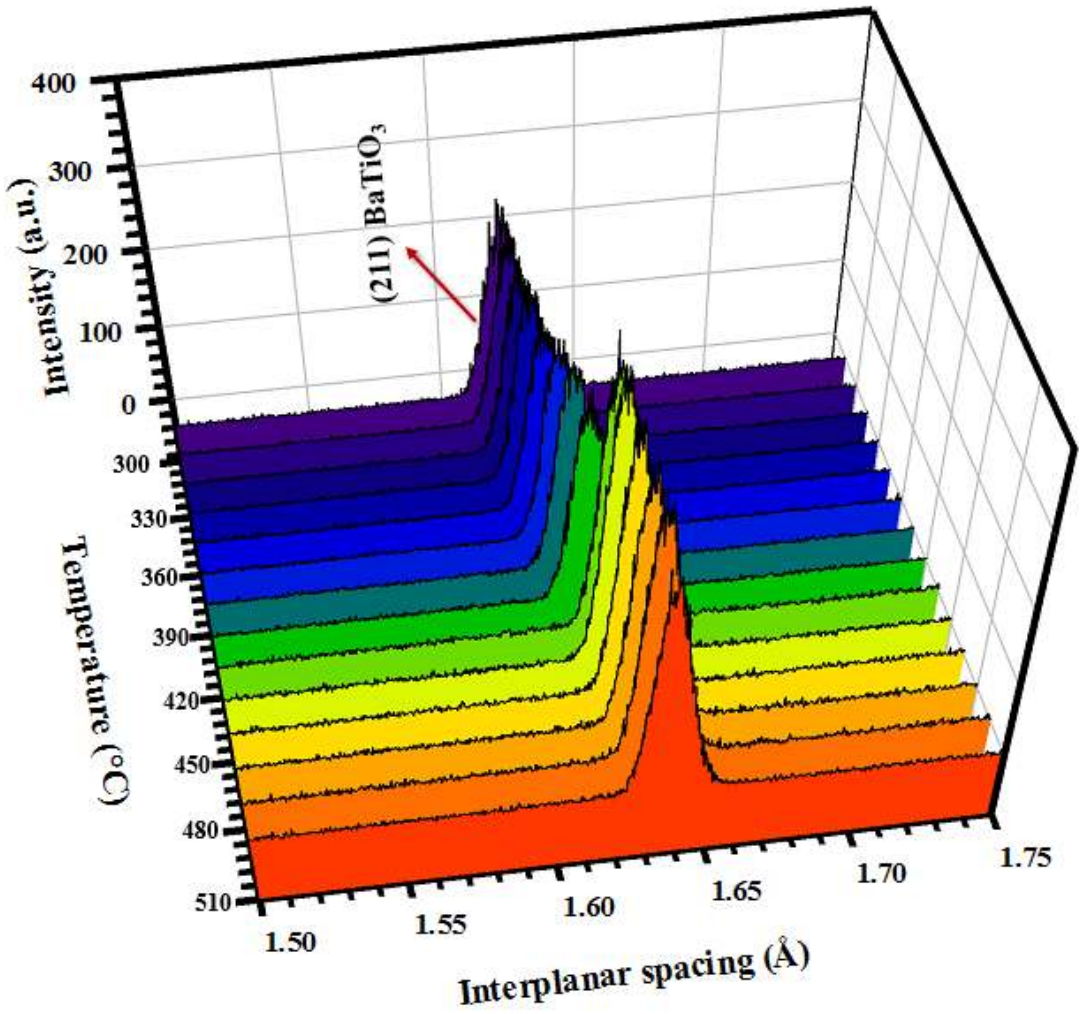

Figure 4. 44. Effect of the applied electric field of 270 V/cm on the position of (211) peak

Energy dispersive x-ray spectra of $BaTiO_3$ obtained at different temperature and current values are shown in Figure 4.45. The material became conductive at 390 °C that

the existence of silver paste on both surfaces of the sample facilitated the sintering process, and the current leakage reached its maximum of ~ 1 A. The figure shows that instantaneous increase in the current leakage leads to an increase in the intensities of the peaks. This fact is an indicative of density increase in the sample being sintered. The material goes under a structural phase transformation from cubic to tetragonal with the burst of charges; however, splitting on the peaks, which is a characteristic feature of tetragonal $BaTiO_3$, is not observed on the EDXRD patterns due to resolution issues. Powder x-ray diffraction results, which are discussed later in detail, confirm the phase transformation.

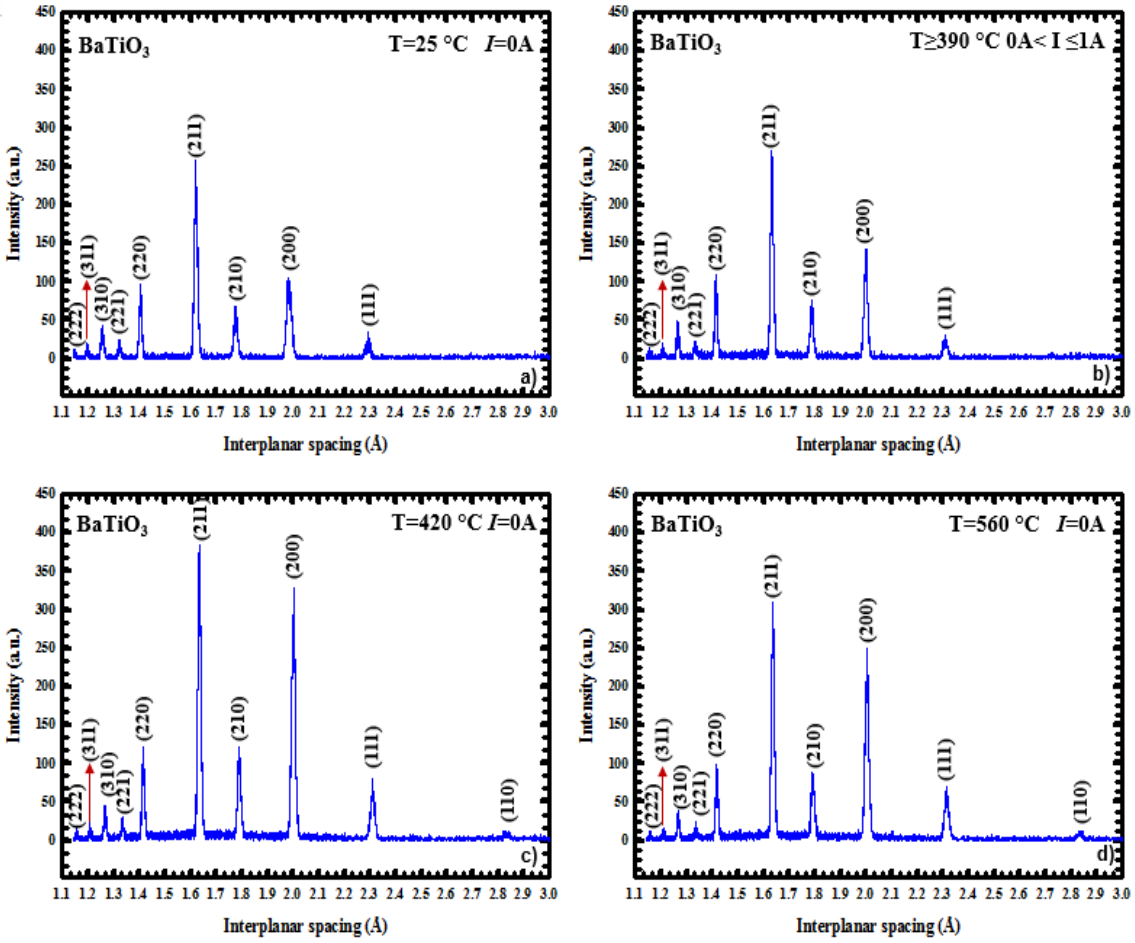

Figure 4. 45. $BaTiO_3$ spectra obtained under different circumstances

Figure 4.46 depicts the change on the spectra of $BaTiO_3$ upon applied electric and thermal fields in detail. A low intensity peak appears on the spectra at the same time with the burst of charges as shown in the figure. As mentioned earlier, splitting on the peaks could not be detected during the EDXRD experiments due to high photoelectric absorption as a result of $BaTiO_3$ having a high atomic number (Z_{BaTiO3}=56).

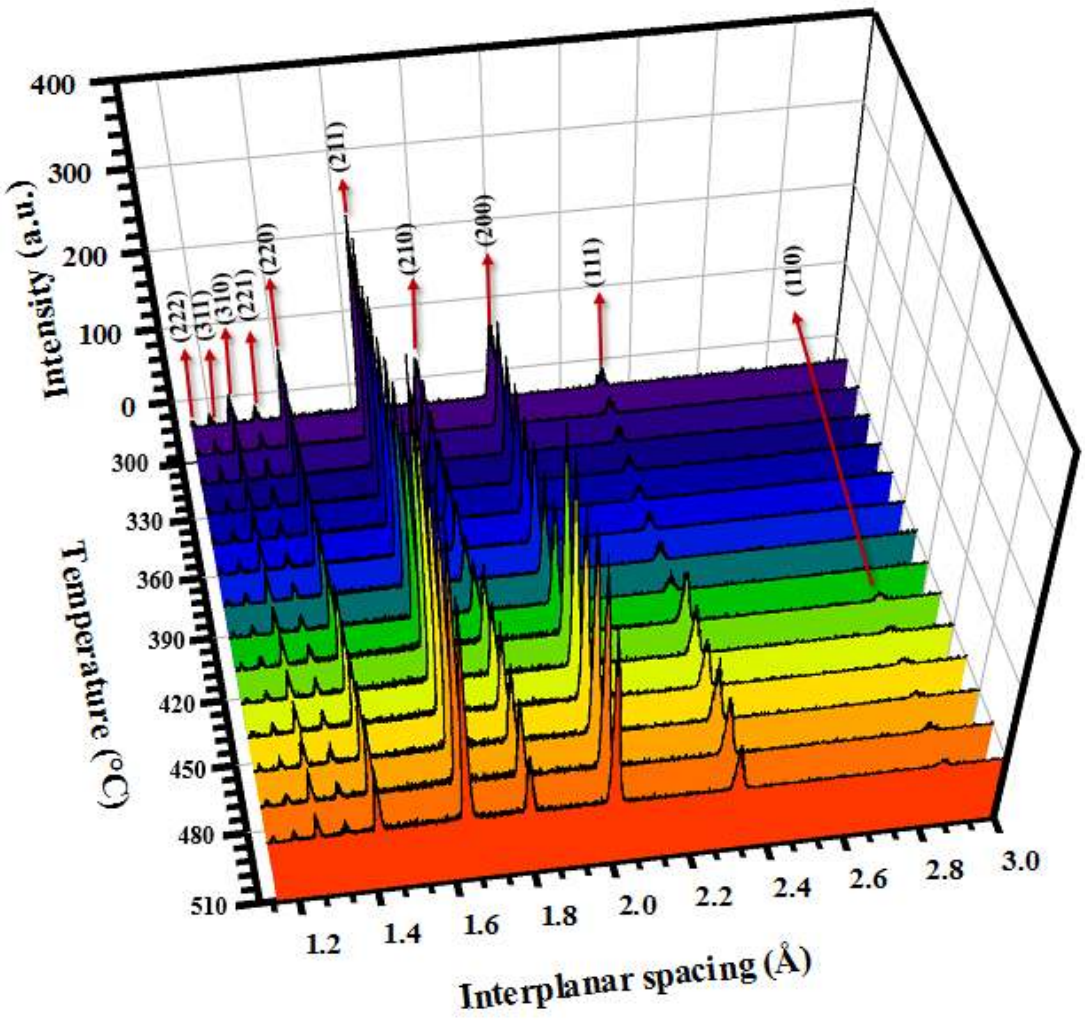

Figure 4. 46. Energy dispersive x-ray diffraction spectra showing the variation in the $BaTiO_3$ specimen under the influence of electric and thermal fields during the flash sintering process

Powder x-ray diffraction analysis of $BaTiO_3$ is of significance after its sintering process. Change in the behavior of unit cell volume expansion based on the data collected using EDXRD reveals that though the material exhibits an expansion in a quadratic trend at atomic level before the current draw, it follows a linear behavior right after the sample receives enough magnitude of current which fact is one of the significant evidences of the phase transformation in the material in question. Resolution issues with EDXRD, and hence, non-detectable splitting on the peaks, required more characterization on the material to support our findings. Therefore, powder x-ray diffraction was used as a complementary method which in turn confirmed our hypothesis on electric field induced structural phase transformation of $BaTiO_3$. Because $BaTiO_3$ specimens pressed using US Research Nanomaterials Inc.[13] powder typically became conductive at temperatures ranging from ~400 °C to ~600 °C, depending on the applied electric field as well as the particle-particle contacts, another thermal experiment was conducted by heating a sample to 600 °C to examine the temperature effect on the structure of $BaTiO_3$ using powder x-ray diffraction. As seen in Figure 4.47, raw sample and the one exposed to thermal field exhibit cubic structure whereas the ones subjected to an electric field of a magnitude indicated on each spectrum and received maximum currents of 0.5 and ~1 A are in tetragonal structure. Splitting, which is not observed on the spectrum of cubic $BaTiO_3$, on (200) peak is identical to the x-ray spectrum of tetragonal $BaTiO_3$, and as seen in the figure, current leakage causes this peak to split into (002) and (200).

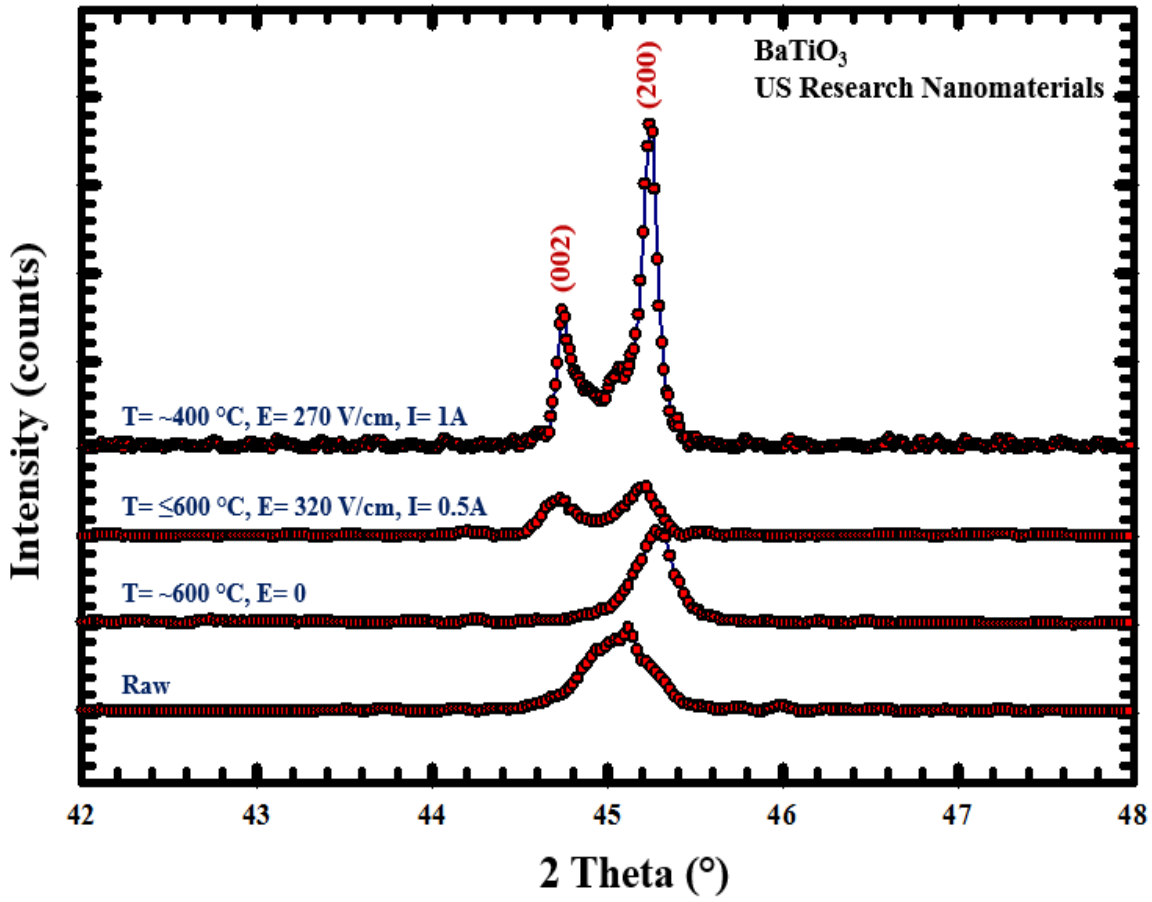

Figure 4. 47. Behavior of (200) $BaTiO_3$[13] peak under different experimental conditions

$BaTiO_3$ specimens based on the powder purchased from Sigma Aldrich Co. LLC.[14] were subjected to similar experiments as the ones explained above. Although 320 V/cm electric field was applied to these samples, they became conductive at higher temperature values (≥850 °C), so the burst event occurred later compared to the previous ones. Therefore, the thermal field experiment was conducted in a temperature range of 980-1250 °C for ≥5 minutes to have a net baseline. It was found out that temperature has no effect on the phase transformation of this material. Maiwa's study[19] on the sintering of $BaTiO_3$ using conventional and SPS methods also confirms that the temperature range we sinter our specimens is not high enough to increase the ferroelectricity of this material. Figure

4.48 illustrates the powder x-ray diffraction patterns of the specimens which were exposed to thermal and electric fields. Applied electric field triggered a phase transformation from cubic to tetragonal structure in these specimens as in the other ones. Additionally, an unidentifiable phase formed in the pellets upon electric field as seen in the figure.

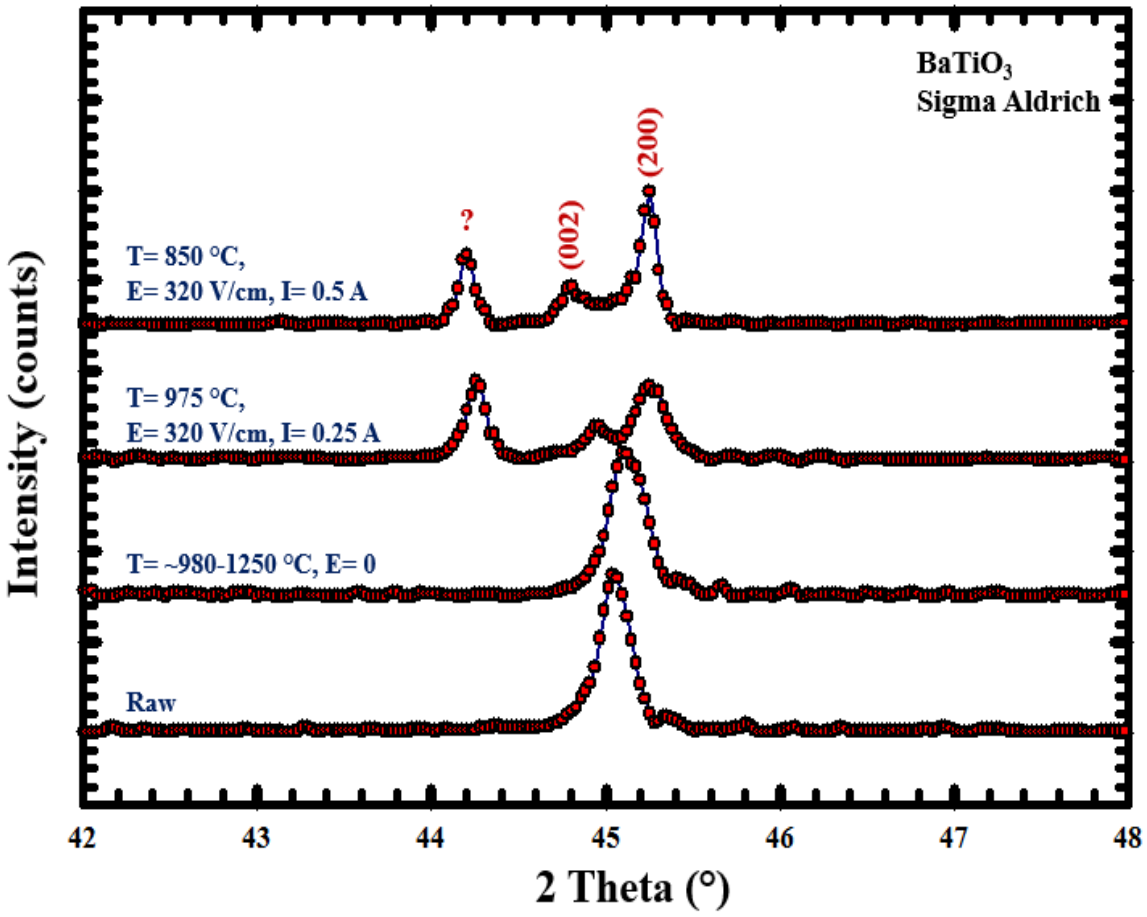

Figure 4. 48. Behavior of (200) $BaTiO_3$[14] peak under different experimental conditions

4.2.4. Electric Field Assisted Densification of $BaTiO_3$

Density of the sample sintered under thermal and 270 V/cm electric fields and received ~1 A current was found to be 92% ρ_{th} based on Archimedes method. As discussed in detail earlier, burst event occurred at 390 °C in 24 seconds in this sample. Temperature

reached 405 °C at the maximum of the unit cell volume. Other specimen based on US Research Nanomaterials powder exhibited 94% density after the sintering process done under 320 V/cm and 0.5 A current cut-off. Although higher electric field was applied on this specimen, it sintered at a higher temperature (~560 °C). SEM images of these samples after sintering process are shown in two different scales in Figure 4.49. Micrographs of the samples is the self-evident of the consolidation event in this material under the aforementioned conditions. SEM images also show that there is grain growth in the first sample during densification (Figure 4.49a and b). Although starting particle size of the powder was 100 nm, some larger grains of ≥1μm were observed on the micrographs. Images taken from the surface of the other specimen (94% ρ_{th}) did not show enough evidence of densification besides necking between the particles (Figure 4.49c and d). Therefore, the fractured surface of this specimen, unlike the other specimens, was also examined to find out whether the measured density value of 94% ρ_{th} was correct or a statistical error. As a result, the fractured surface of the sample confirmed the density measurement (Figure 4.49e and f). This result might be attributed to the fact that the particles on the surface of a sintered sample of <95 % ρ_{th} are not always close enough or in contact.

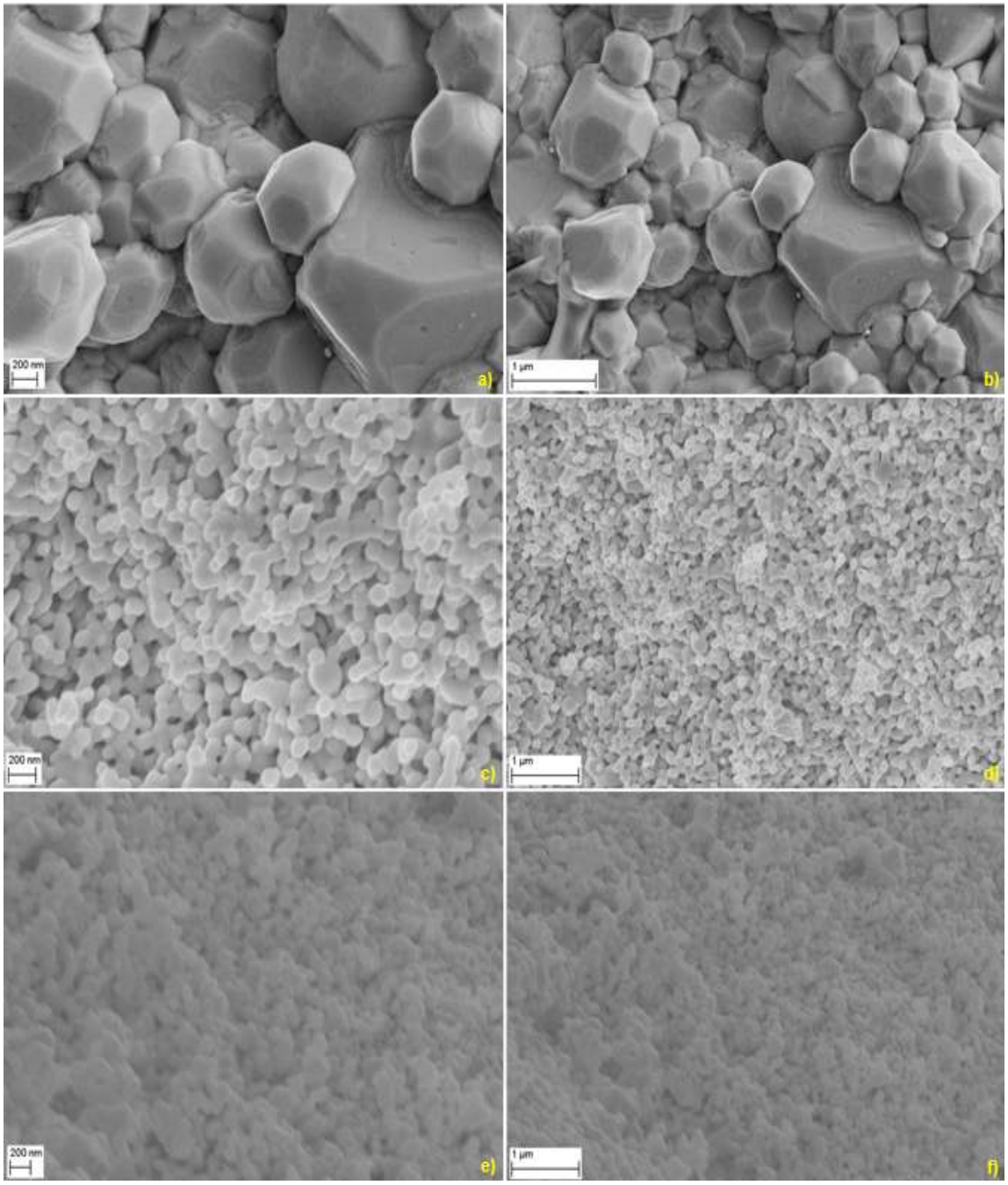

Figure 4. 49. SEM images of 92% ρ_{th} $BaTiO_3$ in **a)** 200 nm and **b)** 1 µm scales from its surface and of 94% ρ_{th} $BaTiO_3$ in **c)** 200 nm and **d)** 1 µm scales from its surface and in **e)** 200 nm and **f)** 1 µm scales from its fractured surface

Figure 4.50 depicts the SEM images of Sigma Aldrich based specimens exposed to ~320 V/cm electric field and received maximum 0.5 A and 0.25 A current. Both specimens

became conductive at almost the same temperature. In detail, 1 mA current leakage on the specimens was observed at 673 °C and 685 °C in the experiments in which the current cut-off was set to 0.5 A and 0.25 A, respectively. However, the burst event occurred at 850 °C and 975 °C for the same experiments, respectively. Pellets were allowed to receive 0.5 A for ~1.5 minutes and 0.25 A for ~1 minute. These specimens were sintered at higher temperatures compared to those based on US Research Nanomaterials powder. Also, more grain growth and more signs of densification were observed on these specimens. Although the densities of the samples in question seem to be ≥95% ρ_{th} according to their micrographs, Archimedes measurements result in ~93% ρ_{th} and ~94% ρ_{th} for the one received 0.5 A and 0.25 A current, respectively.

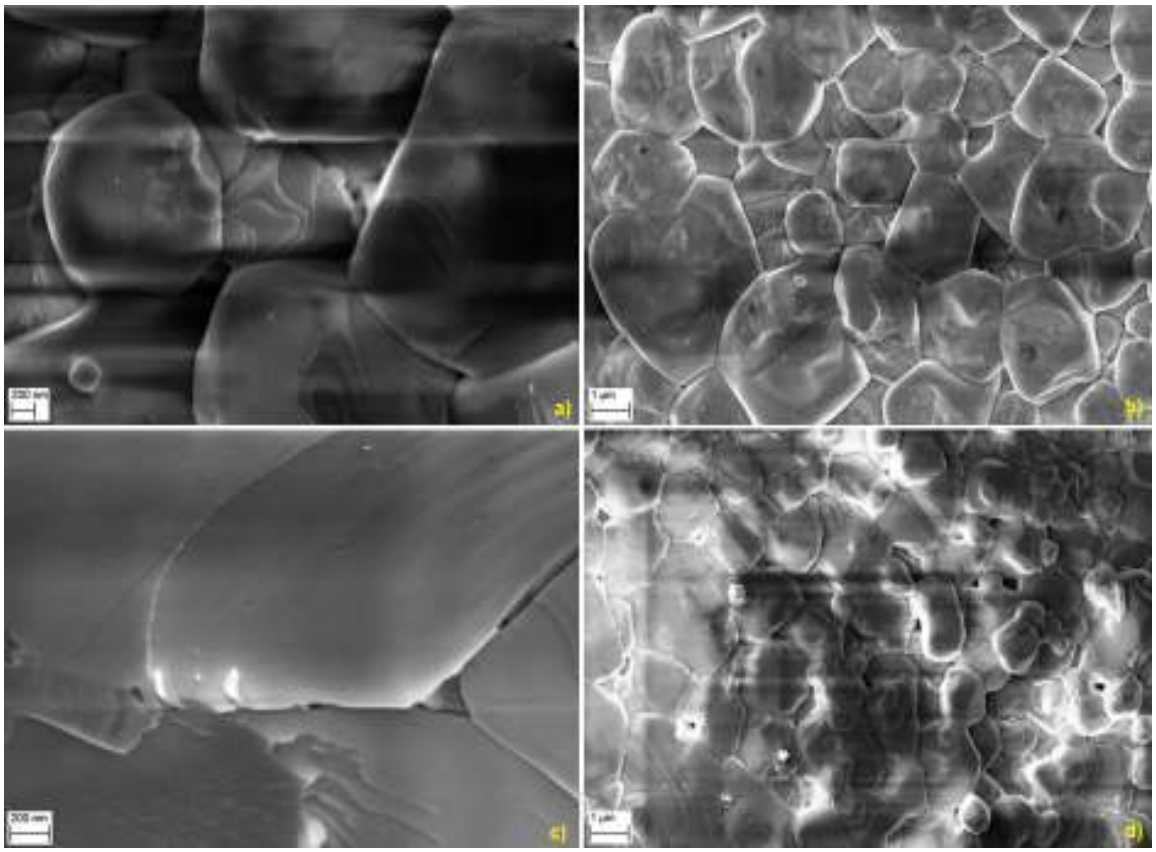

Figure 4. 50. SEM images of $BaTiO_3$ after densification process under 320 V/cm electric field and 0.5 A current cut-off in **a)** 200 nm and **b)** 1 μm scales and under 320 V/cm and 0.25 A current cut-off in **c)** 200 nm and **d)** 1 μm scales

4.2.5. Thermodynamic Approach to the Burst Event in $BaTiO_3$ under 270 V/cm Electric Field

Figure 4.51 shows the variation in the power to which the $BaTiO_3$ specimen is subjected. The specimen shows no conductivity till 320 °C at which temperature value the current leakage of 0.03 A is observed. Since the surfaces of the specimen were painted with silver paste to have ohmic contacts between the sample and electrodes through which the electric field was applied, the current leakage was observed at a lower temperature than the expected value. The onset stage in the flash sintering process begins with the observation of the current flow even though it is very small, 0.03 A in this experiment as mentioned

above. The burst of the charges takes place at 390 °C with a humongous increase in the current flow. The burst event takes only 24 seconds in which time span most of the densification work is done and the density of the sample reaches its maximum of 92% ρ_{th}. Temperature reaches 405 °C when the current flow reaches its maximum, ~1 A. The area under the power curve during the burst event, which represents the work done by the applied electric field during the burst, was integrated, and it was found to be 385.902 Ws. This value was used to find the theoretical internal temperature limit of $BaTiO_3$ by assuming 100% electric to Joule heating conversion which is unlikely to be possible because this assumption actually breaks the second law of thermodynamics. Calculation from the C_p formula of $BaTiO_3$ gained using the data published by Babu et al.[136] yielded a temperature value of ~5050 °C. In other words, a $BaTiO_3$ sample should be heated up to ~5050 °C to acquire the same magnitude of work in the same time span under zero electric field. This result also supports that there is not a considerable Joule heating in the system because the measured furnace temperature just next to the specimen is far lower than this estimated value. However, some other mechanisms should be active in the material to result in such a high density in such a short time.

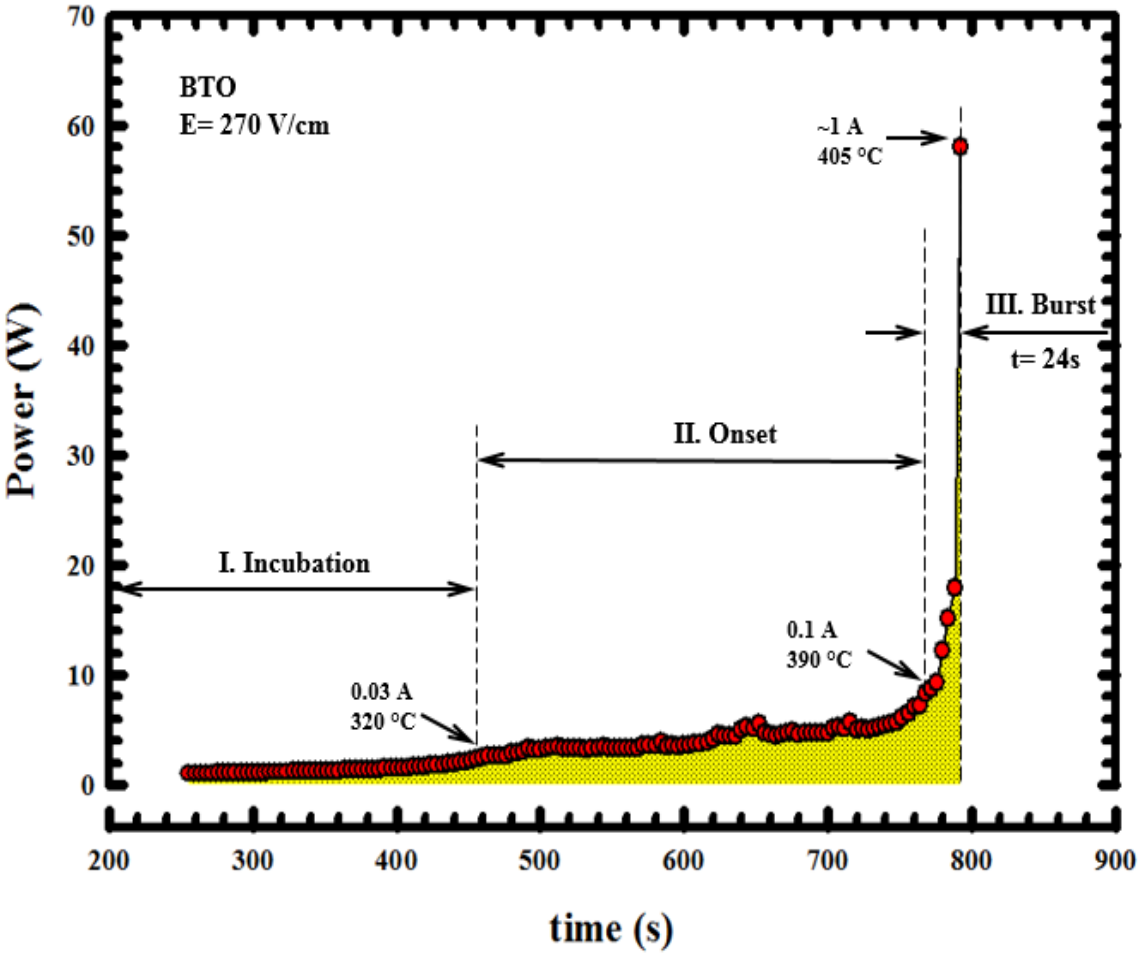

Figure 4. 51. Power (W) vs time (s) graph acquired under 270 V/cm electric field

5. Conclusions

In this study, effects of a dc electric field on nano-TiB_2 and nano-$BaTiO_3$ were studied. Given the high temporal resolution of EDXRD method, all crystallochemical changes in these materials coupled with the effects of temperature and electric field were measured.

The present dissertation study reveals the following;

1) Flash sintering, a.k.a. burst mode densification, is a transient state phenomena which decreases the densification temperature of a material to 30-70% of its conventional sintering temperature. Also, this technique enables one to sinter a material at an ultra-short time scale as small as 1-2 orders of magnitude less than its conventional sintering time.

2) Due to high oxidation tendency nature of TiB_2, this material does not consolidate under electric field. Oxygen phases, such as TiO_2, $TiBO_3$, and B_2O_3, existent in TiB_2 powder aggressively prevent this material from densifying. Applied electric field causes a transformation between these oxide phases as higher electric field accelerates this process. A dc electric field directly imposed on a TiB_2 specimen triggers an additional oxidation process as well. Although, the required temperature for oxidation of TiB_2 in air is $\geq$850 °C, electric field decreases it to as low as 305 °C in an inert atmosphere (Argon). A tentative model proposed here in this study suggests four steps for the reaction between oxygen and TiB_2 particles under an applied electric field; (i) Diffusion of O_2 in ambient atmosphere, (ii) Dissolution of O_2 at interface between atmosphere and oxide layer surrounding a TiB_2

particle, (iii) Diffusion of O_2 in oxygen layer, (iv) Chemical reaction of O_2 with TiB_2. Electric field induced possible reactions occurring in TiB_2 specimens containing significant amount of oxide are;

$$4TiO_2 + 2B_2O_3 \rightarrow 4TiBO_3 + O_2$$

$$4TiB_2 + 9O_2 \rightarrow 4TiBO_3 + 2B_2O_3$$

3) Flash sintering method results in high densification (92% - 94% ρ_{th}) in $BaTiO_3$, unlike TiB_2. A directly imposed electric field on a nano-$BaTiO_3$ specimen instigates a transformation from paraelectric to ferroelectric phase in $BaTiO_3$. (200) peak on its x-ray spectrum splits into (002) and (200) due to the distortion from cubic to tetragonal structure stems from the stress induced into the system by applied electric field.

4) Density increase and structural phase transformation in $BaTiO_3$ and sudden oxidation and phase transformation between oxides in TiB_2 at very low temperature values in very short time scales should be corresponding with the anomalous expansion in the unit cell volume of each material. Given the fact of the material being perturbed from the onset of flash sintering temperature till the end of the burst, the system is all in non-equilibrium condition during which equilibrium properties should not be under consideration.

6. Suggestions for Future Work

Following suggestions might be considered for future work towards the improvement of the work presented in this study;

1) Since TiB_2 has a high oxygen tendency nature, it is difficult to prevent this material from oxidizing. A better quality powder containing less than 1% oxygen will increase the sinterability of this material in a dry enough inert gas atmosphere. Sintering additives, such as SiC and B_4C, will be used to let the native oxygen content as well as that pushed into the system by electric field leave the material as CO_2 during the burst of charges on a purpose of increasing its density. As the final option to eliminate oxidation of this material, a vacuum furnace will be used to completely isolate the specimen being worked on from environment.

2) Although $BaTiO_3$ densified upon an applied electric field, maximum density obtained was measured as 94% ρth after the application of maximum 320 V/cm. Also, some considerable grain growth was observed on the specimens. Densification of a material is proportional to the power it absorbs. Density of a specimen can be increased by increasing the applied voltage and setting the current cut-off to a value ≤0.1 A. Therefore, the material absorbs same or more magnitude of power while receiving less current which in turn increases the density of the specimen without melting it. This might also help to suppress the grain growth. A recently purchased power source which is capable of applying 1000 V and 5 A will be used in an attempt to improve the results presented in this study. Besides, due to the instant phase transformation from cubic to tetragonal structure in

$BaTiO_3$, microcracks form in the system cause the specimen to break as a result of which electrical properties of this material cannot properly be measured. Lower current cut-off will also be a solution to this problem.

Appendix A.

In an attempt to find out the effects of flash sintering process on electrical properties of $BaTiO_3$, some piezoelectric coefficient (d_{33}) measurements were carried out. However, because this material goes under a phase transformation from cubic to tetragonal structure with current leakage, as explained in the results and conclusions, specimens being worked on mostly lose their circular shapes, which is a must for the measurement of electrical properties, at the end of each experiment. Painting the surfaces of each specimen with silver paste followed by poling process. Although two of the samples failed in this step due to their shapes, piezoelectric coefficient of one sample (94% ρ_{th} at T $\leq$600 °C under E= 320 V/cm and I= 0.5 A) could be measured and found out to be 170 ± 4 pC/N at RT. Compared to typical d_{33} value of $BaTiO_3$, 190 pC/N,[139] this value seems to be promising.

References

1 G.B. Raju, B. Basu, N.H. Tak, and S.J. Cho, "Temperature dependent hardness and strength properties of TiB_2 with $TiSi_2$ sinter-aid," *J. Eur. Ceram. Soc.*, **29** [10] 2119–2128 (2009).

2 M. Cologna, B. Rashkova, and R. Raj, "Flash sintering of nanograin zirconia in <5 s at 850°C," *J. Am. Ceram. Soc.*, **93** [11] 3556–3559 (2010).

3 J.L. Murray, P.K. Liao, and K.E. Spear, "The B-Ti (Boron-Titanium) System," *Bull. Alloy Phase Diagrams*, **7** [6] 550–555 (1986).

4 R.G. Munro, "Material properties of titanium diboride," *J. Res. Natl. Inst. Stand. Technol.*, **105** [5] 709–720 (2000).

5 B. Basu, G.B. Raju, and A.K. Suri, "Processing and properties of monolithic TiB_2 based materials," *Int. Mater. Rev.*, **51** [6] 352–374 (2006).

6 W.G. Fahrenholtz, G.E. Hilmas, I.G. Talmy, and J. a. Zaykoski, "Refractory Diborides of Zirconium and Hafnium," *J. Am. Ceram. Soc.*, **90** [5] 1347–1364 (2007).

7 A.G. Atkins and D. Tabor, "Hardness and deformation properties of solids at very high temperatures," *Proc. R. Soc. A*, **292** 441–459 (1966).

8 G.B. Raju and B. Basu, "Densification, Sintering Reactions, and Properties of Titanium Diboride With Titanium Disilicide as a Sintering Aid," *J. Am. Ceram. Soc.*, **90** [11] 3415–3423 (2007).

9 G.B. Raju, B. Basu, and A.K. Suri, "Oxidation Kinetics and Mechanisms of Hot-Pressed TiB_2 -$MoSi_2$ Composites," *J. Am. Ceram. Soc.*, **91** [10] 3320–3327 (2008).

10 G.H. Haertling, "Ferroelectric Ceramics: History and Technology," *J. Am. Ceram. Soc.*, **82** [4] 797–818 (1999).

11 M.B. Smith, K. Page, T. Siegrist, P.L. Redmond, E.C. Walter, R. Seshadri, L.E. Brus, and M.L. Steigerwald, "Crystal Structure and the Paraelectric-to-Ferroelectric Phase Transition of Nanoscale BaTiO 3," *J. Am. Chem. Soc.*, **130** [14] 6955–6963 (2008).

12 E.K. Akdoğan, I. Şavklıyıldız, H. Biçer, W. Paxton, F. Toksoy, Z. Zhong, and T. Tsakalakos, "Anomalous lattice expansion in yttria stabilized zirconia under simultaneous applied electric and thermal fields: A time-resolved in situ energy dispersive x-ray diffractometry study with an ultrahigh energy synchrotron probe," *J. Appl. Phys.*, **113** [23] 233503 (2013).

[13] US Research Nanomaterials Inc., *Barium Titanate Nanopowder (99.9%, 100nm, cubic)*, *2015*, (n.d.).

[14] Sigma Aldrich Co. LLC., *Barium Titanate Nanopowder (99% trace metals basis, <100 nm, cubic)*, (2015).

[15] J. Li, X. Lü, Y. Lai, Q. Li, and Y. Liu, "Research Progress in TiB_2 Wettable Cathode for Aluminum Reduction," *JOM*, **60** [8] 32–37 (2008).

[16] P.S. Mohanty and J.E. Gruzleskit, "Mechanism of grain refinement in aluminum," *Pergamon*, **43** [5] 2001–2012 (1995).

[17] S.G. Huang, K. Vanmeensel, O.J. a. Malek, O. Van der Biest, and J. Vleugels, "Microstructure and mechanical properties of pulsed electric current sintered B4C–TiB_2 composites," *Mater. Sci. Eng. A*, **528** [3] 1302–1309 (2011).

[18] S. Luo, Z. Tang, W. Yao, and Z. Zhang, "Low-temperature combustion synthesis and characterization of nanosized tetragonal barium titanate powders," *Microelectron. Eng.*, **66** 147–152 (2003).

[19] H. Maiwa, "Preparation and properties of $BaTiO_3$ ceramics by spark plasma sintering," *Jpn. J. Appl. Phys.*, **3** 1–22 (2008).

[20] X.-H. Wang, X.-Y. Deng, H.-L. Bai, H. Zhou, W.-G. Qu, L.-T. Li, and I.-W. Chen, "Two-Step Sintering of Ceramics with Constant Grain-Size, II: $BaTiO_3$ and Ni-Cu-Zn Ferrite," *J. Am. Ceram. Soc.*, **89** [2] 438–443 (2006).

[21] G. Cabouro, S. Le Gallet, S. Chevalier, E. Gaffet, Y. Grin, and F. Bernard, "Dense $MoSi_2$ produced by reactive flash sintering: Control of Mo/Si agglomerates prepared by high-energy ball milling," *Powder Technol.*, **208** [2] 526–531 (2011).

[22] J. a. Downs and V.M. Sglavo, "Electric Field Assisted Sintering of Cubic Zirconia at 390°C," *J. Am. Ceram. Soc.*, **96** [5] 1342–1344 (2013).

[23] J.S.C. Francis, M. Cologna, and R. Raj, "Particle size effects in flash sintering," *J. Eur. Ceram. Soc.*, **32** [12] 3129–3136 (2012).

[24] A. Gaur and V.M. Sglavo, "Flash-sintering of MnCO2O4 and its relation to phase stability," *J. Eur. Ceram. Soc.*, **34** [10] 2391–2400 (2014).

[25] A. Karakuscu, M. Cologna, D. Yarotski, J. Won, J.S.C. Francis, R. Raj, and B.P. Uberuaga, "Defect Structure of Flash-Sintered Strontium Titanate," *J. Am. Ceram. Soc.*, **95** [8] 2531–2536 (2012).

[26] R. Muccillo and E.N.S. Muccillo, "An experimental setup for shrinkage evaluation during electric field-assisted flash sintering: Application to yttria-stabilized zirconia," *J. Eur. Ceram. Soc.*, **33** [3] 515–520 (2013).

[27] J. Narayan, "Grain growth model for electric field-assisted processing and flash sintering of materials," *Scr. Mater.*, **68** [10] 785–788 (2013).

[28] M.C. Steil, D. Marinha, Y. Aman, J.R.C. Gomes, and M. Kleitz, "From conventional ac flash-sintering of YSZ to hyper-flash and double flash," *J. Eur. Ceram. Soc.*, **33** [11] 2093–2101 (2013).

[29] H. Yoshida, Y. Sakka, T. Yamamoto, J.-M. Lebrun, and R. Raj, "Densification behaviour and microstructural development in undoped yttria prepared by flash-sintering," *J. Eur. Ceram. Soc.*, **34** [4] 991–1000 (2014).

[30] E. Zapata-Solvas, S. Bonilla, P.R. Wilshaw, and R.I. Todd, "Preliminary investigation of flash sintering of SiC," *J. Eur. Ceram. Soc.*, **33** [13-14] 2811–2816 (2013).

[31] M. Cologna, J.S.C. Francis, and R. Raj, "Field assisted and flash sintering of alumina and its relationship to conductivity and MgO-doping," *J. Eur. Ceram. Soc.*, **31** [15] 2827–2837 (2011).

[32] M. Cologna, A.L.G. Prette, and R. Raj, "Flash-Sintering of Cubic Yttria-Stabilized Zirconia at 750°C for Possible Use in SOFC Manufacturing," *J. Am. Ceram. Soc.*, **94** [2] 316–319 (2011).

[33] R. Raj, "Joule heating during flash-sintering," *J. Eur. Ceram. Soc.*, **32** [10] 2293–2301 (2012).

[34] J.C. Walker, "Synthesis of TiB_2 by the borothermic/carbothermic reduction of TiO2 with B4C," *Adv. Ceram. Mater.*, **3** [6] 601–604 (1988).

[35] V.A. Neronov, M.A. Korchagin, V. V. Aleksandrov, and S.N. Gusenko, "Investigation of the Interaction between Boron and Titanium," *J. Less Common Met.*, **82** 125–129 (1981).

[36] R.L. Axelbaum, D.P. Dufaux, and C.A. Frey, "A Flame Process for Synthesis of Unagglomerated , Low- Oxygen Nanoparticles : Application to Ti and TiB 2," **28** [December] 1199–1211 (1997).

[37] H.R. Baumgartner and R.A. Steiger, "Sintering and Properties of Titanium Diboride Made from Powder Synthesized in a Plasma-Arc Heater," *J. Am. Ceram. Soc.*, **67** [3] 207–212 (1983).

[38] S.E. Bates and W.E. Buhro, "Synthesis of titanium boride (TiB)2 nanocrystallites by solution-phase processing," *J. Mater. Res.*, **10** [10] 2599–2612 (1995).

[39] M. Ziemnicka-Sylwester, "TiB_2-Based Composites for Ultra-High-Temperature Devices, Fabricated by SHS, Combining Strong and Weak Exothermic Reactions," *Materials (Basel).*, **6** [5] 1903–1919 (2013).

[40] K.B. Panda and K.S. Ravi Chandran, "Determination of elastic constants of titanium diboride (TiB_2) from first principles using FLAPW implementation of the density functional theory," *Comput. Mater. Sci.*, **35** [2] 134–150 (2006).

[41] K. Schwarz, "Band Structure and Chemical Bonding in Transition Metal Carbides and Nitrides," *CRC Crit. Rev. Solid State Mater. Sci.*, **13** [3] 211–257 (1987).

[42] D. Vallauri, I.C.A. Adrián, and A. Chrysanthou, "TiC–TiB_2 composites: A review of phase relationships, processing and properties," *J. Eur. Ceram. Soc.*, **28** [8] 1697–1713 (2008).

[43] R. Telle, "Boride and carbide ceramics;" p. 175 in *Mater. Sci. Technol.*, Vol. 11. Edited by R.W. Cahn. VCH, Weinheim, 1994.

[44] R.A. Cutler, "Engineering properties of borides;" pp. 787–803 in *Eng. Mater. Handb.* Edited by J.S. Schneider. ASM International, Metals Park, Ohio, 1991.

[45] Y.-M. Chiang, D.P. Birnie, and W.D. Kingery, *Physical Ceramics: Principles for Ceramic Science and Engineering*. John Wiley & Sons, New York, 1997.

[46] G. Goor, P. Sagesser, and K. Berroth, "Electrically conductive ceramic composites," *Solid State Ionics*, **101** [103] 1163–1170 (1997).

[47] T.S.R.C. Murthy, B. Basu, R. Balasubramaniam, a. K. Suri, C. Subramanian, and R.K. Fotedar, "Processing and Properties of TiB_2 with $MoSi_2$ Sinter-additive: A First Report," *J. Am. Ceram. Soc.*, **89** [1] 131–138 (2006).

[48] K. Biswas, B. Basu, a Suri, and K. Chattopadhyay, "A TEM study on TiB_2–20%$MoSi_2$ composite: Microstructure development and densification mechanism," *Scr. Mater.*, **54** [7] 1363–1368 (2006).

[49] B. Todorovic, T. Jokic, Z. Rakocevic, Z. Markovic, B. Gakovic, and T. Nenadovic, "The effect of rapid thermal annealing on structural and electrical properties of TiB_2 thin films," *Thin Solid Films*, **300** 272–277 (1997).

[50] A.D. McLeod, J.S. Haggerty, and D.R. Sadoway, "Electrical Resistivities of Monocrystalline and Polycrystalline TiB_2," *J. Am. Ceram. Soc.*, **67** [11] 705–708 (1984).

[51] C. Martin, B. Cales, P. Vivier, and P. Mathieu, "Electrical discharge machinable ceramic composites," *Mater. Sci. Eng.*, **A109** 351–356 (1989).

[52] L. Li, H. Kim, and E. Son, "Sintering and mechanical properties of titanium diboride with aluminum nitride as a sintering aid," *J. Eur. Ceram. Soc.*, **22** 973–977 (2002).

[53] G. V. Samsonov, P. Hagenmuller, and T. Lundstrom, "II . The Nature of the Chemical Bond in Borides A);" pp. 19–30 in *Boron Refract. Borides, Nat. Chem. Bond Borides*. Springer-Verlag, New York, 1977.

[54] H.L. Holleck, H. Leiste, and W. Schneider, *High Tech Ceramics*. Elsevier Science Publishers, Amsterdam, 1987.

[55] M.K. Ferber, P.F. Becher, and C.B. Finch, "Effect of Microstructure on the Properties of TiB_2 Ceramics," *J. Am. Ceram. Soc.*, **66** C2–C3 (1983).

[56] S. Madtha, C. Lee, and K.S. Ravi Chandran, "Physical and Mechanical Properties of Nanostructured Titanium Boride (TiB) Ceramic," *J. Am. Ceram. Soc.*, **91** [4] 1319–1321 (2008).

[57] S.-Q. Guo, "Densification of ZrB2-based composites and their mechanical and physical properties: A review," *J. Eur. Ceram. Soc.*, **29** [6] 995–1011 (2009).

[58] T. Graziani and A. Bellosi, "Sintering and Characterization of TiB_2–B4C–ZrO2 Composites," *Mater. Manufact. Process.*, **9** [4] 767–80 (1994).

[59] E.S. Kang and C.H. Kim, "Improvements in Mechanical Properties of TiB_2 by the Dispersion of B4C Particles," *J. Mater. Sci.*, **25** 580–584 (1990).

[60] Y. Murata, H.P. Julien, and E.D. Whitney, "Densification and Wear Resistance of Ceramic Systems: I. Titanium Diboride," *Ceram. Bull.*, **46** [7] 643–648 (1967).

[61] S.K. Bhaumik, C. Diwakar, A.K. Singh, and G.S. Upadhyaya, "Synthesis and Sintering of TiB_2 and TiB_2–TiC Composite Under High Pressure," *Mater. Sci. Eng. A*, **279** 275–281 (2000).

[62] J.M. Sanchez, I. Azcona, and F. Castro, "Mechanical properties of titanium diboride based cermets," *J. Mater. Sci.*, **35** 9–14 (2000).

[63] P. Yih and D.D.L. Chung, "Titanium diboride copper-matrix composites," *J. Mater. Sci.*, **32** 1703–1709 (1997).

[64] Z.Y. Ma and S.C. Tjong, "High temperature creep behavior of in-situ TiB2 particulate reinforced copper-based composite," **284** 70–76 (2000).

[65] Q. Xu, X. Zhang, J. Han, X. He, and V.L. Kvanin, "Combustion synthesis and densification of titanium diboride–copper matrix composite," *Mater. Lett.*, **57** [28] 4439–4444 (2003).

[66] Y. Muraoka, M. Yoshinaka, K. Hirota, and O. Yamaguchi, "Hot Isostatic Pressing of TiB_2-ZrO2 (2 mol% Y2O3) Composite Powders," *Mater. Res. Bull.*, **31** [7] 787–792 (1996).

[67] S. Torizuka, K. Sato, H. Nishio, and T. Kishi, "Effect of SiC on Interfacial Reaction and Sintering Mechanism of TiB_2," *J. Am. Ceram. Soc.*, **78** [6] 1606–1610 (1995).

[68] J. Park, Y. Koh, H. Kim, C.S. Hwang, and E.S. Kang, "Densification and Mechanical Properties of Titanium Diboride with Silicon Nitride as a Sintering Aid," *J. Am. Ceram. Soc.*, **82** 3037–3042 (1999).

[69] S.H. Kang and D.J. Kim, "Pressureless Sintering and Properties of Titanium Diboride Ceramics Containing Chromium and Iron," **84** [4] 893–895 (2001).

[70] A. Pettersson, P. Magnusson, P. Lundberg, and M. Nygren, "Titanium–titanium diboride composites as part of a gradient armour material," *Int. J. Impact Eng.*, **32** [1-4] 387–399 (2005).

[71] M. Faraday, "Supplementary Note to Experimental Researches in Electricity . Eleventh Series," *Phil. Trans. R. Soc. Lond.*, **128** [1] 79–81 (1838).

[72] A. Moulson and J.M. Herbert, *Electroceramics-Materials-properties-applications*. Chapman and Hall, London, 1990.

[73] N. Nikulin, *Fundamentals of electrical materials*. Mir Publishers, Moscow, 1988.

[74] D.W. Richerson, *Modern ceramic engineering: Properties, processing, and use in design*, 2nd ed. Marcel Dekker, 1992.

[75] A. Hall, M. Allahverdi, E.K. Akdogan, and A. Safari, "Piezoelectric/electrostrictive multimaterial PMN-PT monomorph actuators," *J. Eur. Ceram. Soc.*, **25** [12] 2991–2997 (2005).

[76] A. Navrotsky and D.J. Weidner, *Perovskite: A Structure of Great Interest to Geophysics and Materials Science*. American Geophysics Union, Washington, DC, 1989.

[77] J. Nath, D. Ghosh, J.-P.M. Maria, A.I. Kingon, W. Fathelbab, P.D. Franzon, and M.B. Steer, "An Electronically Tunable Microstrip Bandpass Filter Using Thin-Film Barium – Strontium – Titanate (BST) Varactors," *IEEE Trans. Microw. Theory Tech.*, **53** [9] 2707–2712 (2005).

[78] R. Ramesh and N.A. Spaldin, "Multiferroics : progress and prospects in thin films," *Nat. Mater.*, **6** 21–29 (2007).

[79] M.-F. Chang, P.-T. Lee, S.P. McAlister, and A. Chin, "A flexible organic pentacene nonvolatile memory based on high- κ dielectric layers," *Appl. Phys. Lett.*, **93** [23] 233302 (2008).

[80] B. Charlot, W. Sun, K. Yamashita, H. Fujita, and H. Toshiyoshi, "Bistable nanowire for micromechanical memory," *J. Micromechanics Microengineering*, **18** [4] 045005 (2008).

[81] D.-G. Sun, Z. Liu, Y. Huang, S.-T. Ho, D.J. Towner, and B.W. Wessels, "Performance simulation for ferroelectric thin-film based waveguide electro-optic modulators," *Opt. Commun.*, **255** [4-6] 319–330 (2005).

[82] M.Y. Zhuravlev, R.F. Sabirianov, S.S. Jaswal, and E.Y. Tsymbal, "Giant Electroresistance in Ferroelectric Tunnel Junctions," *Phys. Rev. Lett.*, **94** [24] 246802 (2005).

[83] P. Muralt, "Ferroelectric thin films for micro-sensors and actuators : a," *J. Micromechanics Microengineering*, **136** 136–146 (2000).

[84] P. Muralt, "Micromachined infrared detectors based on pyroelectric thin films," *Reports Prog. Phys.*, **64** 1339 (2001).

[85] J. Ho, T.R. Jow, and S. Boggs, "Historical Introduction to Capacitor," *IEEE Electr. Insul. Mag.*, **26** [1] 20–25 (2010).

[86] D. Richerson, *Modern Ceramic Engineering: Properties, Processing, and Use in Design*, 3rd ed. CRC Press, New York, 1992.

[87] H. Han, D. Ghosh, J.L. Jones, and J.C. Nino, "Colossal permittivity in microwave-sintered barium titanate and effect of annealing on dielectric properties," *J. Am. Ceram. Soc.*, **96** [2] 485–490 (2013).

[88] A.F. Devonshire, "Theory of Barium Titanate - Part II," *Philos. Mag.*, **42** 1065–1079 (1951).

[89] A.F. Devonshire, "Theory of Barium Titanate - Part I," *Philos. Mag.*, **40** 1040–1063 (1949).

[90] J.P. Remeika and W.M. Jackson, "A Method for Growing Barium Titanate Single Crystals," *J. Am. Chem. Soc.*, **76** [3] 940–941 (1954).

[91] H.F. Kay and P. Vousden, "Symmetry changes in barium titanate at low temperatures and their relation to its ferroelectric properties," *Philos. Mag. J. Sci.*, **40** [309] 1019–1040 (1949).

[92] W.P. Mason and B.T. Matthias, "Theoretical model for explaining the ferroelectric effect in barium titanate," *Phys. Rev.*, **74** [11] 1622–1636 (1948).

[93] H.D. Megaw, "Origin of ferroelectricity in barium titanate and other perovskite-type crystals," *Acta Crystallogr.*, **5** [6] 739–749 (1952).

[94] W.P. Mason, "Aging of the Properties of Barium Titanate and Related Ferroelectric Ceramics," *J. Acoust. Soc. Am.*, **27** [1] 73–85 (1955).

[95] D. Meyerhofer, "Transition to the ferroelectric state in barium titanate," *Phys. Rev.*, **112** [2] 413–423 (1958).

[96] D.W. Richerson, *Modern Ceramic Engineering*, 2nd ed. CRC Press, New York, 1992.

[97] V. Giurgiutiu, *Structural Health Monitoring: with Piezoelectric Wafer Active Sensors*, 1st ed. Academic Press, Burlington, 2008.

[98] N. Basile, M. Gonon, F. Petit, and F. Cambier, "Interaction between laser beam and BaTiO 3 powders in selective laser sintering treatments," *J. Eur. Ceram. Soc.*, **32** [12] 3303–3311 (2012).

[99] Z. Cen, H. Yang, C. Zhou, Q. Zhou, J. Cheng, C. Yuan, and W. Li, "Effect of sintering temperature on microstructure and piezoelectric properties of Pb-free BiFeO3-$BaTiO_3$ ceramics in the composition range of large BiFeO3 concentrations," *J. Electroceramics*, **31** [1-2] 15–20 (2013).

[100] M. Kong, S. Jiang, T. Xie, and H. Zhang, "Low temperature sintering properties of Y-doped $BaTiO_3$ ceramics by BaB2O4 sintering aid," *Microelectron. Eng.*, **86** [11] 2320–2323 (2009).

[101] B. Li, X. Wang, M. Cai, L. Hao, and L. Li, "Densification of uniformly small-grained $BaTiO_3$ using spark-plasma-sintering," *Mater. Chem. Phys.*, **82** [1] 173–180 (2003).

[102] Y. Li, H. Liu, F. Liu, C. Li, B. Chen, and W. Dong, "A simple approach to porous low-temperature-sintering BaTiO 3," *Sci. China Chem.*, **55** [9] 1765–1769 (2012).

[103] J.C.C. Lin and W.C.J. Wei, "Low-temperature sintering of $BaTiO_3$ with Mn-Si-O glass," *J. Electroceramics*, **25** [2-4] 179–187 (2010).

[104] K. Samuvel and K. Ramachandran, "High calcination of ferroelectric $BaTiO_3$ doped Fe nanoceramics prepared by a solid-state sintering method," *Spectrochim. Acta Part A Mol. Biomol. Spectrosc.*, **146** 113–118 (2015).

[105] Y. Sato, M. Terauchi, S. Kameoka, and a.-P. Tsai, "Optical properties of Group X-XII intermetallic compounds studied by HR-EELS," *Microscopy*, **63** [suppl 1] i18–i19 (2014).

[106] Sonia, R.K. Patel, P. Kumar, C. Prakash, and D.K. Agrawal, "Low temperature synthesis and dielectric, ferroelectric and piezoelectric study of microwave sintered $BaTiO_3$ ceramics," *Ceram. Int.*, **38** [2] 1585–1589 (2012).

[107] T. Takeuchi, Y. Suyama, D.C. Sinclair, and H. Kageyama, "Spark-plasma-sintering of fine $BaTiO_3$ powder prepared by a sol-crystal method," *J. Mater. Sci.*, **36** [9] 2329–2334 (2001).

[108] D. Völtzke, H. Abicht, J. Woltersdorf, and E. Pippel, "Surface modification of pre-sintered BaTiO 3 particles," *Mater. Chem. Phys.*, **73** 274–280 (2002).

[109] C.J. Xiao, Z.H. Chi, S.M. Feng, F.Y. Li, L.C. Chen, C.Q. Jin, X.H. Wang, L.T. Li, *et al.*, "Ferroelectricity of 30 nm $BaTiO_3$ ceramics prepared by high pressure sintering," *J. Electroceramics*, **21** [1-4 SPEC. ISS.] 39–42 (2008).

[110] S. Yoon, J. Dornseiffer, Y. Xiong, D. Grüner, Z. Shen, S. Iwaya, C. Pithan, and R. Waser, "Synthesis, spark plasma sintering and electrical conduction mechanism in $BaTiO_3$-Cu composites," *J. Eur. Ceram. Soc.*, **31** [5] 773–782 (2011).

[111] J.-C. M'Peko, J.S.C. Francis, and R. Raj, "Field-assisted sintering of undoped $BaTiO_3$: Microstructure evolution and dielectric permittivity," *J. Eur. Ceram. Soc.*, **34** [15] 3655–3660 (2014).

[112] M.M. Billah, A. Mousharraf, M.F. Islam, M. Engineering, and C. Engineering, "The Effect of Sintering Time on the Densification of Pure Nano-Sized $BaTiO_3$;" pp. 18–20 in *Int. Conf. Mech. Eng. 2011*. 2011.

[113] K.L. Ying and T.E. Hsieh, "Sintering behaviors and dielectric properties of nanocrystalline barium titanate," *Mater. Sci. Eng. B Solid-State Mater. Adv. Technol.*, **138** [3] 241–245 (2007).

[114] Y. Hirata, A. Nitta, and M. Kawabata, *Microstructure and Dielectric Properties of* $BaTiO_3$ *Prepared by Colloidal Processing*. 1994.

[115] Y. Hirata, A. Nitta, S. Sameshima, and Y. Kamino, "Dielectric properties of barium titanate prepared by hot isostatic pressing," *Mater. Lett.*, **29** [December] 229–234 (1996).

[116] T. Kawashima and Y. Suzuki, "High-temperature X-ray diffraction analysis and reactive sintering of $BaTiO_3$ piezoelectric ceramics," *J. Ceram. Soc. Japan*, **123** [2] 83–85 (2015).

[117] I. Chen and X. Wang, "Sintering dense nanocrystalline ceramics without final-stage grain growth," *Nature*, **404** [6774] 168–71 (2000).

[118] T. Karaki, K. Yan, and M. Adachi, "Barium titanate piezoelectric ceramics manufactured by two-step sintering," *Jpn. J. Appl. Phys.*, **46** [10 B] 7035–7038 (2007).

[119] H.I. Hsiang, C.S. Hsi, C.C. Huang, and S.L. Fu, "Sintering behavior and dielectric properties of $BaTiO_3$ ceramics with glass addition for internal capacitor of LTCC," *J. Alloys Compd.*, **459** [1-2] 307–310 (2008).

[120] H. Naghib-zadeh, C. Glitzky, I. Dörfel, and T. Rabe, "Low temperature sintering of barium titanate ceramics assisted by addition of lithium fluoride-containing sintering additives," *J. Eur. Ceram. Soc.*, **30** [1] 81–86 (2010).

[121] A. Polotai, K. Breece, E. Dickey, C. Randall, and A. Ragulya, "A novel approach to sintering nanocrystalline barium titanate ceramics," *J. Am. Ceram. Soc.*, **88** [11] 3008–3012 (2005).

[122] E.B. Blum, R. Heese, R. Klaffky, S. Krinsky, and J. Safranek, "Operation of a low emittance lattice at the NSLS x-ray ring;" pp. 2304–2306 in *Proc. 1999 Part. Accel. Conf.* New York, 1999.

[123] D.B. Sirdeshmukh, L. Sirdeshmukh, and K.G. Subhadra, *Atomistic Properties of Solids*. Springer Series in Materials Science, Heidelberg, Germany, 2011.

[124] H.P. Klug and L.E. Alexander, *X-Ray Diffraction Procedures: For Polycrystalline and Amorphous Materials*. John Wiley & Sons, New York, 1974.

[125] A. Guinier, *X-ray Diffraction: In Crystals, Imperfect Crystals, and Amorphous Bodies*. Dover Publications, Mineola, NY, 1994.

[126] M. Croft, I. Zakharchenko, Z. Zhong, Y. Gurlak, J. Hastings, J. Hu, R. Holtz, M. DaSilva, *et al.*, "Strain field and scattered intensity profiling with energy dispersive x-ray scattering," *J. Appl. Phys.*, **92** [1] 578 (2002).

[127] M. Croft, V. Shukla, E.K. Akdoğan, N. Jisrawi, Z. Zhong, R. Sadangi, a. Ignatov, L. Balarinni, *et al.*, "In situ strain profiling of elastoplastic bending in Ti–6Al–4V alloy by synchrotron energy dispersive x-ray diffraction," *J. Appl. Phys.*, **105** [9] 093505 (2009).

[128] M. Croft, N. Jisrawi, Z. Zhong, K. Horvath, R.L. Holtz, M. Shepard, M. Lakshmipathy, K. Sadananda, *et al.*, "Stress Gradient Induced Strain Localization in Metals: High Resolution Strain Cross Sectioning via Synchrotron X-Ray Diffraction," *J. Eng. Mater. Technol.*, **130** [2] 021005 (2008).

[129] A.M. Korsunsky, S.P. Collins, R.A. Owen, M.R. Daymond, S. Achtioui, and K.E. James, "Fast residual stress mapping using energy-dispersive synchrotron X-ray diffraction on station 16.3 at the SRS," *J. Synchrotron Radiat.*, **9** [2] 77–81 (2002).

[130] M. Croft, N. Jisrawi, Z. Zhong, R. Holtz, K. Sadananda, J. Skaritka, and T. Tsakalakos, "Fatigue history and in-situ loading studies of the overload effect using high resolution X-ray strain profiling," *Int. J. Fatigue*, **29** [9-11] 1726–1736 (2007).

[131] M. Croft, Z. Zhong, N. Jisrawi, I. Zakharchenko, R. Holtz, J. Skaritka, T. Fast, K. Sadananda, *et al.*, "Strain profiling of fatigue crack overload effects using energy dispersive X-ray diffraction," *Int. J. Fatigue*, **27** [10-12] 1408–1419 (2005).

[132] A. Steuwer, J.R. Santisteban, M. Turski, P.J. Withers, and T. Buslaps, "High-resolution strain mapping in bulk samples using full-profile analysis of energy-dispersive synchrotron X-ray diffraction data," *J. Appl. Crystallogr.*, **37** [6] 883–889 (2004).

[133] A. Steuwer, J.R. Santisteban, M. Turski, P.J. Withers, and T. Buslaps, "High-resolution strain mapping in bulk samples using full-profile analysis of energy dispersive synchrotron X-ray diffraction data," *Nucl. Instruments Methods Phys. Res. Sect. B Beam Interact. with Mater. Atoms*, **238** 200–204 (2005).

[134] K. Akdogan, I. Savkliyildiz, Z. Zhong, and T. Tsakalakos, "Line profile calibration of ultrahigh energy synchrotron EDXRD data by LaB6," *Unpublished*, (n.d.).

[135] O. Kubaschewski, "Titanium: Pyysico-Chemical Properties of its Compounds and Alloys;" in *Int. At. Agency*. Edited by K.L. Komarek. Vienna, 1983.

[136] R. Babu, R. Kandan, H. Jena, K.V. Govindan Kutty, and K. Nagarajan, "Calorimetric investigations on cubic $BaTiO_3$ and Ba0.9Nd0.1TiO3 systems," *J. Alloys Compd.*, **506** [2] 565–568 (2010).

[137] US Research Nanomaterials Inc., *Titanium diboride nanopowder/nanoparticles (95+%, 58nm, hexagonal)*, (2014).

[138] Y. He, "Heat capacity, thermal conductivity, and thermal expansion of barium titanate-based ceramics," *Thermochim. Acta*, **419** [1-2] 135–141 (2004).

[139] M.M. Vijatovic, J.D. Bobic, and B.D. Stojanovic, "History and challenges of barium titanate: Part II," *Sci. Sinter.*, **40** [3] 235–244 (2008).